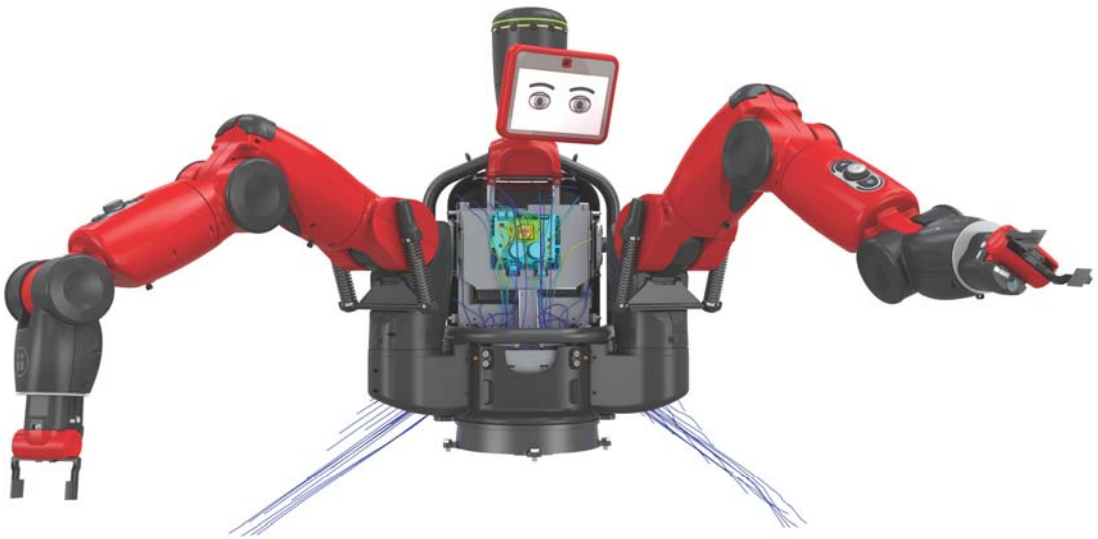


VALIDATION EXAMPLES

SOLIDWORKS FLOW SIMULATION 2020



Contents

Introduction	1
1 Flow through a Cone Valve	3
2 Laminar Flows Between Two Parallel Plates	7
3 Laminar and Turbulent Flows in Pipes	17
4 Flows Over Smooth and Rough Flat Plates	23
5 Flow in a 90-degree Bend Square Duct	27
6 Flows in 2D Channels with Bilateral and Unilateral Sudden Expansions	33
7 Flow over a Circular Cylinder	37
8 Supersonic Flow in a 2D Convergent-Divergent Channel	41
9 Supersonic Flow over a Segmental Conic Body	45
10 Flow over a Heated Plate	51
11 Convection and Radiation in an Annular Tube	55
12 Pin-fin Heat Sink Cooling by Natural Convection	61
13 Plate Fin Heat Sink Cooling by Forced Convection	65
14 Unsteady Heat Conduction in a Solid	69
15 Tube with Hot Laminar Flow and Outer Heat Transfer	73
16 Flow over a Heated Cylinder	77
17 Natural Convection in a Square Cavity	81

18 Particles Trajectories in Uniform Flows.	87
19 Porous Screen in a Non-uniform Stream	93
20 Lid-driven Flows in Triangular and Trapezoidal Cavities.	99
21 Flow in a Cylindrical Vessel with a Rotating Cover	105
22 Flow in an Impeller.	109
23 Rotation of Greek Cross Cylinder.	115
24 Cavitation on a hydrofoil	119
25 Isothermal Cavitation in a Throttle Nozzle	125
26 Thermoelectric Cooling	129
27 Buice-Eaton 2D Diffuser	133
28 Flow Over a Broad-crested Weir	137
References	139



Introduction

A series of calculation examples presented below validate the ability of Flow Simulation to predict the essential features of various flows, as well as to solve conjugate heat transfer problems (i.e. flow problems with heat transfer in solids). In order to perform the validation accurately and to present clear results which the user can check independently, relatively simple examples have been selected. For each of the following examples, exact analytical expression or well-documented experimental results exist. Each of the examples focus on one or two particular physical phenomena such as: laminar flow with or without heat transfer, turbulent flows including vortex development, boundary layer separation and heat transfer, compressible gas flow with shock and expansion waves. Therefore, these examples validate the ability of Flow Simulation to predict fundamental flow features accurately. The accuracy of predictions can be extrapolated to typical industrial examples (encountered every day by design engineers and solved using Flow Simulation), which may include a combination of the above-mentioned physical phenomena and geometries of arbitrary complexity.

Flow through a Cone Valve

Let us see how Flow Simulation predicts incompressible turbulent 3D flows in a 3D cone valve taken from Ref. 13 (the same in Ref. 2) and having a complex flow passage geometry combining sudden 3D contractions and expansions at different turning angles φ (Fig. 1.1). Following the Ref. 2 and Ref. 13 recommendations on determining a valve's hydraulic resistance correctly, i.e. to avoid any valve-generated flow disturbances at the places of measuring the flow total pressures upstream and downstream of the valve, the inlet and outlet straight pipes of the same diameter D and of enough length (we take $7D$ and $17D$) are connected to the valve, so constituting the experimental rig model (see Fig. 1.2). As in Ref. 13, a water flows through this model. Its temperature of 293.2 K and fully developed turbulent inlet profile (see Ref. 1) with mass-average velocity $U \approx 0.5$ m/s (to yield the turbulent flow's Reynolds number based on the pipe diameter $Re_D = 10^5$) are specified at the model inlet, and static pressure of 1 atm is specified at the model outlet.

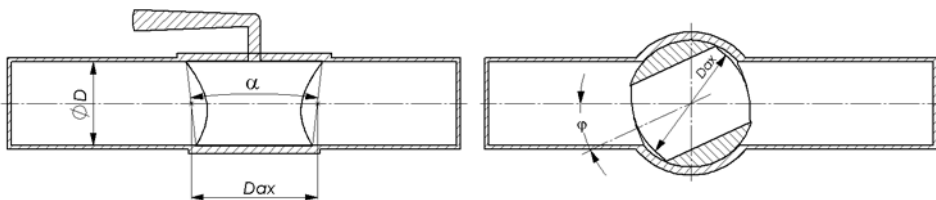


Fig. 1.1 The cone valve under consideration: $D = 0.206$ m, $D_{ax} = 1.515D$, $\alpha = 13^\circ 40'$.

The corresponding model used for these predictions is shown in Fig. 1.2. The valve's turning angle φ is varied in the range of $0 \dots 55^\circ$ (the valve opening diminishes to zero at $\varphi = 82^\circ 30'$).

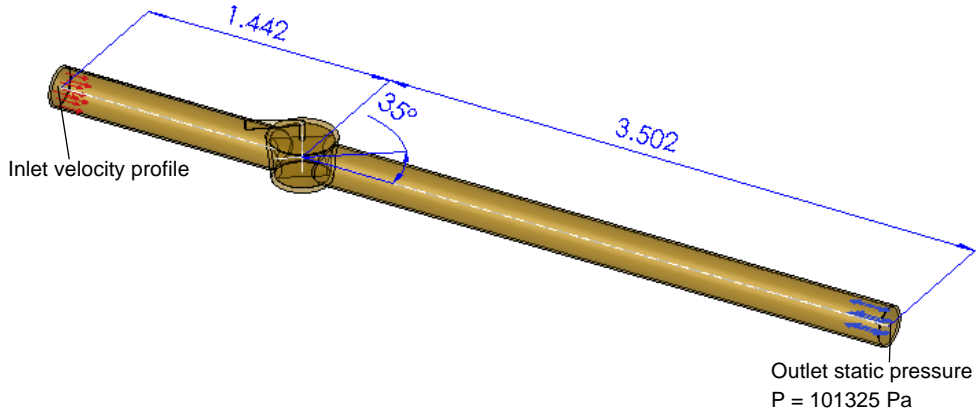


Fig. 1.2 The model for calculating the 3D flow in the cone valve.

The flow predictions performed with Flow Simulation are validated by comparing the valve's hydraulic resistance ζ_v , and the dimensionless coefficient of torque M (see Fig. 1.1) acting on the valve, m , to the experimental data of Ref. 13 (Ref. 2).

Since Ref. 13 presents the valve's hydraulic resistance (i.e. the resistance due to the flow obstacle, which is the valve) ζ_v , whereas the flow calculations in the model (as well as the experiments on the rig) yield the total hydraulic resistance including both ζ_v and the tubes' hydraulic resistance due to friction, ζ_f , i.e. $\zeta = \zeta_v + \zeta_f$, then, to obtain ζ_v from the flow predictions (as well as from the experiments), ζ_f is calculated (measured in the experiments) separately, at the fully open valve ($\varphi = 0$); then $\zeta_v = \zeta - \zeta_f$.

In accordance with Ref. 13, both ζ and ζ_f are defined as $(P_{o\ inlet} - P_{o\ outlet})/(\rho U^2/2)$, where $P_{o\ inlet}$ and $P_{o\ outlet}$ are the flow total pressures at the model's inlet and outlet, accordingly, ρ is the fluid density. The torque coefficient is defined as $m = M/[D^3 \cdot (\rho U^2/2) \cdot (1 + \zeta_v)]$, where M is the torque trying to slew the valve around its axis (vertical in the left picture in Fig. 1.1) due to a non-uniform pressure distribution over the valve's inner passage (naturally, the valve's outer surface pressure cannot contribute to this torque). M is measured directly in the experiments and is integrated by Flow Simulation over the valve's inner passage.

The Flow Simulation predictions have been performed at result resolution level of 5 with manual setting of the minimum gap size to the valve's minimum passage in the $Y = 0$ plane and the minimum wall thickness to 3 mm (to resolve the valve's sharp edges).

Flow Simulation has predicted $\zeta_f = 0.455$, ζ_v shown in Fig. 1.3, and m shown in Fig. 1.4 It is seen that the Flow Simulation predictions well agree with the experimental data.

This cone valve's 3D vortex flow pattern at $\varphi = 45^\circ$ is shown in Fig. 1.5 by flow trajectories colored by total pressure. The corresponding velocity contours and vectors at the $Y = 0$ plane are shown in Fig. 1.6

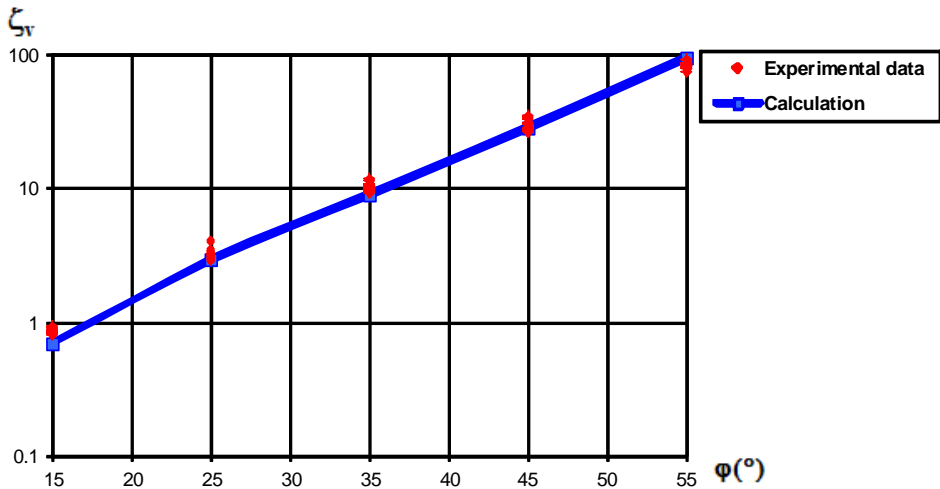


Fig. 1.3 Comparison of the Flow Simulation predictions with the Ref. 13 experimental data on the cone valve's hydraulic resistance versus the cone valve turning angle.

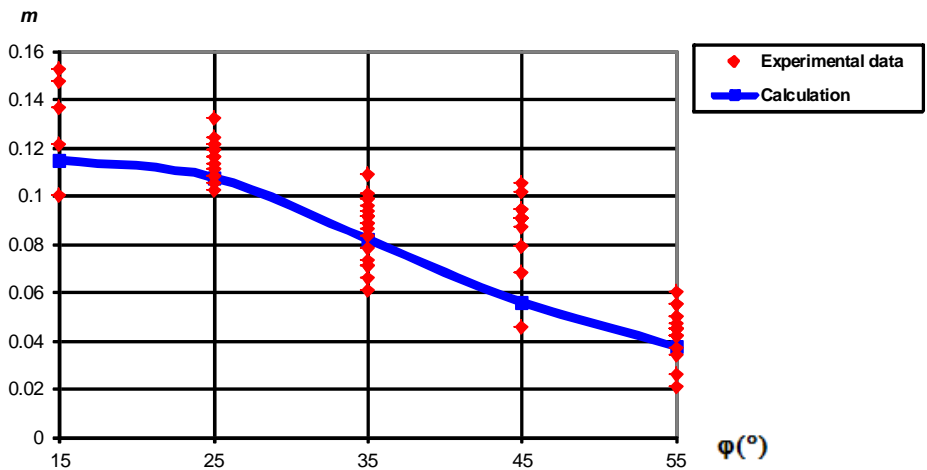


Fig. 1.4 Comparison of the Flow Simulation predictions with the Ref. 13 experimental data on the cone valve's torque coefficient versus the cone valve turning angle.

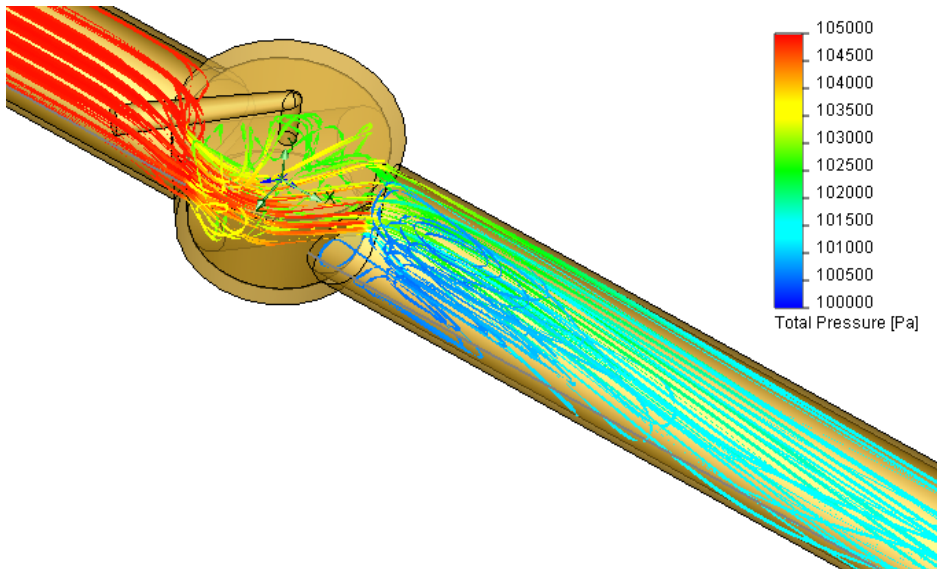


Fig. 1.5 Flow trajectories colored by total pressure at $\varphi = 45^\circ$.

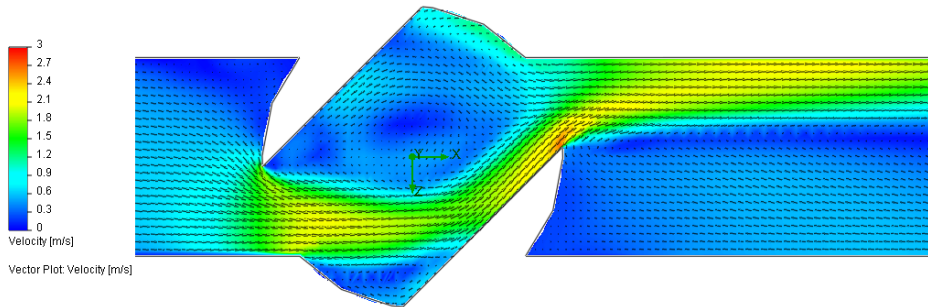


Fig. 1.6 The cone valve's velocity contours and vectors at $\varphi = 45^\circ$.

Laminar Flows Between Two Parallel Plates

Let us consider two-dimensional (planar) steady-state laminar flows of Newtonian, non-Newtonian, and compressible liquids between two parallel stationary plates spaced at a distance of $2h$ (see Fig. 2.1).

In the case of Newtonian and non-Newtonian liquids the channel has a $2h = 0.01$ m height and a 0.2 m length, the inlet for these liquids have standard ambient temperature (293.2 K) and a uniform inlet velocity profile of $u_{average} = 0.01$ m/s (entrance disturbances are neglected). The inlet pressure is not known beforehand, since it will be obtained from the calculations in accordance with the specified channel exit pressure of 1 atm. (The fluids pass through the channel due to a pressure gradient.)

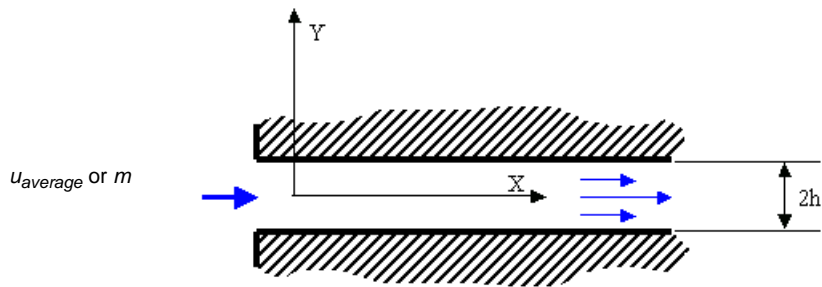


Fig. 2.1 Flow between two parallel plates.

Since the Reynolds number based on the channel height is equal to about $Re_{2h} = 100$, the flow is laminar.

As for the liquids, let us consider water as a Newtonian liquid and four non-Newtonian liquids having identical density of 1000 kg/m^3 , identical specific heat of 4200 J/(kgK) and identical thermal conductivity of 10 W/(mK) , but obeying different non-Newtonian liquid laws available in Flow Simulation.

The considered non-Newtonian liquids' models and their governing characteristics are presented in Table 2.1. These models are featured by the function connecting the flow shear stress (τ) with the flow shear rate ($\dot{\gamma}$), i.e. $\tau = f(\dot{\gamma})$, or, following Newtonian liquids, the liquid dynamic viscosity (η) with the flow shear rate ($\dot{\gamma}$), i.e. $\tau = \eta(\dot{\gamma}) \cdot \dot{\gamma}$:

- 1 the Herschel-Bulkley model: $\tau = K \cdot (\dot{\gamma})^n + \tau_o$, where K is the consistency coefficient, n is the power-law index, and τ_o is the yield stress (a special case with $n = 1$ gives the Bingham model);
- 2 the power-law model: $\tau = K \cdot (\dot{\gamma})^n$, i.e., $\eta = K \cdot (\dot{\gamma})^{n-1}$, which is a special case of Herschel-Bulkley model with $\tau_o = 0$;
- 3 the Carreau model: $\tau = \eta \cdot \dot{\gamma}$, $\eta = \eta_\infty + (\eta_o - \eta_\infty) \cdot \left[1 + (K_1 \cdot \dot{\gamma})^2\right]^{n-1/2}$, where η_∞ is the liquid dynamic viscosity at infinite shear rate, i.e. the minimum dynamic viscosity, η_o is the liquid dynamic viscosity at zero shear rate, i.e. the maximum dynamic viscosity, K_1 is the time constant, n is the power-law index (this model is a smooth version of the power-law model).

Table 2.1 Non-Newtonian liquids' models and their governing characteristics.

Non-Newtonian liquid No.	1	2	3	4
Non-Newtonian liquid model	Herschel-Bulkley	Bingham	Power law	Carreau
Consistency coefficient, K (Pa.s ⁿ)	0.001	0.001	0.001	-
Power law index, n	1.5	1	0.6	0.4
Yield stress, τ_o (Pa)	0.001	0.001	-	-
Minimum dynamic viscosity, η_∞ (Pa.s)	-	-	-	10 ⁻⁴
Maximum dynamic viscosity, η_o (Pa.s)	-	-	-	10 ⁻³
Time constant, K_1 (s)	-	-	-	1

In accordance with the well-known theory presented in Ref. 1, after some entrance length, the flow profile $u(y)$ becomes fully developed and invariable. It can be determined from

the Navier-Stokes x -momentum equation $\frac{dP}{dx} = \frac{d\tau}{dy} = \text{const} = \frac{\tau_w}{h}$ corresponding to

this case in the coordinate system shown in Fig. 2.1 ($y = 0$ at the channel's center plane,

$\frac{dP}{dx}$ is the longitudinal pressure gradient along the channel, $\dot{\gamma} = \frac{du}{dy}$ in the flow under consideration).

As a result, the fully developed $u(y)$ profile for a Newtonian fluid has the following form:

$$u(y) = -\frac{1}{2\eta} \frac{dP}{dx} (h^2 - y^2),$$

where η is the fluid dynamic viscosity and h is the half height of the channel,

$$\frac{dP}{dx} = -\frac{3\eta u_{average}}{h^2},$$

where $u_{average}$ is the flow's mass-average velocity defined as the flow's volume flow rate divided by the area of the flow passage cross section.

For a non-Newtonian liquid described by the power-law model the fully developed $u(y)$ profile and the corresponding pressure gradient can be determined from the following formulae:

$$u(y) = u_{average} \frac{2n+1}{n+1} \left(1 - \left(\frac{y}{h} \right)^{\frac{n+1}{n}} \right), \quad \frac{dP}{dx} = -\frac{K}{h} \cdot \left(\frac{u_{average}}{h} \cdot \frac{2n+1}{n} \right)^n.$$

For a non-Newtonian liquid described by the Herschel-Bulkley model the fully developed $u(y)$ profile can be determined from the following formulae:

$$u(y) = u_{max} = \frac{h}{K^{1/n} \tau_w} \frac{n}{n+1} (\tau_w - \tau_o)^{\frac{n+1}{n}} \quad \text{at } |y| < \frac{\tau_o}{\tau_w} h,$$

$$u(y) = u_{max} \cdot \left(1 - \left(\frac{\tau_w \frac{y}{h} - \tau_o}{\tau_w - \tau_o} \right)^{\frac{n+1}{n}} \right) \quad \text{at } y > \frac{\tau_o}{\tau_w} h,$$

where the unknown wall shear stress τ_w is determined numerically by solving the nonlinear equation

$$u_{average} = \frac{h}{K^{1/n} \tau_w} \cdot \frac{n}{n+1} \cdot (\tau_w - \tau_o)^{\frac{n+1}{n}} \cdot \left(1 - \frac{n}{2n+1} \frac{\tau_w - \tau_o}{\tau_w} \right),$$

e.g. with the Newton method, as described in this validation. The corresponding pressure

gradient is determined as $\frac{dP}{dx} = \frac{\tau_w}{h}.$

For a non-Newtonian liquid described by the Carreau model the fully developed $u(y)$ profile can not be determined analytically in an explicit form, so in this validation example it is obtained by solving the following parametric equation:

$$y = \frac{h}{\tau_w} p \left(\mu_\infty + (\mu_0 - \mu_\infty) (1 + \lambda^2 p^2)^{(n-1)/2} \right),$$

$$u = u_{\max} - \frac{h\mu_\infty}{2\tau_w} p^2 - \frac{(\mu_0 - \mu_\infty)h}{(n+1)\tau_w} (1 + \lambda^2 p^2)^{(n-1)/2} \left(np^2 - \frac{1}{\lambda^2} \right) - \frac{(\mu_0 - \mu_\infty)h}{(n+1)\tau_w \lambda^2},$$

where p is a free parameter varied within the $\pm p_{\max}$ range,

$$\tau_w = p_{\max} \left(\mu_\infty + (\mu_0 - \mu_\infty) (1 + \lambda^2 p_{\max}^2)^{(n-1)/2} \right),$$

$$u_{\max} = \frac{h\mu_\infty}{2\tau_w} p_{\max}^2 + \frac{(\mu_0 - \mu_\infty)h}{(n+1)\tau_w} (1 + \lambda^2 p_{\max}^2)^{(n-1)/2} \left(np_{\max}^2 - \frac{1}{\lambda^2} \right) + \frac{(\mu_0 - \mu_\infty)h}{(n+1)\tau_w \lambda^2}$$

The p value is varied to satisfy $hu_{average} = \int_0^h u dy = \int_0^{p_{\max}} u \frac{dy}{dp} dp$.

The corresponding pressure gradient is equal to $\frac{dP}{dx} = \frac{\tau_w}{h}$.

The SOLIDWORKS model for the 2D calculation is shown in Fig. 2.2. The boundary conditions are specified as mentioned above and the initial conditions coincide with the inlet boundary conditions. The results of the calculations performed with Flow Simulation at result resolution level 5 are presented in Figs .2.3 - 2.8. The channel exit $u(y)$ profile and the channel $P(x)$ profile were obtained along the sketches shown by green lines in Fig. 2.2.

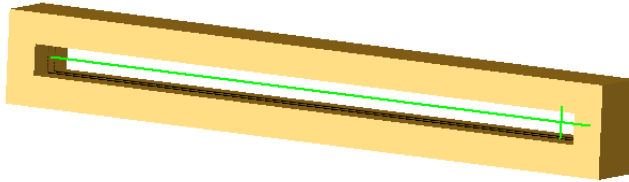


Fig. 2.2 The model for calculating 2D flow between two parallel plates with Flow Simulation.

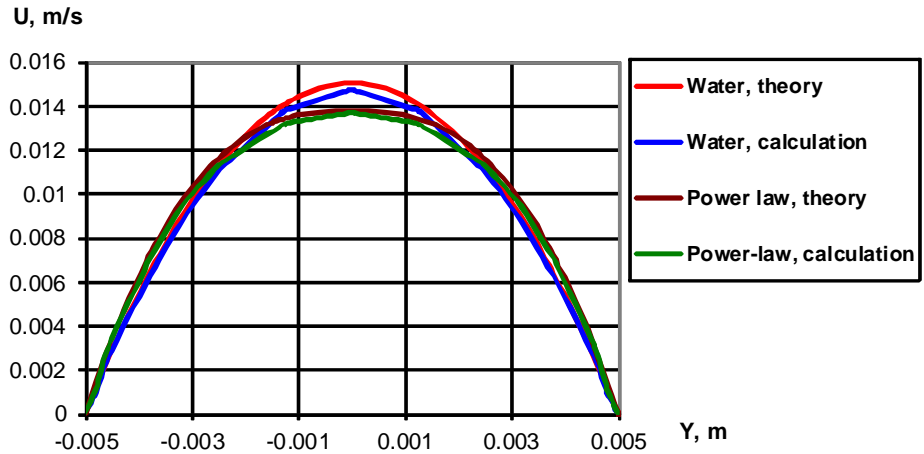


Fig. 2.3 The water and liquid #3 velocity profiles $u(y)$ at the channel outlet.

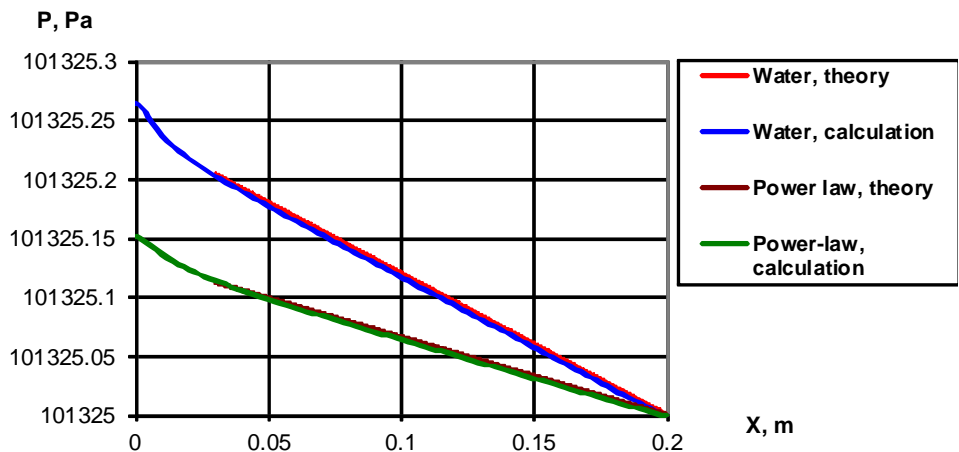


Fig. 2.4 The water and liquid #3 longitudinal pressure change along the channel, $P(x)$.

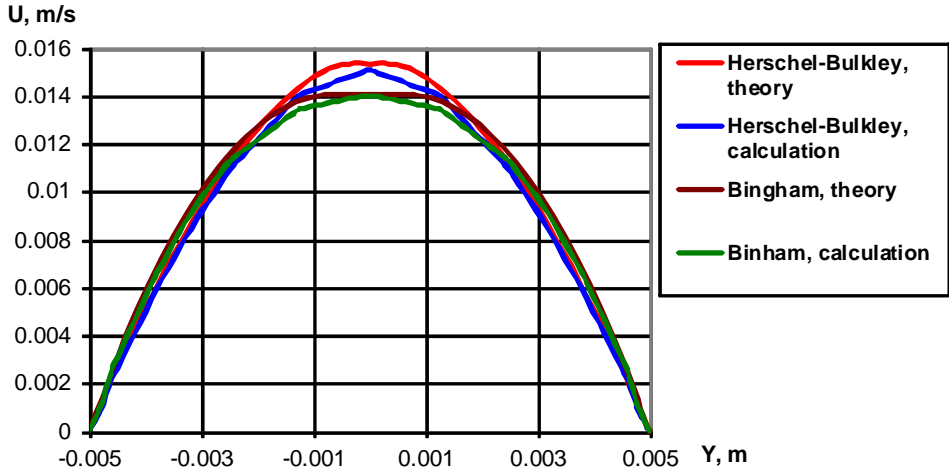


Fig. 2.5 The liquids #1 and #2 velocity profiles $u(y)$ at the channel outlet.

From Figs. 2.4, 2.6, and 2.8 you can see that for all the liquids under consideration, after some entrance length of about 0.03 m, the pressure gradient governing the channel pressure loss becomes constant and nearly similar to the theoretical predictions. From Figs. 2.3, 2.5, and 2.7 you can see that the fluid velocity profiles at the channel exit obtained from the calculations are close to the theoretical profiles.

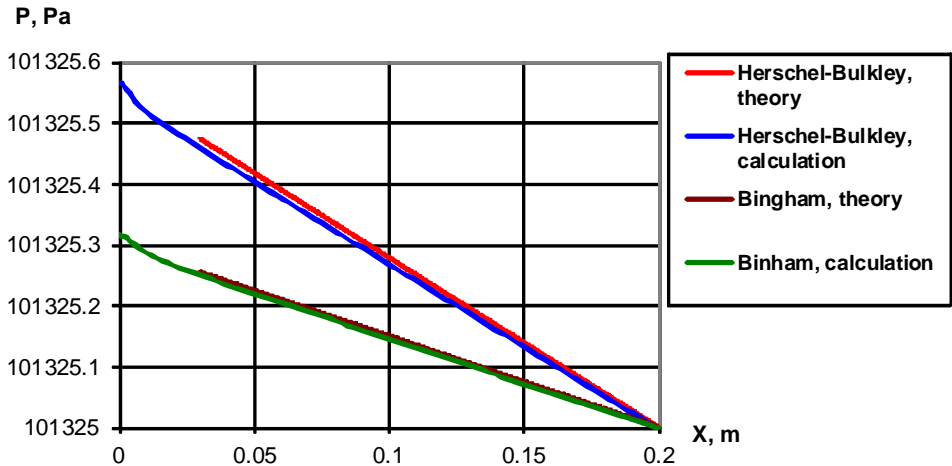


Fig. 2.6 The liquids #1 and #2 longitudinal pressure change along the channel, $P(x)$.

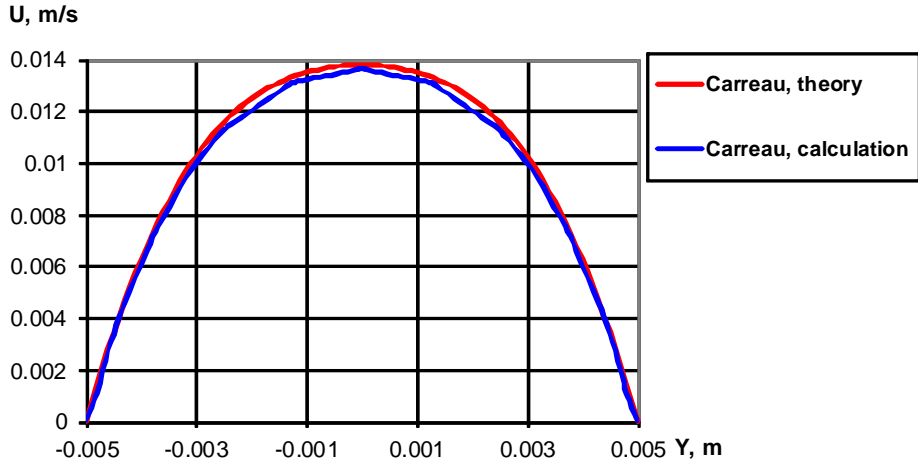


Fig. 2.7 The liquid #4 velocity profile $u(y)$ at the channel outlet.

In the case of compressible liquids the channel has the height of $2h = 0.001$ m and the length of 0.5 m, the liquids at its inlet had standard ambient temperature (293.2 K) and a uniform inlet velocity profile corresponding to the specified mass flow rate of $\dot{m} = 0.01$ kg/s.

The inlet pressure is not known beforehand, since it will be obtained from the calculations as providing the specified mass flow rate under the specified channel exit pressure of 1 atm. (The fluids pass through the channel due to the pressure gradient).

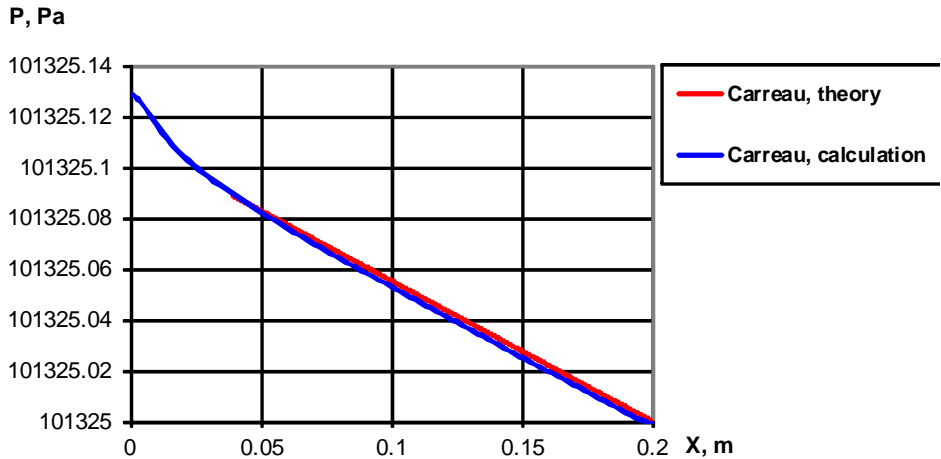


Fig. 2.8 The liquid #4 longitudinal pressure change along the channel, $P(x)$.

Let us consider two compressible liquids whose density obeys the following laws:

- the power law:

$$\left(\frac{\rho}{\rho_0}\right)^n = \frac{P+B}{P_0+B}, \text{ where } \rho_0, P_0, B \text{ and } n \text{ are specified: } \rho_0 \text{ is the liquid's density under the reference pressure } P_0, B \text{ and } n \text{ are constants,}$$

- the logarithmic law:

$$\rho = \frac{\rho_0}{1 - C \ln \frac{B+P}{B+P_0}}, \text{ where } \rho_0, P_0, B \text{ and } C \text{ are specified: } \rho_0 \text{ is the liquid's density under the reference pressure } P_0, B \text{ and } C \text{ are constants.}$$

In this validation example these law's parameters values have been specified as $\rho_0 = 10^3 \text{ kg/m}^3$, $P_0 = 1 \text{ atm}$, $B = 10^7 \text{ Pa}$, $n = 1.4$, $C = 1$, and these liquids have the $1 \text{ Pa}\cdot\text{s}$ dynamic viscosity.

Since this channel is rather long, the pressure gradient along it can be determined as

$$\frac{\partial P}{\partial x} = -\frac{3\eta}{h^2} \frac{\dot{m}}{S\rho}, \text{ where } \eta \text{ is the liquids' dynamic viscosity, } \dot{m} \text{ is the liquid mass flow rate, } S \text{ is the channel's width, } \rho \text{ is the liquid density.}$$

Therefore, by substitution the compressible liquids' $\rho(P)$ functions, we obtain the following equations for determining $P(x)$ along the channel:

- for the power-law liquid:

$$\frac{\partial P}{\partial x} = -\frac{3\mu}{h^2} \frac{\dot{m}}{S\rho_0} \left(\frac{P_0+B}{P+B}\right)^{1/n}$$

its solution is

$$(P+B)^{1+1/n} \frac{n}{n+1} = \frac{3\mu\dot{m}}{h^2 S \rho_0} (P_0+B)^{1/n} x + C_1,$$

where C_1 is a constant determined from the boundary conditions;

- $\frac{\partial P}{\partial x} = -\frac{3\mu}{h^2} \frac{\dot{m}}{S\rho_0} \left(1 - C \ln \frac{P+B}{P_0+B}\right)$, this equation is solved numerically.

Both the theoretical $P(x)$ distributions and the corresponding distributions computed within Flow Simulation on a 5×500 computational mesh are presented in Figs. 2.9 and 2.10. It is seen that the Flow Simulation calculations agree with the theoretical distributions.

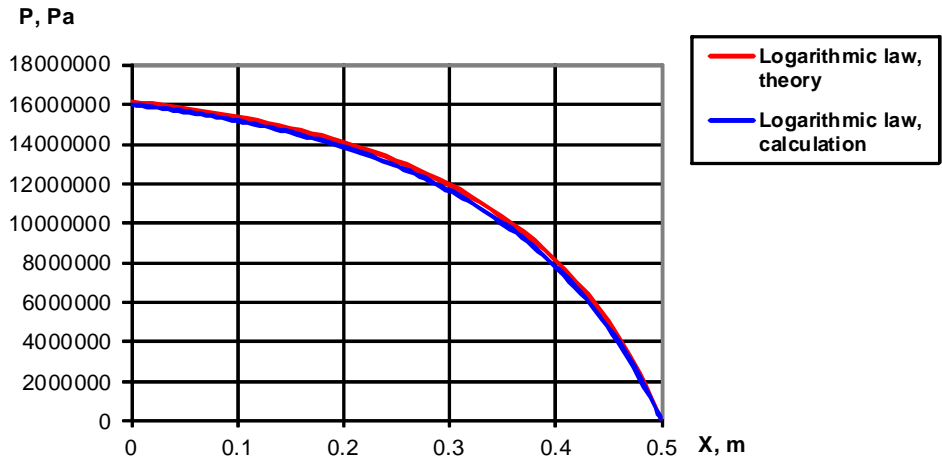


Fig. 2.9 The logarithmic-law compressible liquid's longitudinal pressure change along the channel, $P(x)$.

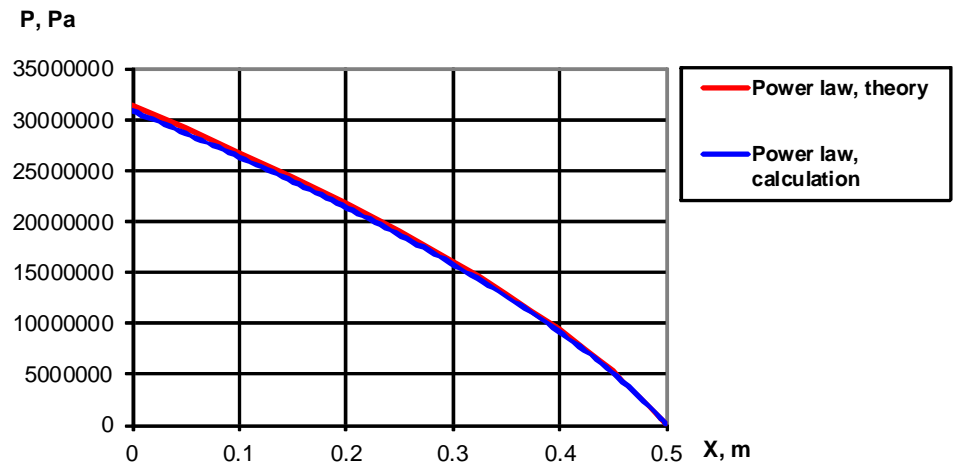


Fig. 2.10 The power-law compressible liquid's longitudinal pressure change along the channel, $P(x)$.

Laminar and Turbulent Flows in Pipes

Let us see how the 3D flow through a straight pipe is predicted. We consider water (at standard 293.2 K temperature) flowing through a long straight pipe with circular cross section of $d = 0.1$ m (see Fig. 3.1). At the pipe inlet the velocity is uniform and equal to u_{inlet} . At the pipe outlet the static pressure is equal to 1 atm.

The geometry model used for all the 3D pipe flow calculations is shown in Fig. 3.2 The initial conditions have been specified to coincide with the inlet boundary conditions. The computational domain is reduced to domain ($Z \geq 0, Y \geq 0$) with specifying the flow symmetry planes at $Z = 0$ and $Y = 0$.

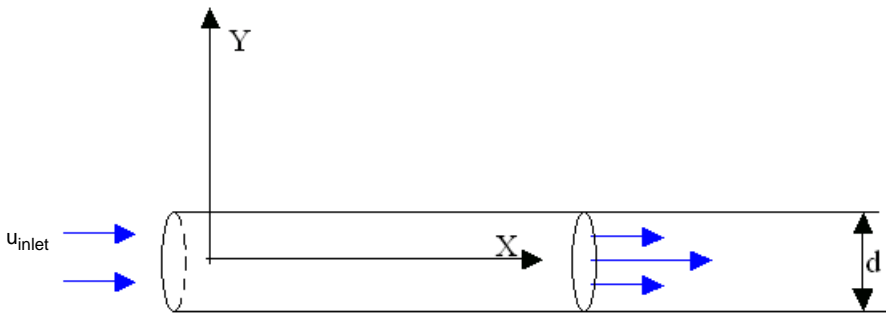


Fig. 3.1 Flow in a pipe.

According to theory (Ref. 1), the pipe flow velocity profile changes along the pipe until it becomes a constant, fully developed profile at a distance of L_{inlet} from the pipe inlet. According to Ref. 1, L_{inlet} is estimated as:

$$L_{inlet} = \begin{cases} 0.03 \cdot d \cdot Re_d \geq 3 \cdot d, & Re_d = 0.1 \dots 2500 \\ 100 \cdot d, & Re_d = 2500 \dots 6000 \\ 40 \cdot d, & Re_d = 6000 \dots 10^6 \end{cases}$$

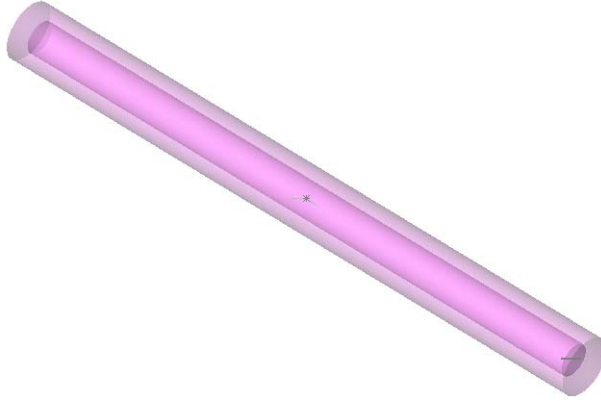


Fig. 3.2 The SOLIDWORKS model for calculating 3D flow in a pipe with Flow Simulation.

where $Re_d = \rho \cdot U \cdot d / \mu$ is the Reynolds number based on the pipe diameter d , U is the mass-average flow velocity, ρ is the fluid density, and μ is the fluid dynamic viscosity.

Therefore, to provide a fully developed flow in the pipe at Re_d under consideration, we will study the cases listed in Table 3.1. Here, L_{pipe} is the overall pipe length. All the Flow Simulation predictions concerning the fully developed pipe flow characteristics are referred to the pipe section downstream of the inlet section.

Table 3.1 Pipe inlet velocities and lengths.

Re_d	u_{inlet} m/s	L_{inlet} m	L_{pipe} m
0.1	10^{-6}	0.3	0.45
100	0.001	0.3	0.45
1000	0.01	3	4.5
10^4	0.1	4 (5)*	6 (10)*
10^5	1	4 (5)*	6 (10)*
10^6	10	4 (5)*6	6 (10)*

*) the lengths in brackets are for the rough pipes.

The flow regime in a pipe can be laminar, turbulent, or transitional, depending on Re_d . According to Ref. 1, $Re_d = 4000$ is approximately the boundary between laminar pipe flow and turbulent one (here, the transitional region is not considered).

Theory (Refs. 1 and 4) states that for laminar fully developed pipe flows (Hagen-Poiseuille flow) the velocity profile $u(y)$ is invariable and given by:

$$u(y) = -\frac{1}{4\mu} \frac{dP}{dx} (R^2 - y^2) \quad ,$$

where R is the pipe radius, and dP/dx is the longitudinal pressure gradient along the pipe, which is also invariable and equal to:

$$\frac{dP}{dx} = -\frac{8\mu u_{inlet}}{R^2} .$$

The Flow Simulation predictions of dP/dx and $u(y)$ of the laminar fully developed pipe flow at $Re_d = 100$ performed at result resolution level 6 are presented in Fig. 3.4 and Fig. 3.3 The presented predictions relate to the smooth pipe, and similar ones not presented here have been obtained for the case of the rough tube with relative sand roughness of $k/d = 0.2 \dots 0.4 \%$, that agrees with the theory (Ref. 1).

Velocity (m/s)

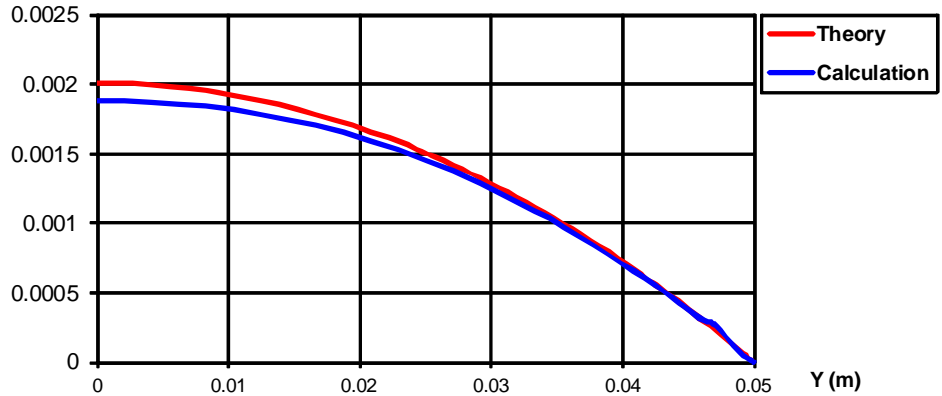


Fig. 3.3 The fluid velocity profile at the pipe exit for $Re_d \approx 100$.

Pressure (Pa)

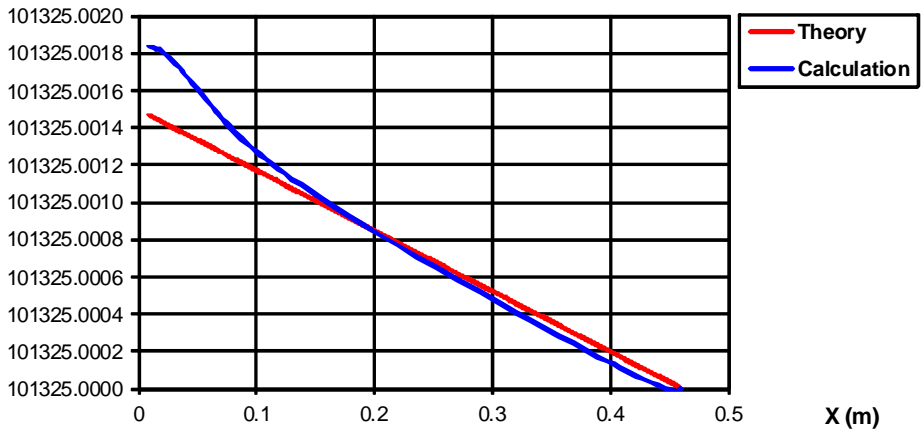


Fig. 3.4 The longitudinal pressure change (pressure gradient) along the pipe at $Re_d \approx 100$.

From Fig. 3.4 one can see that after an entrance length of about 0.15 m the pressure gradient predicted by Flow Simulation coincides with the one predicted by theory. Therefore, the prediction of pipe pressure loss is excellent. As for local flow features, from Fig. 3.3 one can see that the fluid velocity profiles predicted at the pipe exit are rather close to the theoretical profile.

The velocity profile and longitudinal pressure distribution in a smooth pipe at $Re_d = 10^5$, i.e., in a turbulent pipe flow regime, predicted by Flow Simulation at result resolution level 6 are presented in Figs.3.5 and 3.6 and compared to theory (Ref. 1, the Blasius law of pressure loss, the 1/7-power velocity profile).

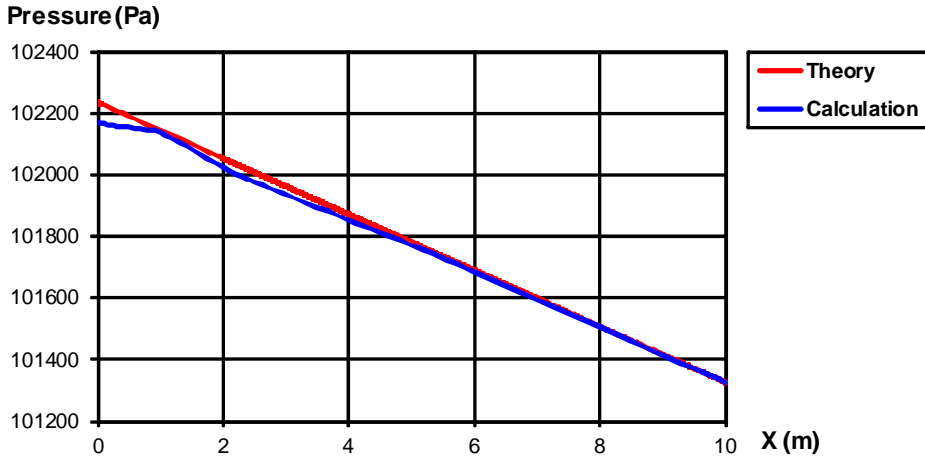


Fig. 3.5 The longitudinal pressure change (pressure gradient) along the pipe at $Re_d = 10^5$.

Then, to stand closer to engineering practice, let us consider the Flow Simulation predictions of the pipe friction factor used commonly and defined as:

$$f = \frac{\Delta P}{\rho \frac{u_{inlet}^2}{2}} \cdot \frac{d}{L} ,$$

where L is length of the pipe section with the fully developed flow, along which pressure loss ΔP is measured.

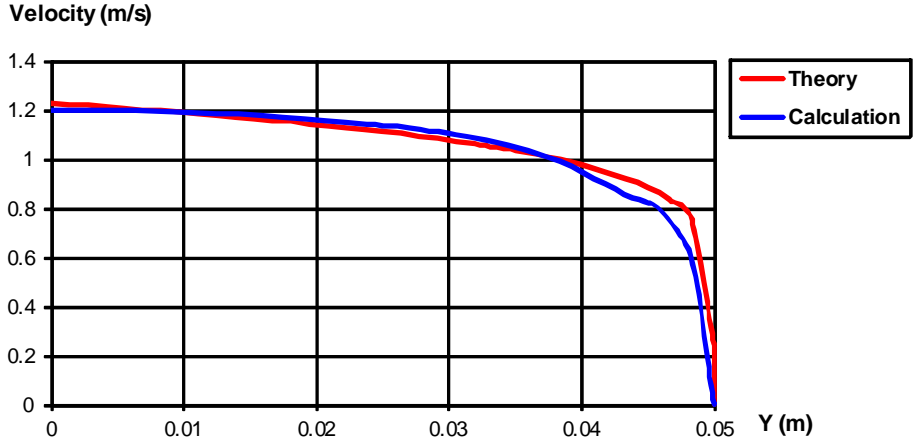


Fig. 3.6 The fluid velocity profile at the pipe exit at $Re_d = 10^5$.

In Figs. 3.7 and 3.8 (scaled up) you can see the Flow Simulation predictions performed at result resolution level 5 for the smooth pipes in the entire Re_d range (both laminar and turbulent), and compared with the theoretical and empirical values determined from the following formulae which are valid for fully-developed flows in smooth pipes (Refs. 1, 2, and 4):

$$f = \begin{cases} \frac{64}{Re_d}, & Re_d \leq 2300 - \text{laminar flows}, \\ 0.316 \cdot Re_d^{-1/4}, & 4000 < Re_d < 10^5 - \text{turbulent flows}, \\ \left(1.8 \cdot \log \frac{Re_d}{6.9}\right)^{-2}, & Re_d \geq 10^5 - \text{turbulent flows} \end{cases}$$

It can be seen that the friction factor values predicted for smooth pipes, especially in the laminar region, are fairly close to the theoretical and empirical curve.

As for the friction factor in rough pipes, the Flow Simulation predictions for the pipes having relative wall roughness of $k/d = 0.4\%$ (k is the sand roughness) are presented and compared with the empirical curve for such pipes (Refs. 1, 2, and 4) in Fig. 3.8. The underprediction error does not exceed 13%.

Additionally, in the full accordance with theory and experimental data the Flow Simulation predictions show that the wall roughness does not affect the friction factor in laminar pipe flows.

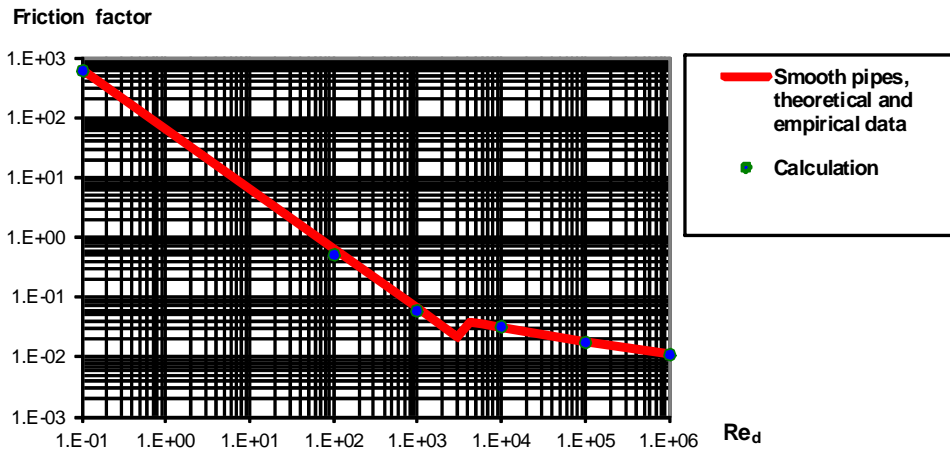


Fig. 3.7 The friction factor predicted by Flow Simulation for smooth pipes in comparison with the theoretical and empirical data (Refs. 1, 2, and 4).

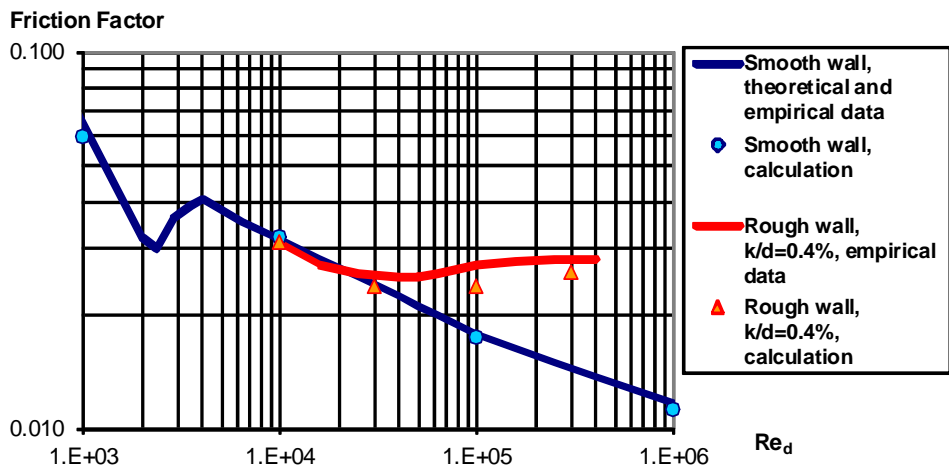


Fig. 3.8 The friction factor predicted by Flow Simulation for smooth and rough pipes in comparison with the theoretical and empirical data (Refs. 1, 2, and 4).

Flows Over Smooth and Rough Flat Plates

Let us consider uniform flows over smooth and rough flat plates with laminar and turbulent boundary layers, so that Flow Simulation predictions of a flat plate drag coefficient are validated.

We consider the boundary layer development of incompressible uniform 2D water flow over a flat plate of length L (see Fig. 4.1). The boundary layer develops from the plate leading edge lying at the upstream computational domain boundary. The boundary layer at the leading edge is considered laminar. Then, at some distance from the plate leading edge the boundary layer automatically becomes turbulent (if this distance does not exceed L).

The geometry model is shown in Fig. 4.2. The problem is solved as internal in order to avoid a conflict situation in the corner mesh cell where the external flow boundary and the model wall intersect. In the internal flow problem statement, to avoid any influence of the upper model boundary or wall on the flow near the flat plate, the ideal wall boundary condition has been specified on the upper wall. The plate length is equal to 10 m, the channel height is equal to 2 m, the walls' thickness is equal to 0.5 m.

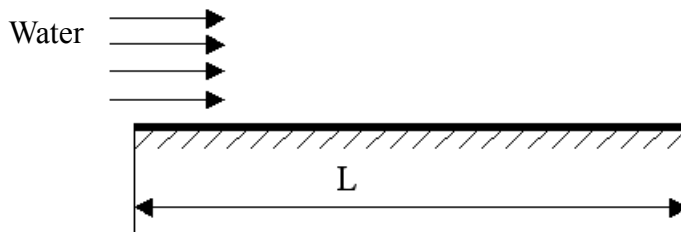


Fig. 4.1 Flow over a flat plate.

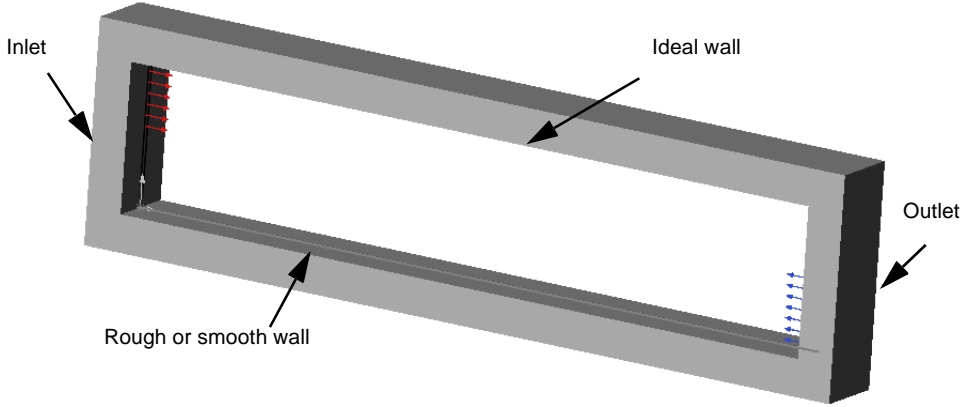


Fig. 4.2 The model for calculating the flow over the flat plate with Flow Simulation.

To solve the problem, an incoming uniform water flow of a certain velocity (see below), temperature of 293.2 K, turbulence intensity of 1%, and turbulence length of 0.01 m is specified at the channel inlet, whereas the water static pressure of 1 atm is specified at the channel outlet.

The flow computation is aimed at predicting the flat plate drag coefficient, defined as (see Ref. 1 and Ref. 4):

$$C_d = \frac{F}{\frac{\rho V^2}{2} A} ,$$

where F is the plate drag force, A is the plate surface area, ρ is fluid density, and V is the fluid velocity.

According to Ref. 1 and Ref. 4, the plate drag coefficient value is governed by the Reynolds number, based on the distance L from the plate leading edge ($Re_L = \rho V L / \mu$, where ρ is the fluid density, V is the incoming uniform flow velocity, and μ is fluid dynamic viscosity), as well as by the relative wall roughness L/k , where k is the sand roughness. As a result, Ref. 1 and Ref. 4 give us the semi-empirical flat plate $C_D(Re_L)$ curves obtained for different L/k from the generalized tubular friction factor curves and presented in Fig. 4.3 (here, $\varepsilon \equiv k$). If the boundary layer is laminar at the plate leading edge, then the wall roughness does not affect C_D until the transition from the laminar boundary layer to the turbulent one, i.e., the $C_D(Re_L)$ curve is the same as for a hydraulically smooth flat plate. The transition region's boundaries depend on various factors, the wall roughness among them. Here is shown the theoretical transition region for a hydraulically smooth flat plate. The transition region's boundary corresponding to fully turbulent flows (i.e., at the higher Re_L) is marked in Fig. 4.3 by a dashed line. At the higher Re_L , the semi-empirical theoretical curves have flat parts along which Re_L does not affect C_D at a fixed wall roughness. These flat parts of the semi-empirical theoretical curves have been obtained by a theoretical scaling of the generalized tubular friction factor curves to the flat plate conditions under the assumption of a turbulent boundary layer beginning from the flat plate leading edge.

To validate the Flow Simulation flat plate C_D predictions within a wide Re_L range, we have varied the incoming uniform flow velocity at the model inlet to obtain the Re_L values of 10^5 , $3 \cdot 10^5$, 10^6 , $3 \cdot 10^6$, 10^7 , $3 \cdot 10^7$, 10^8 , $3 \cdot 10^8$, 10^9 . To validate the wall roughness influence on C_D , the wall roughness k values of 0, 50, 200, 10^3 , $5 \cdot 10^3$, 10^4 μm have been considered. The Flow Simulation calculation results obtained at result resolution level 5 and compared with the semi-empirical curves are presented in Fig. 4.3.

As you can see from Fig. 4.3, $C_D(Re_L)$ of rough plates is somewhat underpredicted by Flow Simulation in the turbulent region, at $L/k \geq 1000$ the $C_D(Re_L)$ prediction error does not exceed about 12%.

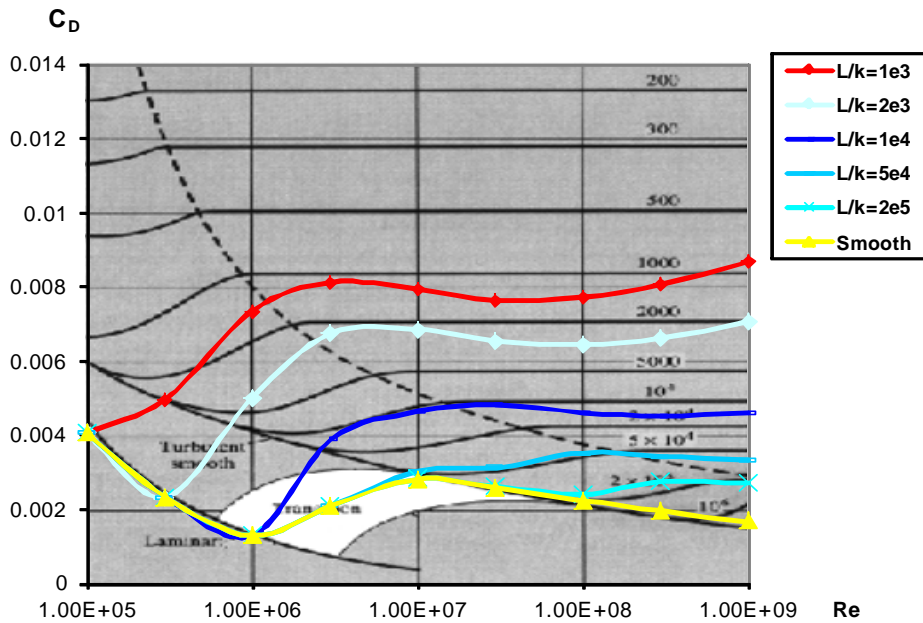


Fig. 4.3 The flat plate drag coefficient predicted with Flow Simulation for rough and hydraulically smooth flat plates in comparison with the semi-empirical curves (Refs. 1 and 4).

Flow in a 90-degree Bend Square Duct

Following Ref. 7, we will consider a steady-state flow of water (at 293.2 K inlet temperature and $U_{inlet} = 0.0198$ m/s inlet uniform velocity) in a 40x40 mm square cross-sectional duct having a 90°-angle bend with $r_i = 72$ mm inner radius ($r_o = 112$ mm outer radius accordingly) and attached straight sections of 1.8 m upstream and 1.2 m downstream (see Fig. 5.1). Since the flow's Reynolds number, based on the duct's hydraulic diameter ($D = 40$ mm), is equal to $Re_D = 790$, the flow is laminar.

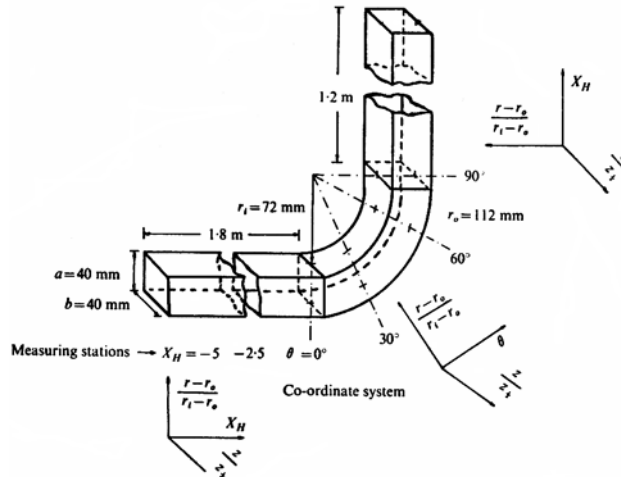


Fig. 5.1 The 90°-bend square duct's configuration indicating the velocity measuring stations and the dimensionless coordinates used for presenting the velocity profiles.

The predicted dimensionless (divided by U_{inlet}) velocity profiles are compared in Figs. 5.2, 5.3 with the ones measured with a laser-Doppler anemometry at the following duct cross sections: $X_H = -5D, -2.5D, 0$ (or $\theta = 0^\circ$) and at the $\theta = 30^\circ, 60^\circ, 90^\circ$ bend

sections. The z and r directions are represented by coordinates $\frac{r - r_o}{r_i - r_o}$ and $\frac{z}{z_{1/2}}$, where $z_{1/2} = 20$ mm. The dimensionless velocity isolines (with the 0.1 step) at the duct's $\theta = 60^\circ$ and 90° sections, both measured in Ref. 7 and predicted with Flow Simulation, are shown in Figs. 5.4 and 5.5.

It is seen that the Flow Simulation predictions are close to the Ref. 7 experimental data.

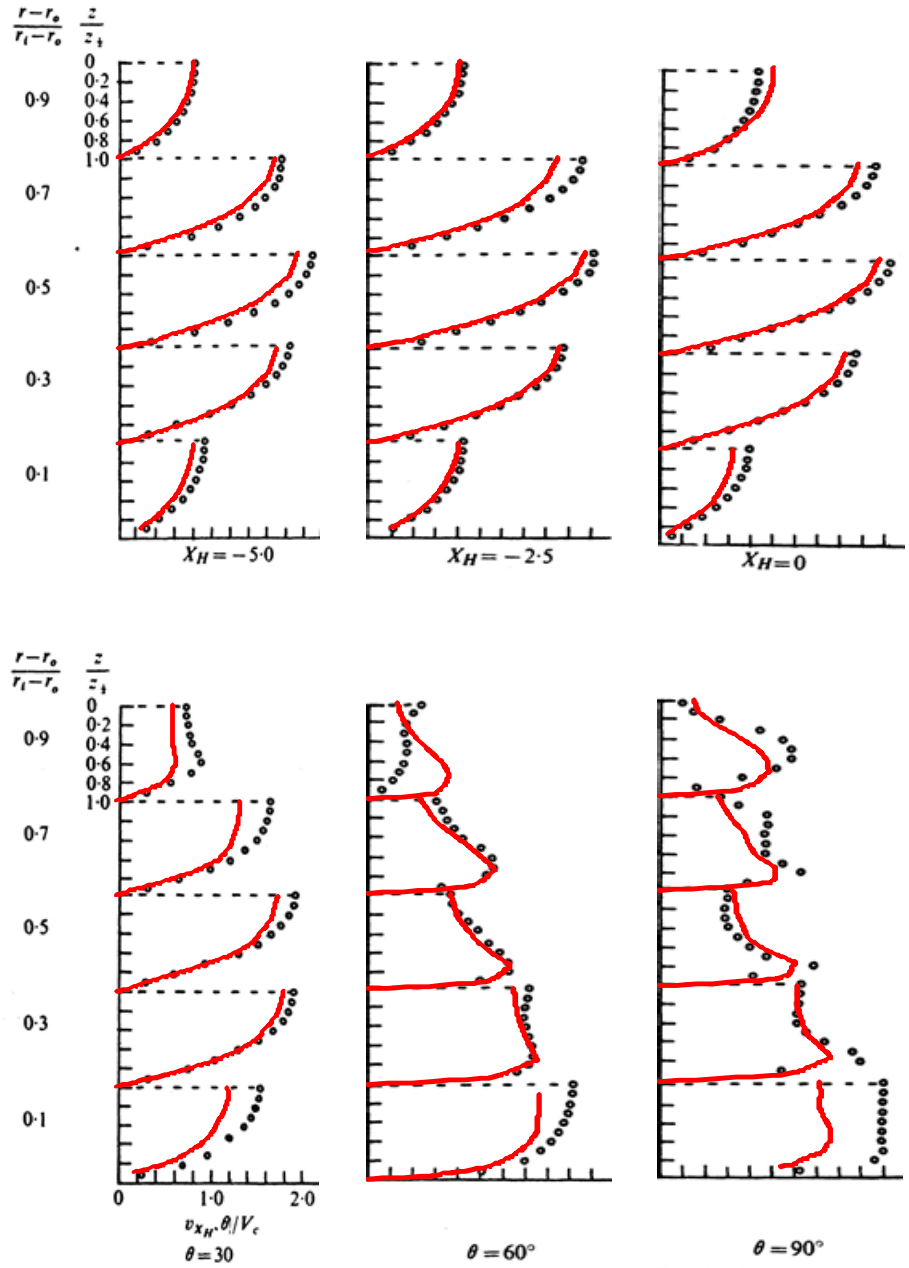


Fig. 5.2 The duct's velocity profiles predicted by Flow Simulation (red lines) in comparison with the Ref. 7 experimental data (circles).

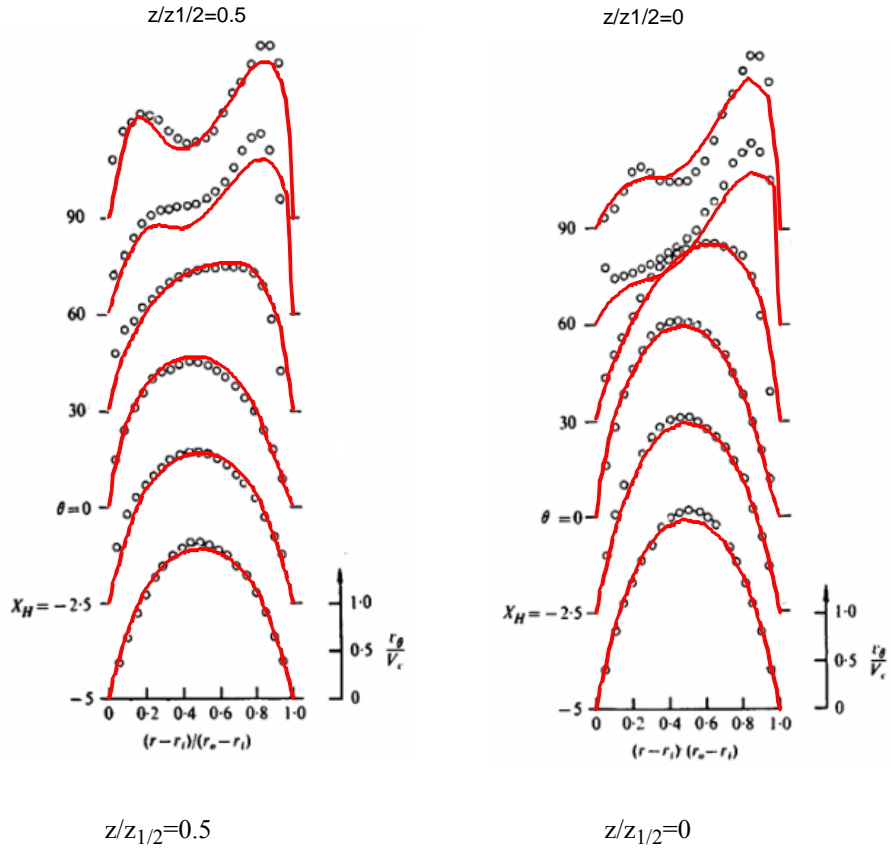


Fig. 5.3 The duct's velocity profiles predicted by Flow Simulation (red lines) in comparison with the Ref. 7 experimental data (circles).

Isolines: Wvc 60 []

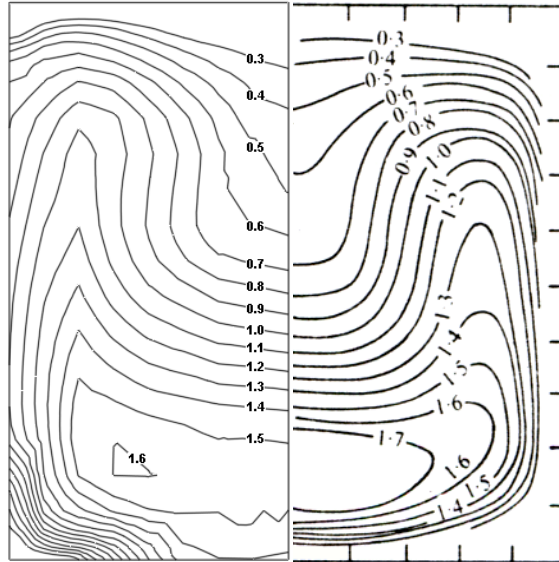


Fig. 5.4 The duct's velocity isolines at the $\theta = 60^\circ$ section predicted by Flow Simulation (left) in comparison with the Ref. 7 experimental data (right).

Isolines: Wvc 90 []

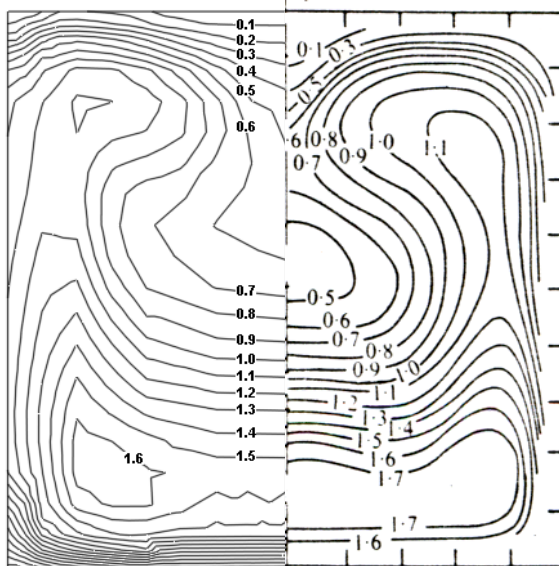


Fig. 5.5 The duct's velocity isolines at the $\theta = 90^\circ$ section predicted by Flow Simulation (left) in comparison with the Ref. 7 experimental data (right).

Flows in 2D Channels with Bilateral and Unilateral Sudden Expansions

In this example we will consider both turbulent and laminar incompressible steady-state flows through 2D (plane) channels with bilateral and unilateral sudden expansions and parallel walls, as shown in Figs. 6.1 and 6.2. At the 10 cm inlet height of the bilateral-sudden-expansion channels a uniform water stream at 293.2 K and 1 m/s is specified. The Reynolds number is based on the inlet height and is equal to $Re = 10^5$, therefore (since $Re > 10^4$) the flow is turbulent. At the 30 mm height inlet of the unilateral-sudden-expansion channel an experimentally measured water stream at 293.2 K and 8.25 mm/s mean velocity is specified, so the Reynolds number based on the inlet height is equal to $Re = 250$, therefore the flow is laminar. In both channels, the sudden expansion generates a vortex, which is considered in this validation from the viewpoint of hydraulic loss in the bilateral-expansion channel (compared to Ref. 2) and from the viewpoint of the flow velocity field in the unilateral-expansion channel (compared to Ref. 12).

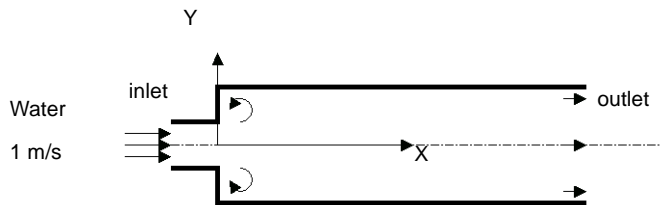


Fig. 6.1 Flow in a 2D (plane) channel with a bilateral sudden expansion.

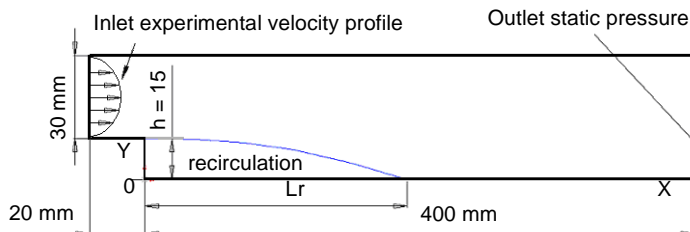


Fig. 6.2 Flow in a 2D (plane) channel with a unilateral sudden expansion.

Bilateral sudden expansion

In accordance with Ref. 2, the local hydraulic loss coefficient of a bilateral sudden expansion (the so-called total pressure loss due to flow) for a turbulent ($Re > 10^4$) flow with a uniform inlet velocity profile depends only on the expansion area ratio and is determined from the following formula:

$$\zeta_s = \frac{P_0 - P_1}{\frac{\rho u_0^2}{2}} = \left(1 - \frac{A_0}{A_1}\right)^2,$$

where A_0 and A_1 are the inlet and outlet cross sectional areas respectively, P_0 and P_1 are the inlet and outlet total pressures, and $\rho u_0^2/2$ is the inlet dynamic head.

In a real sudden expansion the flow hydraulic loss coefficient is equal to $\zeta = \zeta_f + \zeta_s$, where ζ_f is the friction loss coefficient. In order to exclude ζ_f from our comparative analysis, we have imposed the ideal wall boundary condition on all of the channel walls.

In this validation example the channel expansion area ratios under consideration are: 1.5, 2.0, 3.0, and 6.0. To avoid disturbances at the outlet due to the sudden expansion, the channel length is 10 times longer than its height. The 1 atm static pressure is specified at the channel outlet.

The ζ_s values predicted by Flow Simulation at result resolution level 8 for different channel expansion area ratios A_0/A_1 are compared to theory in Fig. 6.3

From Fig. 6.3, one can see that Flow Simulation overpredicts ζ_s by about 4.5...7.9 %.

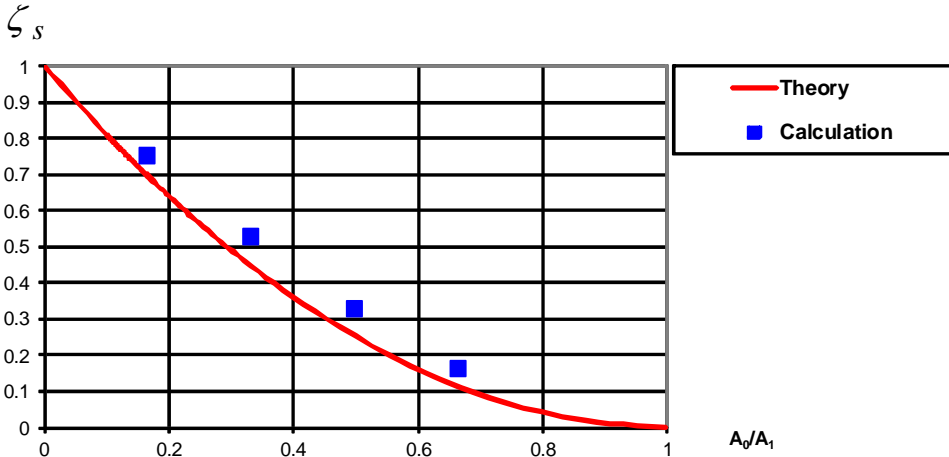


Fig. 6.3 Comparison of Flow Simulation calculations to the theoretical values (Ref. 2) for the sudden expansion hydraulic loss coefficient versus the channel expansion area ratio.

Unilateral sudden expansion

The model used for the unilateral-sudden-expansion channel's flow calculation is shown in Fig. 6.4 The channel's inlet section has a 30 mm height and a 20 mm length. The channel's expanded section (downstream of the 15 mm height back step) has a 45 mm height and a 400 mm length (to avoid disturbances of the velocity field compared to the experimental data from the channel's outlet boundary condition). The velocity profile measured in the Ref. 12 at the corresponding $Re_h = 125$ (the Reynolds number based on the step height) is specified as a boundary condition at the channel inlet. The 10^5 Pa static pressure is specified at the channel outlet.

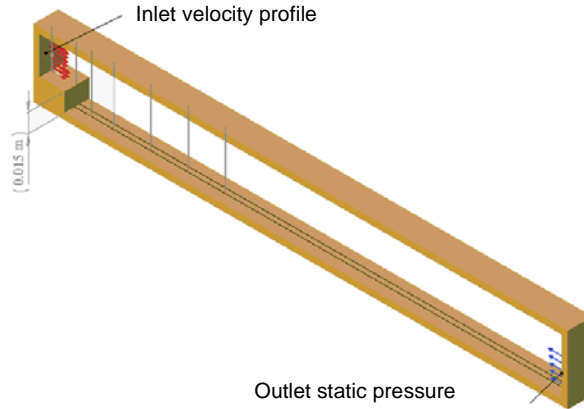


Fig. 6.4 The SOLIDWORKS model for calculating the 2D flow in the unilateral-sudden-expansion channel with Flow Simulation.

The flow velocity field predicted by Flow Simulation at result resolution level 8 is compared in Figs. 6.5, 6.6, and 6.7 to the values measured in Ref. 12 with a laser anemometer. The flow X-velocity (u/U , where $U = 8.25$ mm/s) profiles at several $X = \text{const}$ (-20 mm, 0, 12 mm, ... 150 mm) cross sections are shown in Fig. 6.5 It is seen that the predicted flow velocity profiles are very close to the experimental values both in the main stream and in the recirculation zone. The recirculation zone's characteristics, i.e. its length L_R along the channel's wall, (plotted versus the Reynolds number Re_h based on the channel's step height h , where $Re_h = 125$ for the case under consideration), the separation streamline, and the vortex center are shown in Figs. 6.6 and 6.7. It is seen that they are very close to the experimental data.

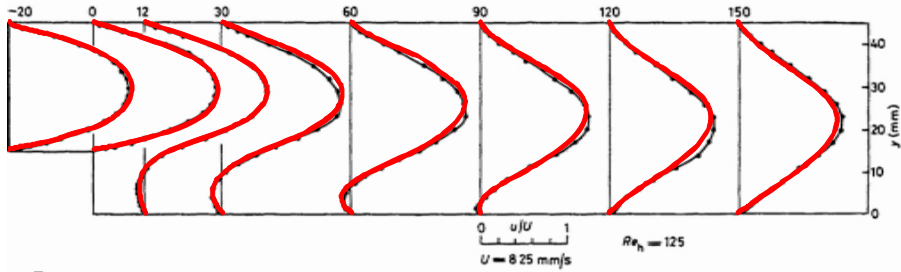


Fig. 6.5 The unilateral-sudden-expansion channel's velocity profiles predicted by Flow Simulation (red lines) in comparison with the Ref. 12 experimental data (black lines with dark circles).

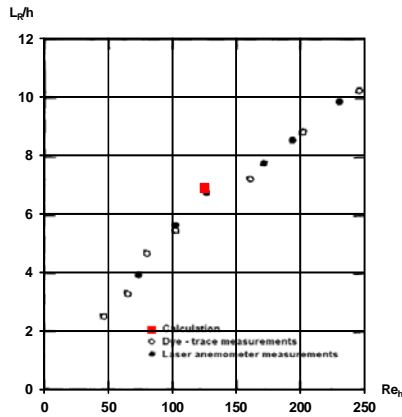


Fig. 6.6 The unilateral-sudden-expansion channel's recirculation zone length predicted by Flow Simulation (red square) in comparison with the Ref. 12 experimental data (black signs).

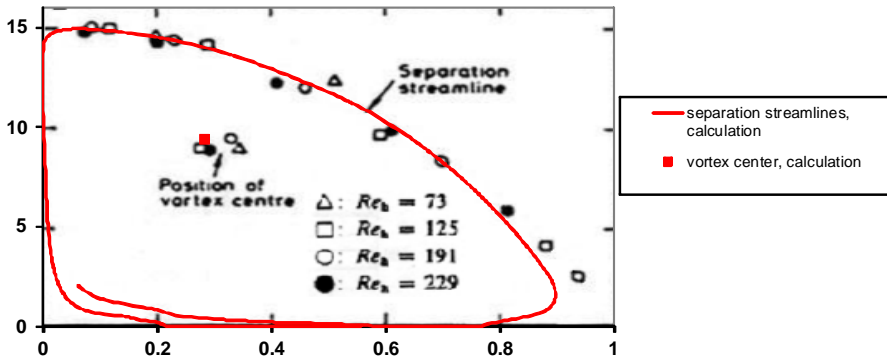


Fig. 6.7 The unilateral-sudden-expansion channel recirculation zone's separation streamlines and vortex center, both predicted by Flow Simulation (red lines and square) in comparison with the Ref. 12 experimental data (black signs).

As one can see, both the integral characteristics (hydraulic loss coefficient) and local values (velocity profiles and recirculation zone geometry) of the turbulent and laminar flow in a 2D sudden expansion channel under consideration are adequately predicted by Flow Simulation.

Flow over a Circular Cylinder

Let us now consider an external incompressible flow example. In this example, water at a temperature of 293.2 K and a pressure of 1 atm flows over a cylinder of 0.01 m or 1 m diameter. The flow pattern of this example substantially depends on the Reynolds number which is based on the cylinder diameter. At low Reynolds numbers ($4 < Re < 60$) two steady vortices are formed on the rear side of the cylinder and remain attached to the cylinder, as it is shown schematically in Fig. 7.1 (see Ref. 3).

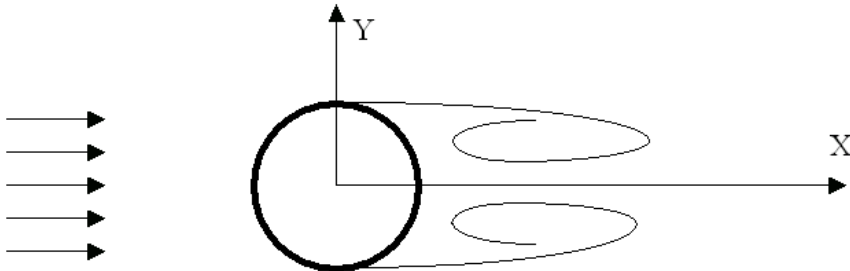


Fig. 7.1 Flow past a cylinder at low Reynolds numbers ($4 < Re < 60$).

At higher Reynolds numbers the flow becomes unstable and a von Karman vortex street appears in the wake past the cylinder. Moreover, at $Re > 60 \dots 100$ the eddies attached to the cylinder begin to oscillate and shed from the cylinder (Ref. 3). The flow pattern is shown schematically in Fig. 7.2.

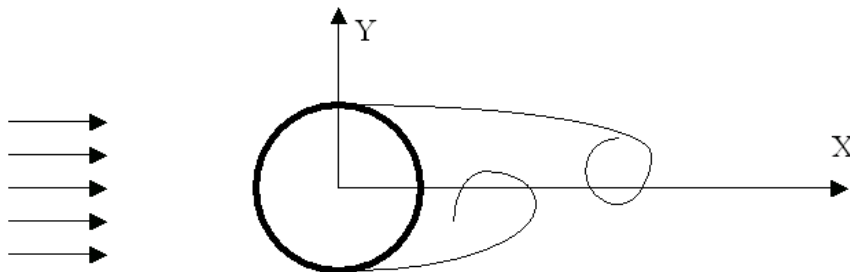


Fig. 7.2 Flow past a cylinder at Reynolds numbers $Re > 60 \dots 100$.

To calculate the 2D flow (in the X-Y plane) with Flow Simulation, the model shown in Fig. 7.3 has been created. The cylinder diameter is equal to 0.01 m at $Re \leq 10^4$ and 1 m at $Re > 10^4$. The incoming stream turbulence intensity has been specified as 0.1%. To take the flow's physical instability into account, the flow has been calculated by Flow Simulation using the time-dependent option. All the calculations have been performed at result resolution level 6.

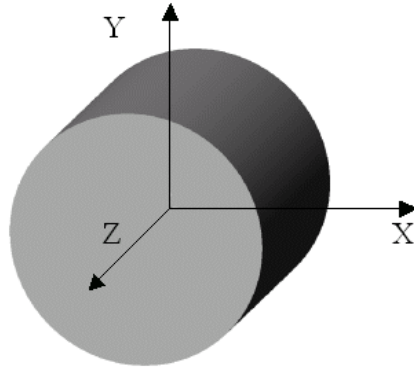


Fig. 7.3 The SOLIDWORKS model used to calculate 2D flow over a cylinder.

In accordance with the theory, steady flow patterns have been obtained in these calculations in the low Re region. An example of such calculation at $Re = 41$ is shown in Fig. 7.4 as flow trajectories over and past the cylinder in comparison with a photo of such flow from Ref. 8. It is seen that the steady vortex past the cylinder is predicted correctly.

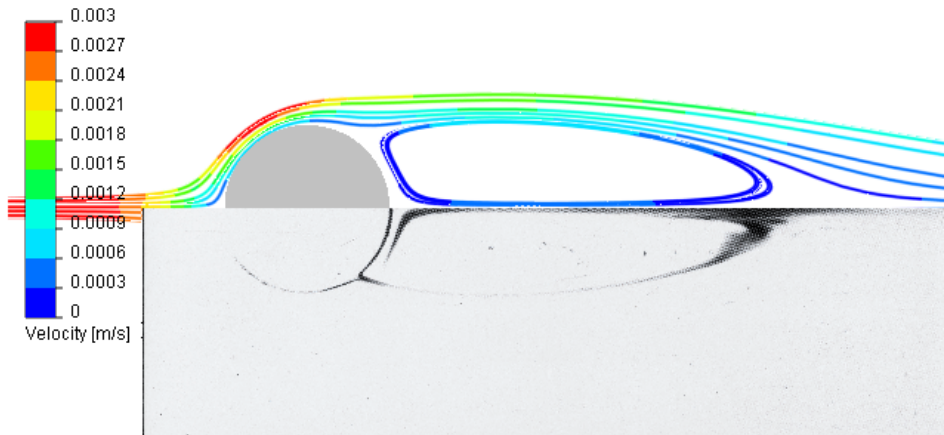


Fig. 7.4 Flow trajectories over and past a cylinder at $Re = 41$ predicted with Flow Simulation (above) in comparison with a photo of such flow from Ref. 8 (below).

The unsteady vortex shedding from a cylinder at $Re > 60..100$, yields oscillations of both drag and lateral forces acting on the cylinder and a von Karman vortex street is formed past the cylinder. An X-velocity field over and past the cylinder is shown in Fig. 7.5 The Flow Simulation prediction of the cylinder drag and lateral force oscillations' frequency in a form of Strouhal number ($St = D/(tU)$, where D is the cylinder diameter, t is the period of oscillations, and U is the incoming stream velocity) in comparison with experimental data for $Re \geq 10^3$ is shown in Fig. 7.6.

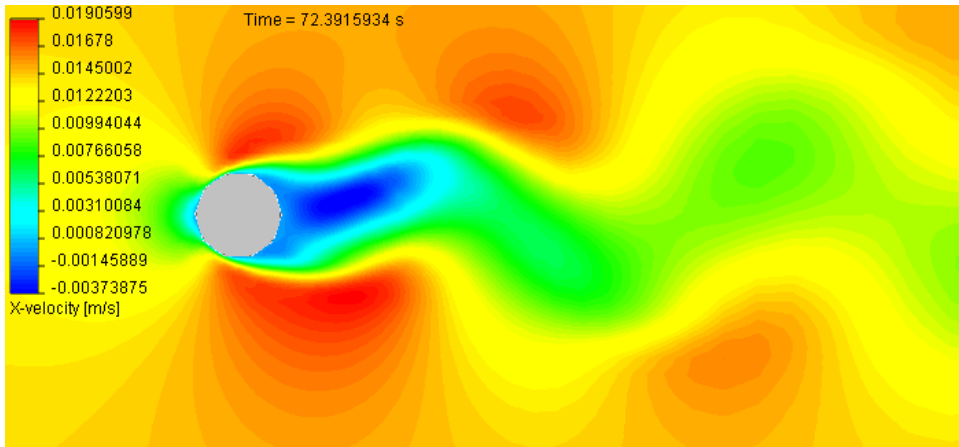


Fig. 7.5 Velocity contours of flow over and past the cylinder at $Re = 140$.

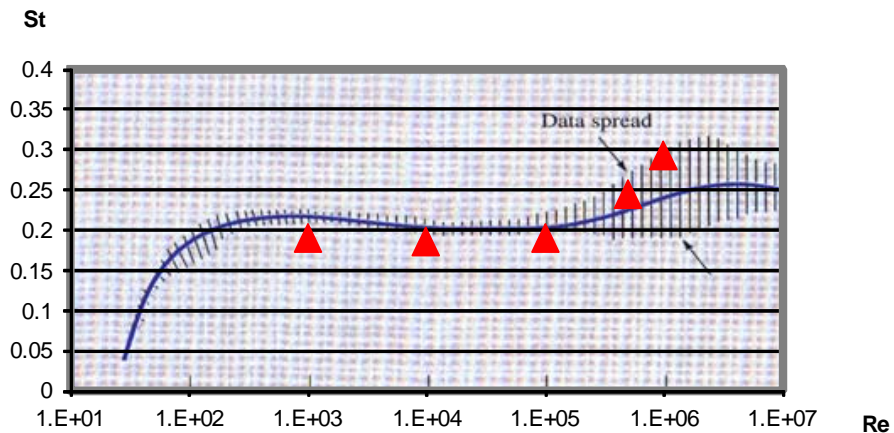


Fig. 7.6 The cylinder flow's Strouhal number predicted with Flow Simulation (red triangles) in comparison with the experimental data (blue line with dashes, Ref. 4).

The time-averaged cylinder drag coefficient is defined as

$$C_D = \frac{F_D}{\frac{1}{2} \rho U^2 D L}$$

where F_D is the drag force acting on the cylinder, $\rho U^2/2$ is the incoming stream dynamic head, D is the cylinder diameter, and L is the cylinder length. The cylinder drag coefficient, predicted by Flow Simulation is compared to the well-known $C_D(\text{Re})$ experimental data in Fig. 7.7.

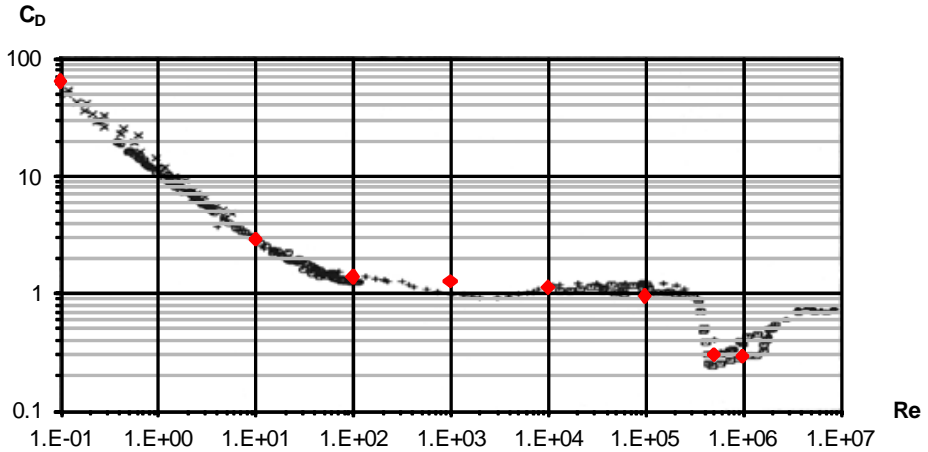


Fig. 7.7 The cylinder drag coefficient predicted by Flow Simulation (red diamonds) in comparison with the experimental data (black marks, Ref. 3)

Supersonic Flow in a 2D Convergent-Divergent Channel

Now let us consider an external supersonic flow of air in a 2D (plane) convergent-divergent channel whose scheme is shown on Fig. 8.1

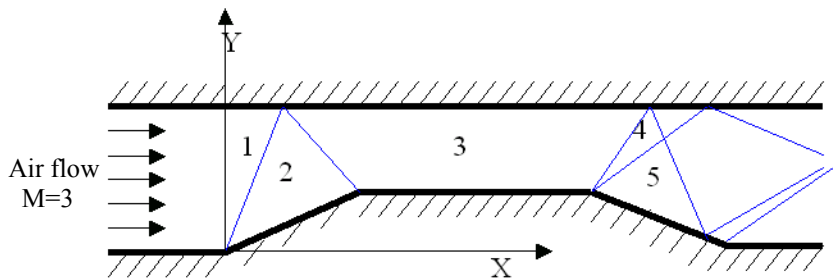


Fig. 8.1 Supersonic flow in a 2D convergent-divergent channel.

A uniform supersonic stream of air, having a Mach number $M = 3$, static temperature of 293.2 K, and static pressure of 1 atm, is specified at the channel inlet between two parallel walls. In the next convergent section (see Fig. 8.2) the stream decelerates through two oblique shocks shown schematically in Fig. 8.1 as lines separating regions 1, 2, and 3. Since the convergent section has a special shape adjusted to the inlet Mach number, so the shock reflected from the upper plane wall and separating regions 2 and 3 comes to the section 3 lower wall edge, a uniform supersonic flow occurs in the next section 3 between two parallel walls. In the following divergent section the supersonic flow accelerates thus forming an expansion waves fan 4. Finally, the stream decelerates in the exit channel section between two parallel walls when passing through another oblique shock.

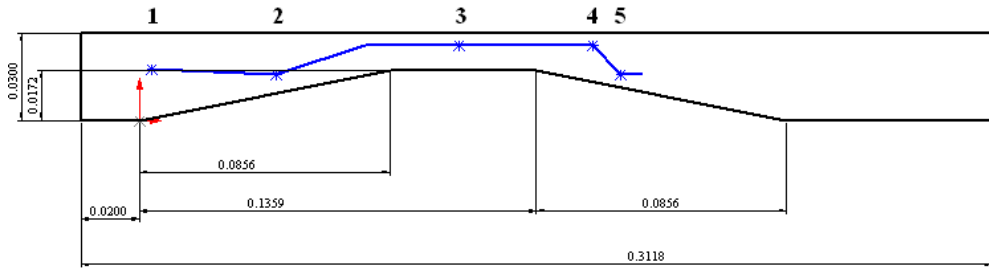


Fig. 8.2 Dimensions (in m) of the 2D convergent-divergent channel including a reference line for comparing the Mach number.

The SOLIDWORKS model of this 2D channel is shown in Fig. 8.3

Since the channel was designed for the inviscid flow of an ideal gas, the ideal wall boundary condition has been specified and the laminar only flow has been considered instead of turbulent. The computed Mach number along the reference line and at the reference points (1-5) are compared with the theoretical values in Fig. 8.4.

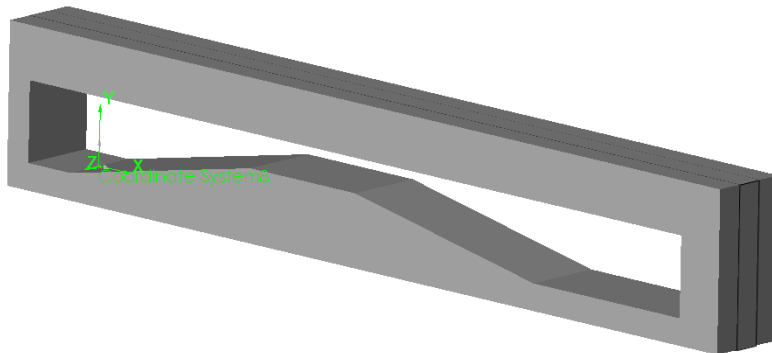


Fig. 8.3 The model for calculating the 2D supersonic flow in the 2D convergent-divergent channel with Flow Simulation.

To obtain the most accurate results possible with Flow Simulation, the calculations have been performed at result resolution level 6. The predicted Mach number at the selected channel points (1-5) and along the reference line (see Fig. 8.2), are presented in Table 8.1 and Fig. 8.4 respectively.

Table 8.1 Mach number values predicted with Flow Simulation with comparison to the theoretical values at the reference points.

Point	1	2	3	4	5
X coordinate of point, m	0.0042	0.047	0.1094	0.155	0.1648
Y coordinate of point, m	0.0175	0.0157	0.026	0.026	0.0157
Theoretical M	3.000	2.427	1.957	2.089	2.365
Flow Simulation prediction of M	3.000	2.429	1.965	2.106	2.380
Prediction error, %	0.0	0.1	0.4	0.8	0.6

From Table 8.1 and Fig. 8.4 it can be seen that the Flow Simulation predictions are very close to the theoretical values. In Fig. 8.4 one can see that Flow Simulation properly predicts the abrupt parameter changes when the stream passes through the shock and a fast parameter change in the expansion fan.

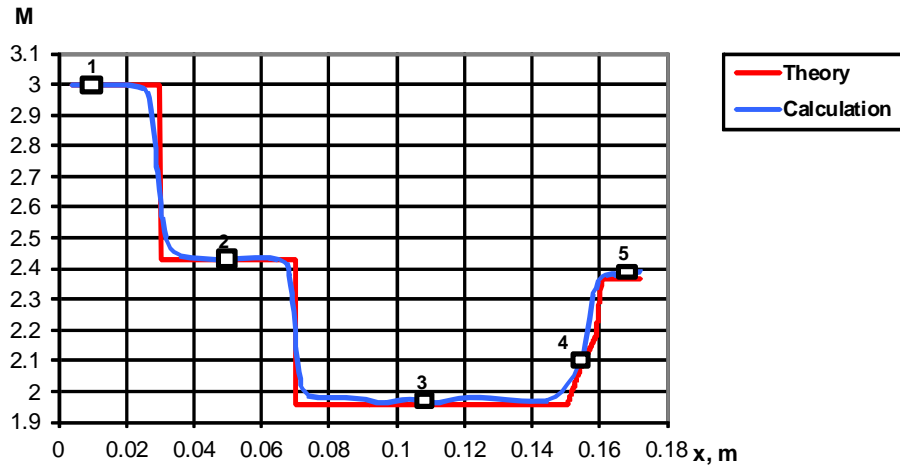


Fig. 8.4 Mach number values predicted with Flow Simulation along the reference line (the reference points on it are marked by square boxes with numbers) in comparison with the theoretical values.

To show the full flow pattern, the predicted Mach number contours of the channel flow are shown in Fig. 8.5.

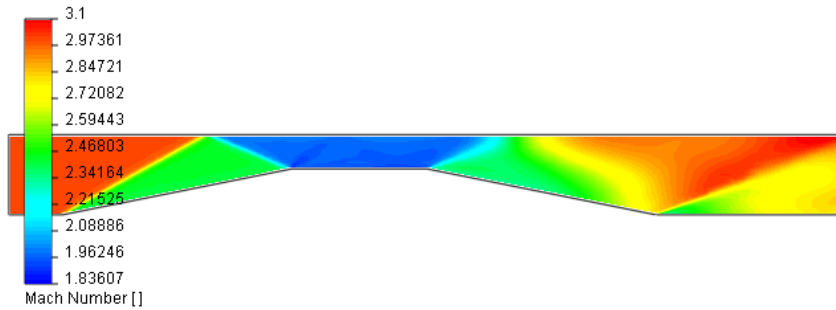


Fig. 8.5 Mach number contours predicted by Flow Simulation.

This example illustrates that Flow Simulation is capable of capturing shock waves with a high degree of accuracy. This high accuracy is possible due to the Flow Simulation solution adaptive meshing capability. Solution adaptive meshing automatically refines the mesh in regions with high flow gradients such as shocks and expansion fans.

Supersonic Flow over a Segmental Conic Body

Now let us consider an external supersonic flow of air over a segmental conic body shown in Fig. 9.1. The general case is that the body is tilted at an angle of α with respect to the incoming flow direction. The dimensions of the body whose longitudinal (in direction t , see Fig. 9.1) and lateral (in direction n) aerodynamic drag coefficients, as well as longitudinal (with respect to Z axis) torque coefficient, were investigated in Ref. 5 are presented in Fig. 9.2. They were determined from the dimensionless body sizes and the Reynolds number stated in Ref. 5.

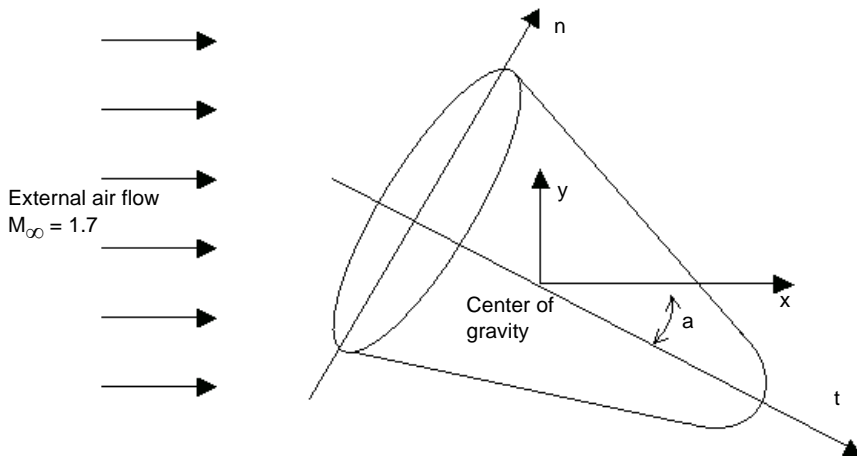


Fig. 9.1 Supersonic flow over a segmental conic body.

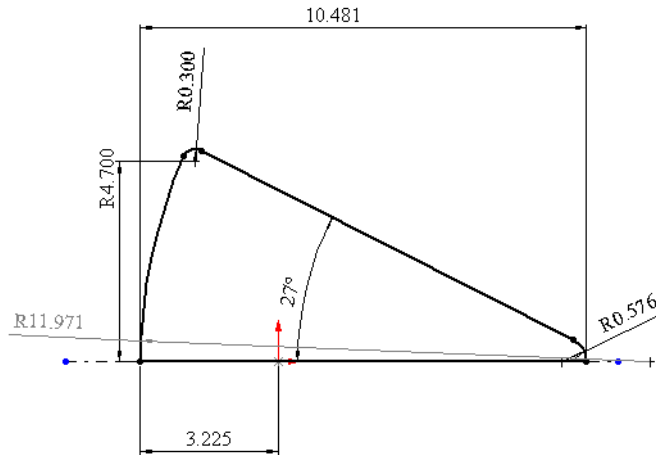


Fig. 9.2 Model sketch dimensioned in centimeters.

The model of this body is shown in Fig. 9.3.

To compare the Flow Simulation predictions with the experimental data of Ref. 5, the calculations have been performed for the case of incoming flow velocity of Mach number 1.7. The undisturbed turbulent incoming flow has a static pressure of 1 atm, static temperature of 660.2 K, and turbulence intensity of 1%. The flow Reynolds number of $1.7 \cdot 10^6$ (defined with respect to the body frontal diameter) corresponds to these conditions, satisfying the Ref. 5 experimental conditions.

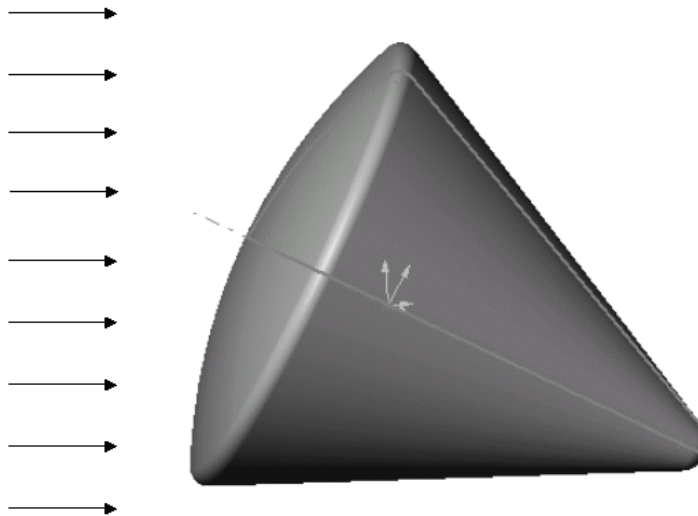


Fig. 9.3 The SOLIDWORKS model for calculating the 3D flow over the 3D segmental conic body with Flow Simulation.

To compare the flow prediction with the experimental data of Ref. 5, the calculations have been performed for the body tilted at $\alpha = 0^\circ, 30^\circ, 60^\circ, 90^\circ, 120^\circ, 150^\circ$ and 180° angles. To reduce the computational resources, the $Z = 0$ flow symmetry plane has been specified in all of the calculations. Additionally, the $Y = 0$ flow symmetry plane has been specified at $\alpha = 0^\circ$ and 180° .

The calculations have been performed at result resolution level 6.

The comparison is performed on the following parameters:

- longitudinal aerodynamic drag coefficient,

$$C_t = \frac{F_t}{\frac{1}{2} \rho U^2 S} ,$$

where F_t is the aerodynamic drag force acting on the body in the t direction (see Fig. 9.1), $\rho U^2/2$ is the incoming stream dynamic head, S is the body frontal cross section (being perpendicular to the body axis) area;

- lateral aerodynamic drag coefficient,

$$C_n = \frac{F_n}{\frac{1}{2} \rho U^2 S} ,$$

where F_n is the aerodynamic drag force acting on the body in the n direction (see Fig. 9.1), $\rho U^2/2$ is the incoming stream dynamic head, S is the body frontal cross section (being perpendicular to the body axis) area;

- on the longitudinal (with respect to Z axis) aerodynamic torque coefficient,

$$m_z = \frac{M_z}{\frac{1}{2} \rho U^2 S L} ,$$

where M_z is the aerodynamic torque acting on the body with respect to the Z axis (see Fig. 9.1), $\rho U^2/2$ is the incoming stream dynamic head, S is the body frontal cross section (being perpendicular to the body axis) area, L is the reference length.

The calculation results are presented in Figs. 9.4 and 9.5.

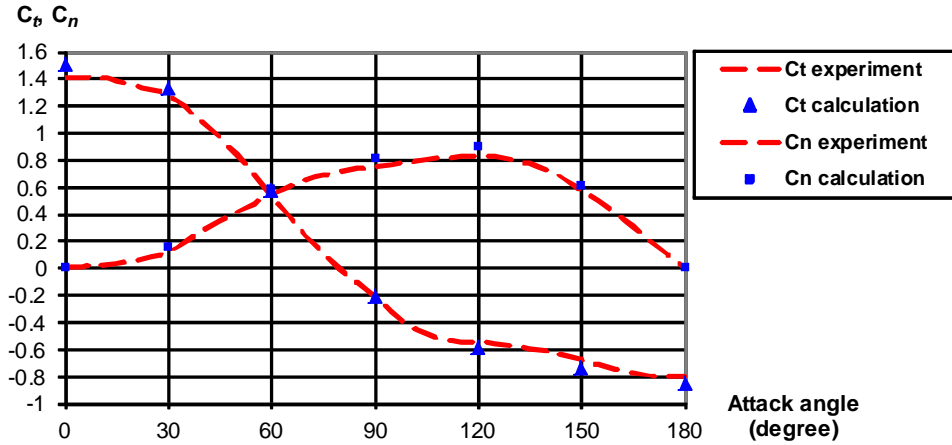


Fig. 9.4 The longitudinal and lateral aerodynamic drag coefficients predicted with Flow Simulation and measured in the experiments of Ref. 5 versus the body tilting angle.

From Fig. 9.4, it is seen that the Flow Simulation predictions of both C_n and C_t are excellent.

As for the longitudinal aerodynamic torque coefficient (m_z) prediction, it is also close to the experimental data of Ref. 5, especially if we take into account the measurements error.

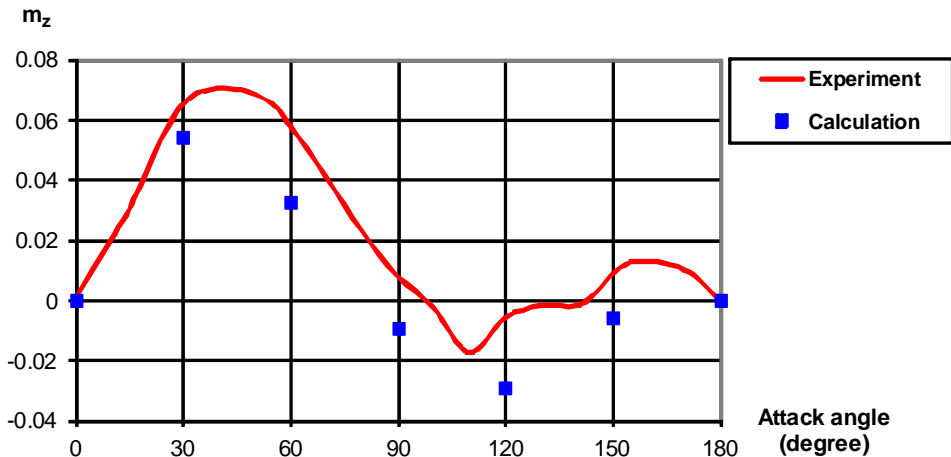


Fig. 9.5 The longitudinal aerodynamic torque coefficient predicted with Flow Simulation and measured in the experiments (Ref. 5) versus the body tilting angle.

To illustrate the quantitative predictions with the corresponding flow patterns, the Mach number contours are presented in Figs. 9.6, 9.7, and 9.8. All of the flow patterns presented on the figures include both supersonic and subsonic flow regions. The bow shock consists of normal and oblique shock parts with the subsonic region downstream of the normal

shock. In the head subsonic region the flow gradually accelerates up to a supersonic velocity and then further accelerates in the expansion fan of rarefaction waves. The subsonic wake region past the body can also be seen.

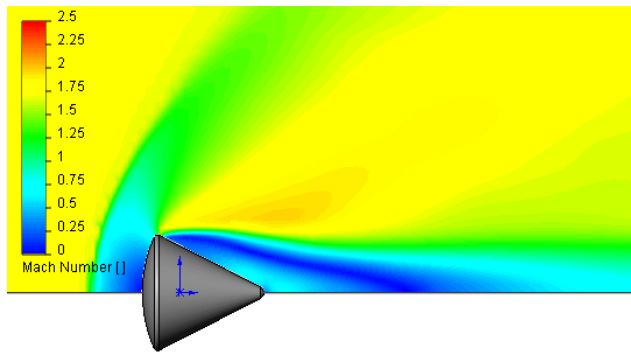


Fig. 9.6 Mach number contours at $\alpha = 0^\circ$.

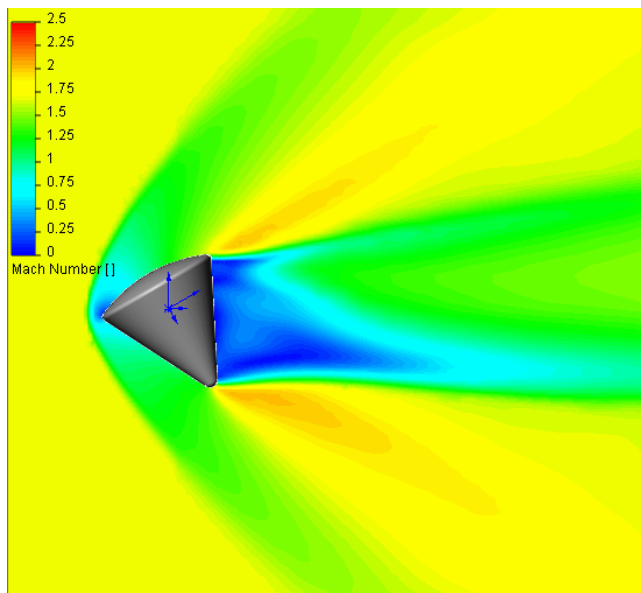


Fig. 9.7 Mach number contours at $\alpha = 60^\circ$.

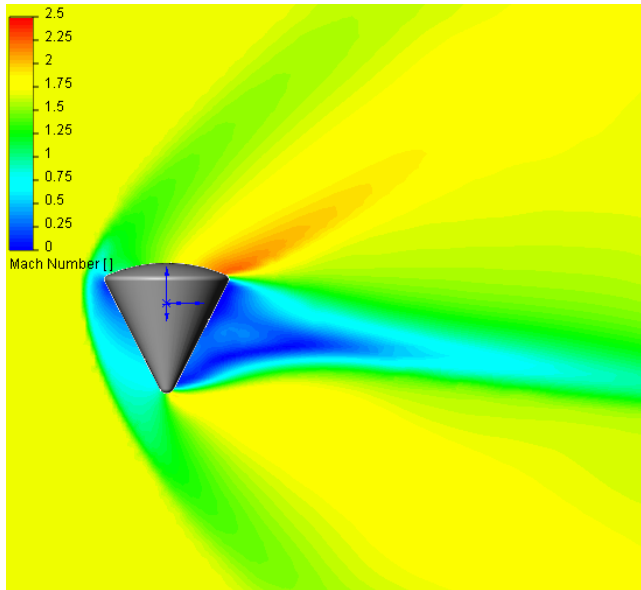


Fig. 9.8 Mach number contours at $\alpha = 90^\circ$.

As the forward part becomes sharper, the normal part of the bow shock and the corresponding subsonic region downstream of it become smaller. In the presented pictures, the smallest nose shock (especially its subsonic region) is observed at $\alpha = 60^\circ$.

Flow over a Heated Plate

Now let us consider a uniform 2D flows with a laminar boundary layer on a heated flat plate, see Fig. 10.1. The incoming uniform air stream has a velocity of 1.5 m/s, a temperature of 293.2 K, and a static pressure of 1 atm. Thus, the flow Reynolds number defined on the incoming flow characteristics and on the plate length of 0.31 m is equal to $3.1 \cdot 10^4$, therefore the boundary layer beginning from the plate's leading edge is laminar (see Ref. 6).

Then, let us consider the following three cases:

Case #1

The plate over its whole length (within the computational domain) is 10°C warmer than the incoming air (303.2 K), both the hydrodynamic and the thermal boundary layer begin at the plate's leading edge coinciding with the computational domain boundary;

Case #2

The upstream half of the plate (i.e. at $x \sim 0.15$ m) has a fluid temperature of 293.2 K, and the downstream half of the plate is 10°C warmer than the incoming air (303.2 K), the hydrodynamic boundary layer begins at the plate's leading edge coinciding with the computational boundary;

Case #3

Plate temperature is the same as in case #1, the thermal boundary layer begins at the inlet computational domain boundary, whereas the hydrodynamic boundary layer at the inlet computational domain boundary has a non-zero thickness which is equal to that in case #2 at the thermal boundary layer starting.

The calculation goal is to predict the local coefficient of heat transfer from the wall to the fluid, as well as the local skin-friction coefficient.

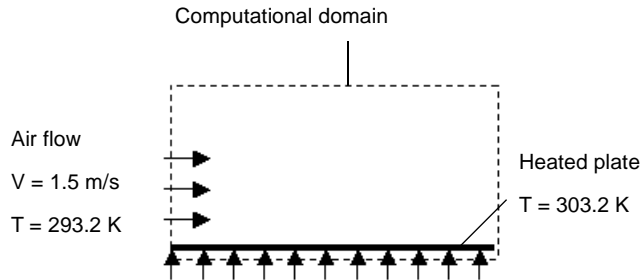


Fig. 10.1 Laminar flow over a heated flat plate.

The geometry model used for calculating the 2D flow over the heated flat plate with Flow Simulation is shown in Fig. 10.2. The problem is solved as internal in order to avoid the conflict situation when the external flow boundary with ambient temperature conditions intersects the wall with a thermal boundary layer.

To avoid any influence of the upper wall on the flow near the heated lower wall, the ideal wall boundary condition has been specified on the upper wall. To solve the internal problem, the incoming fluid velocity is specified at the channel inlet, whereas the fluid static pressure is specified at the channel exit. To specify the external flow features, the incoming stream's turbulent intensity is set to 1% and the turbulent length is set to 0.01 m, i.e., these turbulent values are similar to the default values for external flow problems.

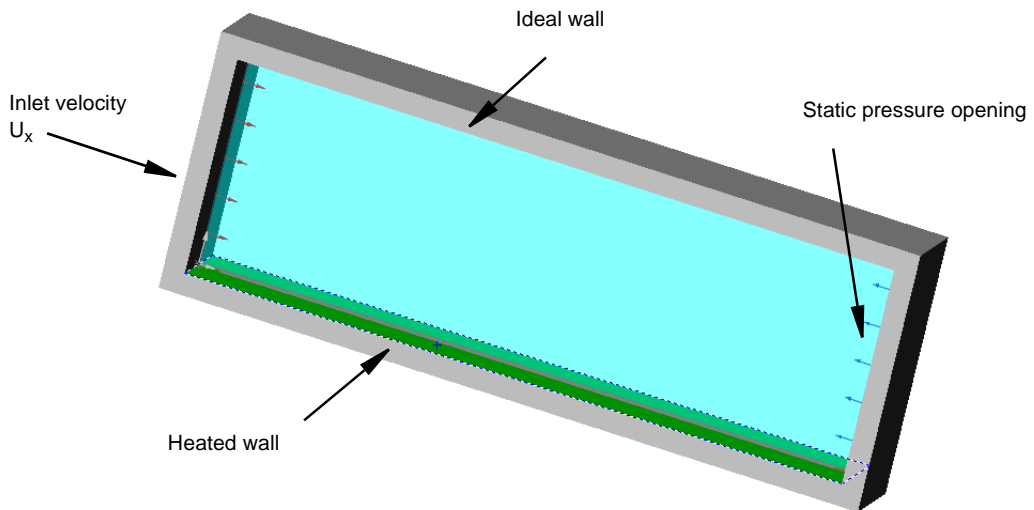


Fig. 10.2 The geometry model used for calculating the 2D flow over heated flat plate with Flow Simulation.

The heat transfer coefficient h and the skin-friction coefficient C_f are Flow Simulation output flow parameters. The theoretical values for laminar flow boundary layer over a flat plate, in accordance with Ref. 6 can be determined from the following equations:

$$h = \frac{kNu_x}{x} ,$$

where

k is the thermal conductivity of the fluid,

x is the distance along the wall from the start of the hydrodynamic boundary layer,

Nu_x is the Nusselt number defined on a heated wall as follows:

$$Nu_x = 0.332 \cdot Pr^{1/3} Re_x^{1/2}$$

for a laminar boundary layer if it's starting point coincides with the thermal boundary layer starting point, and

$$Nu_x = \frac{0.332 \cdot Pr^{1/3} Re_x^{1/2}}{\sqrt[3]{1 - (x_0/x)^{3/4}}}$$

for a laminar boundary layer if the thermal boundary layer begins at point x_0 lying downstream of the hydrodynamic boundary layer starting point, in this case Nu_x is defined at $x > x_0$ only;

where $Pr = \frac{\mu C_p}{k}$ is the Prandtl number, μ is the fluid dynamic viscosity, C_p is the

fluid specific heat at constant pressure, $Re_x = \frac{\rho Vx}{\mu}$ is the Reynolds number

defined on x , ρ is the fluid density, and V is the fluid velocity;

$$C_{fx} = \frac{0,664}{\sqrt{Re_x}} \text{ at } Re_x \leq 5 \cdot 10^5 , \text{ i.e., with a laminar boundary layer.}$$

As for the hydrodynamic boundary layer thickness δ needed for specification at the computational domain boundary in case #3, in accordance with Ref. 6, it has been

determined from the following equation: $\delta = 4.64 \cdot x / Re_x^{0.5}$, so $\delta = 0.00575$ m in this case. For these calculations all fluid parameters are determined at the outer boundary of the boundary layer.

The Flow Simulation predictions of h and C_f performed at result resolution level 7, and the theoretical curves calculated with the formulae presented above are shown in Figs. 10.3 and 10.4. It is seen that the Flow Simulation predictions of the heat transfer coefficient and the skin-friction coefficient are in excellent agreement with the theoretical curves.

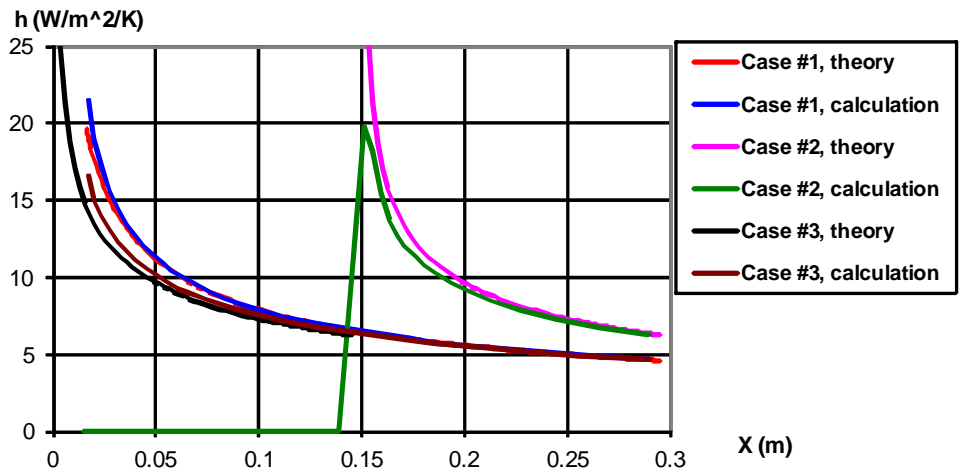


Fig. 10.3 Heat transfer coefficient change along a heated plate in a laminar boundary layer: Flow Simulation predictions compared to theory.

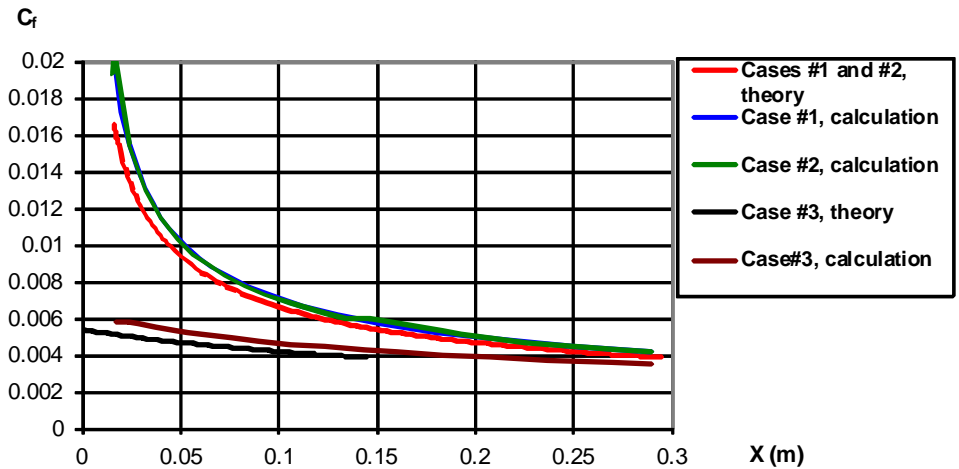


Fig. 10.4 Skin-friction coefficient change along a heated plate in a laminar boundary layer: Flow Simulation predictions compared to theory.

Convection and Radiation in an Annular Tube

We will now consider incompressible laminar flow in a portion of an annular tube, whose outer shell is a heat source having constant heat generation rate Q_1 with a heat-insulated outer surface, and whose central body fully absorbs the heat generated by the tube's outer shell (i.e. the negative heat generation rate Q_2 is specified in the central body); see Fig. 11.1. (The tube model is shown in Fig. 11.2). We will assume that this tube is rather long, so the tube's $L = 1$ m portion under consideration has fully developed fluid velocity and temperature profiles at the inlet, and, since the fluid properties are not temperature-dependent, the velocity profile also will not be temperature-dependent.

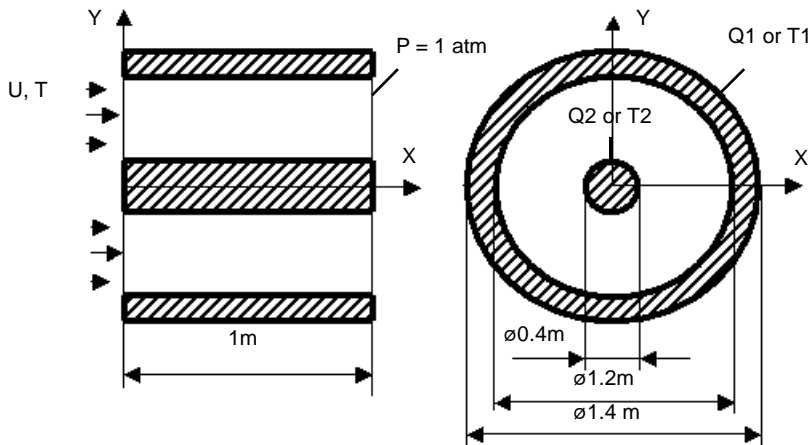


Fig. 11.1 Laminar flow in a heated annular tube.

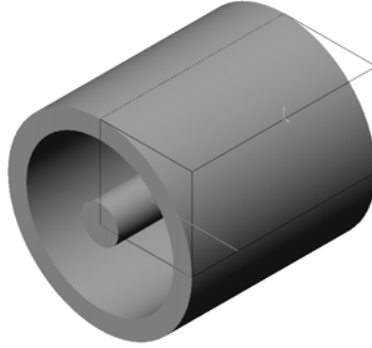


Fig. 11.2 A model created for calculating 3D flow within a heated annular tube using Flow Simulation.

To validate the Flow Simulation capability for solving conjugate heat transfer problems both with and without radiation, let us solve the following three problems:

- 1 a conjugate heat transfer problem with convection only,
- 2 radiation heat transfer only problem, and
- 3 a conjugate heat transfer problem with both convection and radiation.

In the first problem we specify $Q_2 = -Q_1$, so the convective heat fluxes at the tube inner and outer walls are constant along the tube. The corresponding laminar annular pipe flow's fully developed velocity and temperature profiles, according to Ref. 6, are expressed analytically as follows:

$$u(r) = \varphi \cdot \left[\left(\frac{r}{r_2} \right)^2 - \left(\left(\frac{r_1}{r_2} \right)^2 - 1 \right) \frac{\ln(r/r_2)}{\ln(r_1/r_2)} - 1 \right],$$

$$T(r) = T_2 - \frac{q_2}{k} r_2 \ln \left(\frac{r}{r_2} \right),$$

$$\text{where } \varphi = \frac{2 \bar{u}}{\left(\left(\frac{r_1}{r_2} \right)^2 - 1 \right) / \ln(r_1/r_2) - \left(\frac{r_1}{r_2} \right)^2 - 1},$$

u is the fluid velocity,

T is the fluid temperature,

r is the radial coordinate,

r_1 and r_2 are the tube outer shell's inner radius and tube's central body radius, respectively,

\bar{u} is the volume-average velocity, defined as the volume flow rate divided by the tube cross-section area,

q_2 is the the heat flux from the fluid to the tube's central body,

k is the fluid thermal conductivity,

T_2 is the surface temperature of the central body.

The heat flux from the fluid to the tube's central body (negative, since the heat comes from the fluid to the solid) is equal to

$$q_2 = k \left(\frac{\partial T}{\partial r} \right)_{r=r_2} = \frac{Q_2}{2\pi \cdot r_2 \cdot L}$$

Let $Q_1 = -Q_2 = 107.235 \text{ W}$ and $\bar{u} \approx 13.59 \text{ m/s}$ ($\varphi = -10 \text{ m/s}$), the fluid has the following properties: $k = 0.5 \text{ W/(m}\cdot\text{K)}$, $C_p = 500 \text{ J/(kg}\cdot\text{K)}$, $\mu = 0.002 \text{ Pa}\cdot\text{s}$, $\rho = 0.1 \text{ kg/m}^3$. Since the corresponding (defined on the equivalent tube diameter) Reynolds number $Re_d \approx 815$ is rather low, the flow has to be laminar. We specify the corresponding velocity and temperature profiles as boundary conditions at the model inlet and as initial conditions, and $P_{\text{out}} = 1 \text{ atm}$ as the tube outlet boundary condition.

To reduce the computational domain, let us set $Y = 0$ and $X = 0$ flow symmetry planes (correspondingly, the specified Q_1 and Q_2 values are referred to the tube section's quarter lying in the computational domain). The calculation have been performed at result resolution level 6.

The fluid temperature profile predicted at 0.75 m from the tube model inlet is shown in Fig. 11.3 together with the theoretical curve.

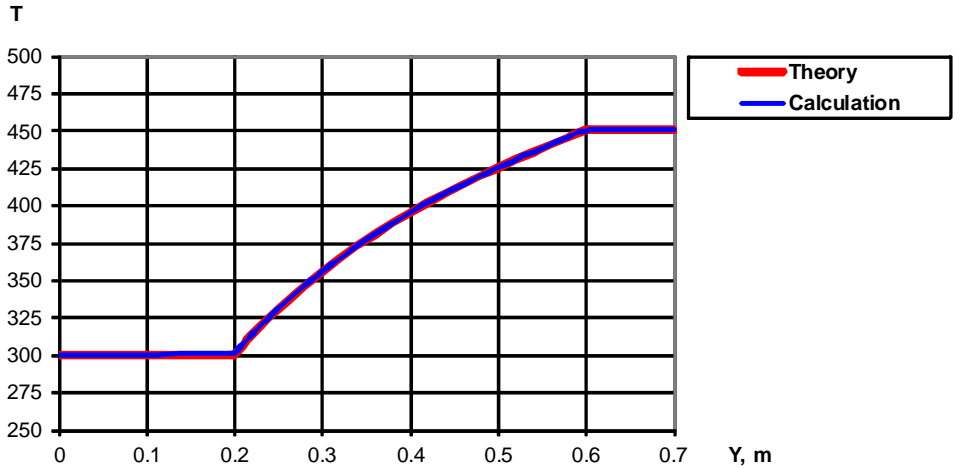


Fig. 11.3 Fluid temperature profiles across the tube in the case of convection only, predicted with Flow Simulation and compared to the theoretical curve.

It is seen that this prediction practically coincides with the theoretical curve.

Before solving the third problem coupling convection and radiation, let us determine the radiation heat fluxes between the tube's outer and inner walls under the previous problem's wall temperatures. In addition to holding the outer shell's temperature at 450 K and the central body's temperature at 300 K as the volume sources, let us specify the emissivity of $\varepsilon_1 = 0.95$ for the outer shell and $\varepsilon_2 = 0.25$ for the central body. To exclude any convection, let us specify the liquid velocity of 0.001 m/s and thermal conductivity of 10^{-20} W/(m·K).

Let J_2 denote the radiation rate leaving the central body, and G_2 denotes the radiation rate coming to the central body, therefore $Q_{2r} = J_2 - G_2$ (the net radiation rate from the central body). In the same manner, let J_1 denote the radiation rate leaving the outer shell's inner surface, and G_1 denote the radiation rate coming to the outer shell's inner surface, therefore $Q_{1r} = J_1 - G_1$ (the net radiation rate from the outer shell's inner surface). These radiation rates can be determined by solving the following equations:

$$J_2 = A_2 \sigma \varepsilon_2 T_2^4 + G_2(1 - \varepsilon_2),$$

$$G_2 = J_1 F_{1-2},$$

$$J_1 = A_1 \sigma \varepsilon_1 T_1^4 + G_1(1 - \varepsilon_1),$$

$$G_1 = J_2 F_{2-1} + J_1 F_{1-1},$$

where $\sigma = 5.669 \cdot 10^{-8}$ W/m²·K⁴ is the Stefan-Boltzmann constant, F_{1-2} , F_{2-1} , F_{1-1} are these surfaces' radiation shape factors, under the assumption that the leaving and incident radiation fluxes are uniform over these surfaces, Ref. 6 gives the following formulas:

$$F_{1-2} = (1/X) - (1/\pi X) \{ \arccos(B/A) - (1/2Y) [(A^2 + 4A - 4X^2 + 4)^{1/2} \arccos(B/X/A) + B \cdot \arcsin(1/X) - \pi A/2] \},$$

$$F_{1-1} = 1 - (1/X) + (2/\pi X) \arctan[2(X^2 - 1)^{1/2}/Y] - (Y/2/\pi X) \{ [(4X^2 + Y^2)^{1/2}/Y] \arcsin\{[4(X^2 - 1) + (Y/X)^2(X^2 - 2)]/[Y^2 + 4(X^2 - 1)]\} - \arcsin[(X^2 - 2)/X^2] + (\pi/2)[(4X^2 + Y^2)^{1/2}/Y - 1] \}$$

$$F_{2-1} = F_{1-2} \cdot A_1/A_2, \text{ where } X = r_1/r_2, Y = L/r_2, A = X^2 + Y^2 - 1, B = Y^2 - X^2 + 1.$$

These net and leaving radiation rates (over the full tube section surface), both calculated by solving the equations analytically and predicted by Flow Simulation at result resolution level 6, are presented in Table 11.1.

Table 11.1 Radiation rates predicted with Flow Simulation with comparison to the theoretical values.

Parameter	Theory (Ref.6), W	Flow Simulation predictions	
		Value, W	Prediction error, %
Q2 r	-383.77	-388.30	1.2%
J2 r	1728.35	1744.47	0.9%
Q1 r	4003.68	3931.87	-1.8%
J1 r	8552.98	8596.04	0.5%

It is seen that the prediction errors are quite small. To validate the Flow Simulation capabilities on the third problem, which couples convection and radiation, let us add the theoretical net radiation rates, Q_{1r} and Q_{2r} scaled to the reduced computational domain, i.e., divided by 4, to the Q_1 and Q_2 values specified in the first problem. Let us specify $Q_1 = 1108.15$ W and $Q_2 = -203.18$ W, so theoretically we must obtain the same fluid temperature profile as in the first considered problem.

The fluid temperature profile predicted at 0.75 m from the tube model inlet at the result resolution level 6 is shown in Fig. 11.4 together with the theoretical curve. It is seen that once again this prediction virtually coincides with the theoretical curve.

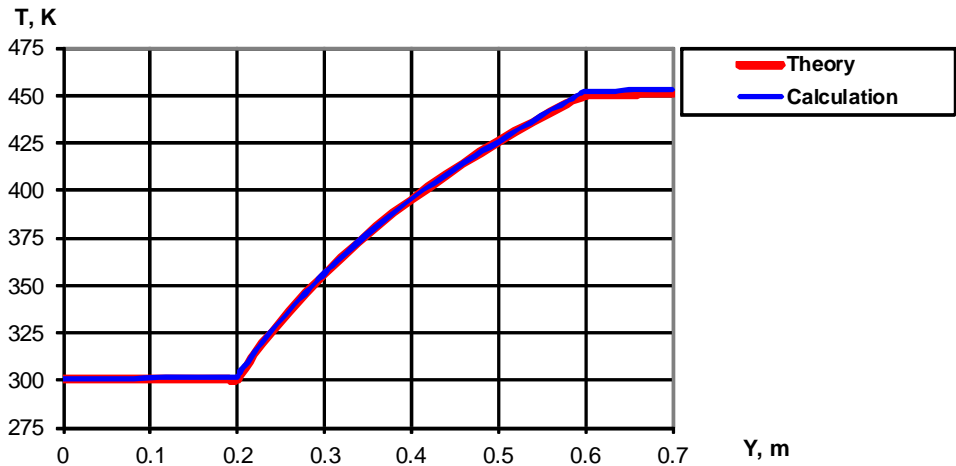


Fig. 11.4 Fluid temperature profiles across the tube in the case coupling convection and radiation, predicted with Flow Simulation and compared to the theoretical curve.

Pin-fin Heat Sink Cooling by Natural Convection

Heat sinks play an important role in electronics cooling. Following the experimental work presented in Ref. 14 and numerical study presented in Ref. 16, let us consider heat transfer from an electrically heated thermofoil which is mounted flush on a plexiglass substrate, coated by an aluminum pin-fin heat sink with a 9x9 pin fin array, and placed in a closed plexiglass box. In order to create more uniform ambient conditions for this box, it is placed into another, bigger, plexiglass box and attached to the heat-insulated thick wall, see Figs. 12.1, 12.2. Following Ref. 14, let us consider the vertical position of these boxes, as it is shown in Fig. 12.1 (c) (here, the gravity acts along the Y axis).

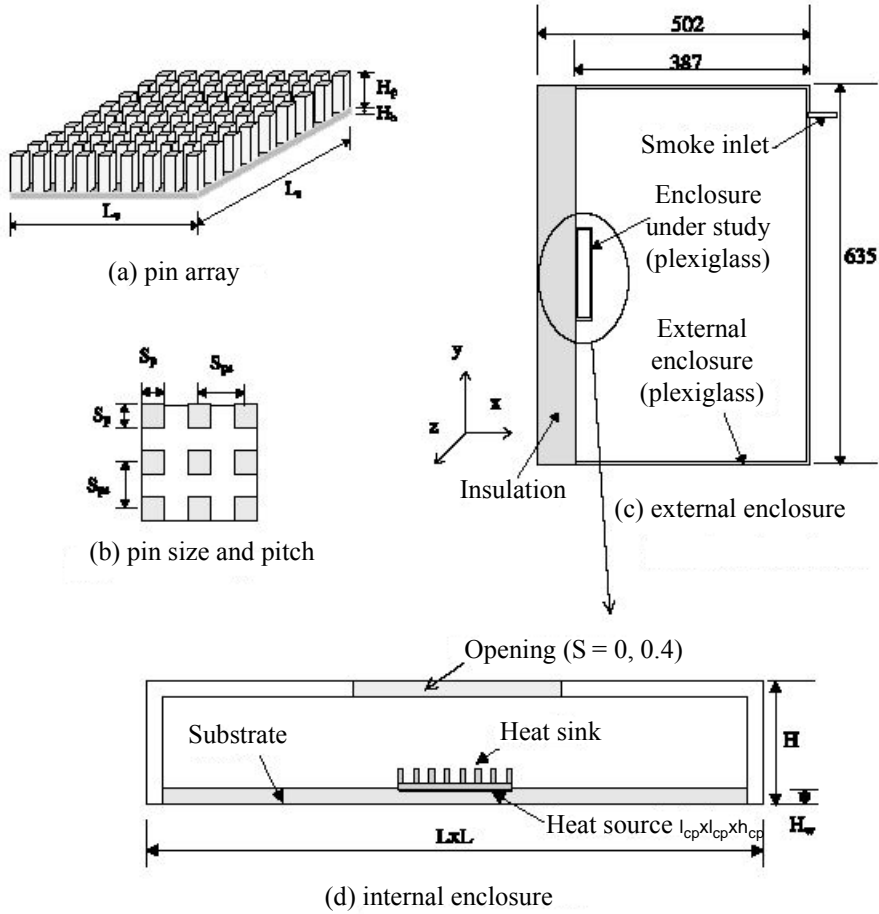


Fig. 12.1 The pin-fin heat sink nestled within two plexiglass boxes: $l_{cp} = L_s = 25.4$ mm, $h_{cp} = 0.861$ mm, $H_p = 5.5$ mm, $H_b = 1.75$ mm, $S_p = 1.5$ mm, $S_{ps} = L_s/8$, $L = 127$ mm, $H = 41.3$ mm, $H_w = 6.35$ mm (from Ref. 14).

The corresponding model used in the calculations is shown in Fig. 12.2. In this model's coordinate system the gravitational acceleration vector is directed along the X axis. The computational domain envelopes the outer surface of the external box, and the $Z = 0$ symmetry plane is used to reduce the required computer resources.

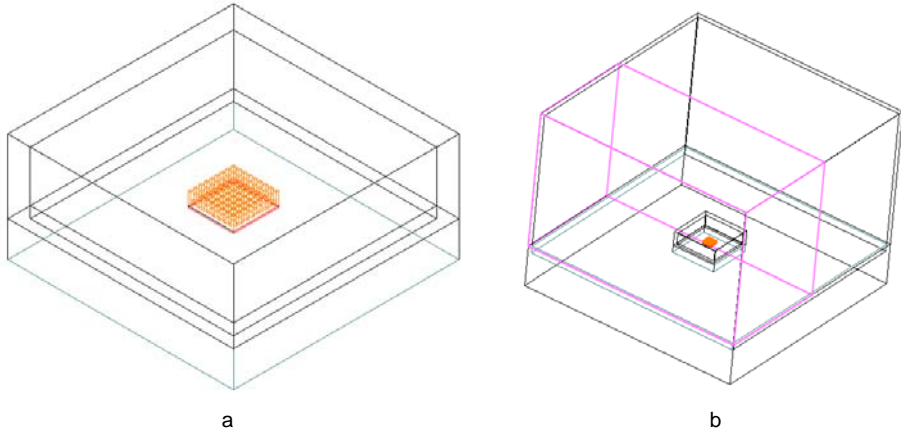


Fig. 12.2 A model created for calculating the heat transfer from the pin-fin heat sink through the two nested boxes into the environment: (a) the internal (smaller) box with the heat sink; (b) the whole model.

According to Ref. 14, both the heat sink and the substrate are coated with a special black paint to provide a surface emissivity of 0.95 (the other plexiglass surfaces are also opaque, diffuse and gray, but have an emissivity of 0.83).

The maximum steady-state temperature T_{max} of the thermofoil releasing the heat of known power Q was measured. The constant ambient temperature T_a was measured at the upper corner of the external box. As a result, the value of

$$R_{ja} = (T_{max} - T_a)/Q \quad (12.1)$$

was determined at various Q (in the 0.1...1 W range).

The ambient temperature is not presented in Ref. 14, so, proceeding from the suggestion that the external box in the experiment was placed in a room, we have varied the ambient temperature in the relevant range of 15...22°C. Since R_{ja} is governed by the temperature difference $T_{max} - T_a$, (i.e. presents the two boxes' thermal resistance), the ambient temperature range only effects the resistance calculations by 0.6°C/W at $Q = 1$ W, (i.e. by 1.4% of the experimentally determined R_{ja} value that is 43°C/W). As for the boundary conditions on the external box's outer surface, we have specified a heat transfer coefficient of 5.6 W/m² K estimated from Ref. 15 for the relevant wind-free conditions and an ambient temperature lying in the range of 15...22°C (additional calculations have shown that the variation of the constant ambient temperature on this boundary yield nearly identical results). As a result, at $Q = 1$ W (the results obtained at the other Q values are shown in Ref. 16) and $T_a = 20^\circ\text{C}$ we have obtained $R_{ja} = 41^\circ\text{C/W}$, i.e. only 5% lower than the experimental value.

The flow streamlines visualized in Ref. 14 using smoke and obtained in the calculations are shown in Fig. 12.3

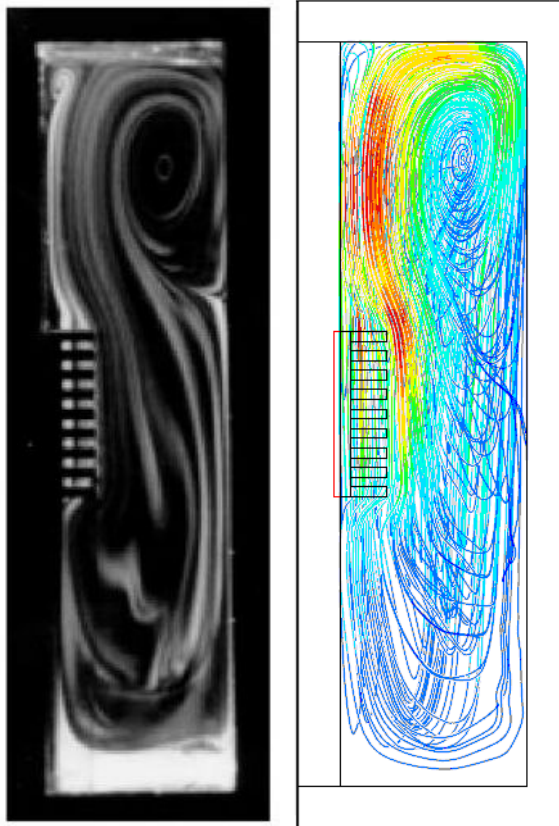


Fig. 12.3 Flow streamlines visualized by smoke in the Ref. 14 experiments (left) and obtained in the calculations (colored in accordance with the flow velocity values) (right).

Plate Fin Heat Sink Cooling by Forced Convection

This validation example demonstrates Flow Simulation capabilities to simulate forced air cooling of plate fin heat sink placed in a wind tunnel. The calculations are based on the experimental results from Ref. 17, where several flow regimes were considered.

Heat sink geometry with its main dimensions is shown in Fig. 13.1. The dimension values were set as follows: fin height (H) of 10 mm, thickness of 1.5 mm and fin-to-fin distance (δ) of 5 mm while the heat sink width (B) and length were 52.8 mm and the base thickness was 3 mm. The wind tunnel width (CB), height (CH) and length were 160 mm, 15 mm and 200 mm respectively.

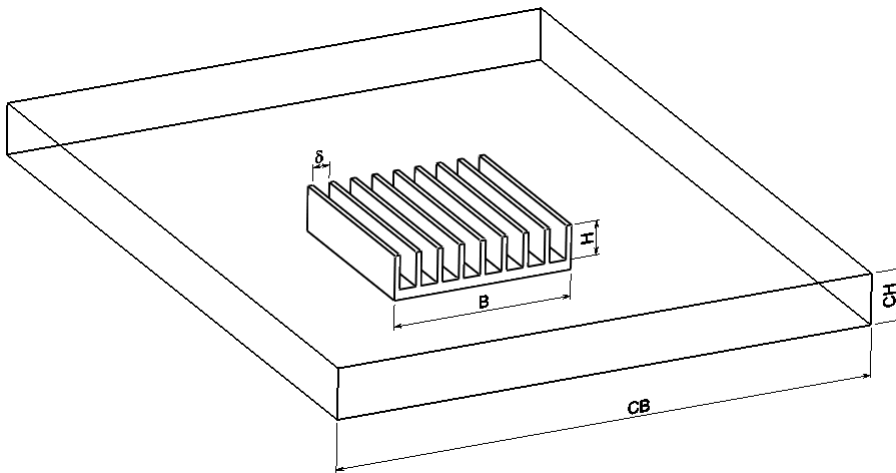


Fig. 13.1 Geometry model of the heat sink.

The model of heat sink is made of solid aluminum (thermal conductivity 200 W/(m·K)). It is heated by MINCO Thermofoil™ electrical heater with a heat load of 10 W. The bottom of the heated foil is insulated with a 25 mm Polystyrene brick (thermal conductivity 0.033 W/(m·K)). The heat sink is placed in a rectangular wind tunnel duct with the walls made of Plexiglass (thermal conductivity 0.2 W/(m·K)). It is mounted in such a way that the fin base is flush with the duct wall as shown in Fig. 13.2.

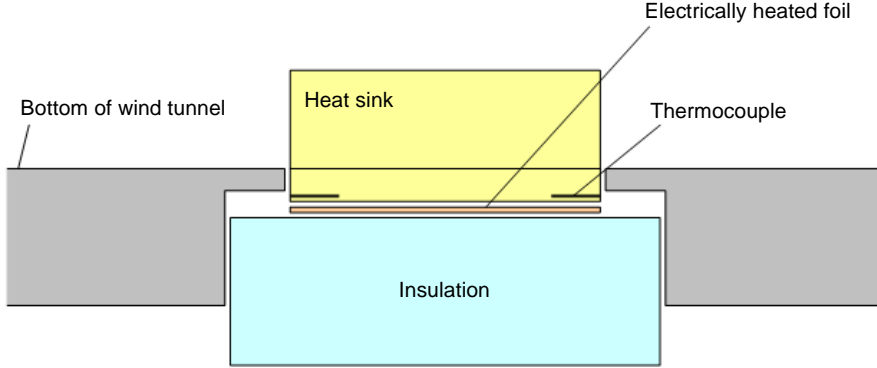


Fig. 13.2 Vertical cut view of heat sink.

The performance of the heat sink is estimated by a thermal resistance defined as

$$R_{th} = \frac{T_{hs} - T_0}{q},$$

where T_{hs} is the temperature of the heat sink base, T_0 is the temperature at the wind tunnel inlet and q is the total power input of the heat source (10 W). In Ref. 17, the T_{hs} value was measured by averaging the reading of four thermocouples (two of them can be seen in Fig. 13.2) placed symmetrically at the corners of the heat sink base.

Table 13.1 shows air inlet flow conditions specified for the calculations, inlet temperature is constant and equal 20°C. To perform the calculations, five cases are considered, each with a different inlet velocity u_{in} that was determined as follows:

$$u_{in} = \dot{V} / A,$$

where $A = 24 \text{ cm}^2$ is wind tunnel cross sectional area; \dot{V} is volumetric air flow rate at standard conditions defined as

$$w = \frac{\dot{V}}{A - A_{front}}, \quad Re_{dh} = \frac{\rho \cdot w \cdot d_h}{\mu}$$

where w is average air velocity; $A_{front} = 1.4 \text{ cm}^2$ is front area of the fins; Re_{dh} is the Reynolds duct number; d_h is hydraulic diameter of the wind tunnel; μ is dynamic viscosity of air; ρ is density of air.

Table 13.1 Inlet boundary conditions.

Case	u_{in} , m/s	Re_{dh}
1	0.903	1740
2	1.287	2480
3	1.583	3050
4	1.899	3660
5	3.633	7000

The outlet static pressure is set to 1 atm.

The heat exchange between the outer duct surfaces and the ambient medium with the temperature of 20°C is defined by a Newton's law of cooling with the heat-transfer coefficient of 3 W/m²·K.

Since the geometry model has a symmetry plane, only a half of the model is used to generate the computational mesh.

The automatically generated mesh with RRL = 3 contained approximately 26 000 cells for cases 1-4 and with RRL = 5 contained approximately 109 000 cells for case 5. Fig. 13.3 shows the mesh generated in the fluid region in one of the heat sink cross-sections. One can see that there only about 3-4 cells generated between two adjacent fins.

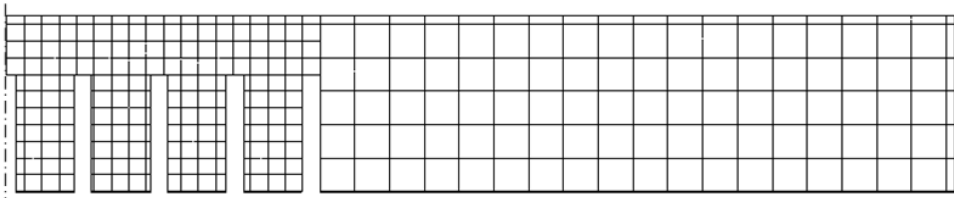


Fig. 13.3 The computational mesh (cases 1-4).

The values of thermal resistances predicted by Flow Simulation and the corresponding values measured experimentally are shown in Fig. 13.4. According to this plot, the difference between the calculations and the experimental measurements is less than 10%.

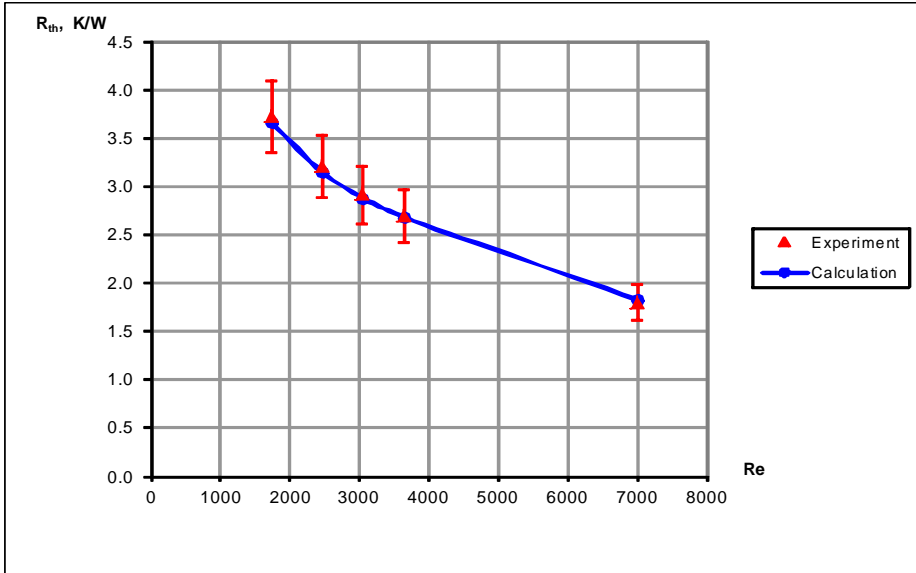


Fig. 13.4 Thermal resistance of the Heat Sink versus Reynold number in comparison with the experimental data (Ref. 17).

This indicates that the sufficient accuracy of the results is maintained even on a coarse mesh generated inside the narrow channels.

Unsteady Heat Conduction in a Solid

To validate heat conduction in solids (i.e., a conjugate heat transfer), let us consider unsteady heat conduction in a solid. To compare the Flow Simulation predictions with the analytical solution (Ref. 6), we will solve a one-dimensional problem.

A warm solid rod having the specified initial temperature and the heat-insulated side surface suddenly becomes and stays cold (at a constant temperature of $T_w = 300$ K) at both ends (see Fig. 14.1). The rod inner temperature evolution is studied. The constant initial temperature distribution along the rod is considered: $T_{\text{initial}}(x) = 350$ K.

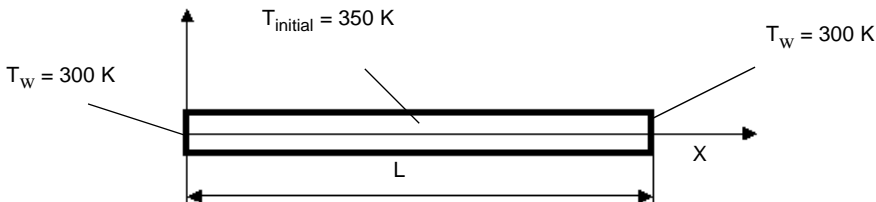


Fig. 14.1 A warm solid rod cooling down from an initial temperature to the temperature at the ends of the rod.

The problem is described by the following differential equation:

$$\frac{\partial^2 T}{\partial x^2} = \frac{\rho C}{k} \frac{\partial T}{\partial \tau},$$

where ρ , C , and k are the solid material density, specific heat, and thermal conductivity, respectively, and τ is the time, with the following boundary condition: $T = T_0$ at $x = 0$ and at $x = L$.

In the general case, i.e., at an arbitrary initial condition, the problem has the following solution:

$$T = T_0 + \sum_{n=1}^{\infty} C_n e^{-(n\pi/L)^2 k\tau/(\rho C)} \sin \frac{n\pi x}{L} ,$$

where coefficients C_n are determined from the initial conditions (see Ref. 6).

With the uniform initial temperature profile, according to the initial and boundary conditions, the problem has the following solution:

$$T = 300 + 50 \frac{4}{\pi} \sum_{n=1}^{\infty} \frac{1}{n} e^{-[n\pi/L]^2 k\tau/(\rho C)} \sin\left(\frac{n\pi x}{L}\right) \quad (\text{K}).$$

To perform the time-dependent analysis with Flow Simulation, a geometry model representing a solid parallelepiped with dimensions 1x0.2x0.1 m has been created (see Fig. 14.2).

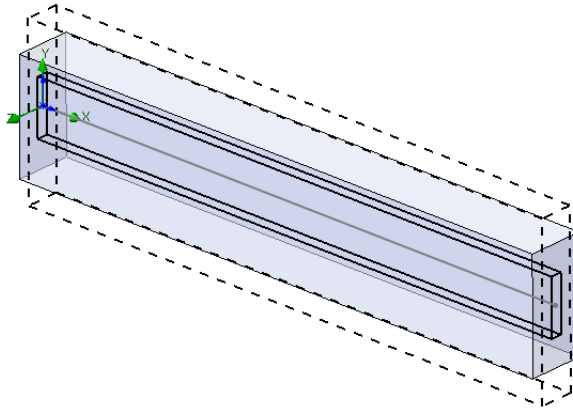


Fig. 14.2 The geometry model used for calculating heat conduction in a solid rod with Flow Simulation (the computational domain envelopes the rod).

The evolution of maximum rod temperature, predicted with Flow Simulation and compared with theory, is presented in Fig. 14.3. The Flow Simulation prediction has been performed at result resolution level 5. One can see that it coincides with the theoretical curve.

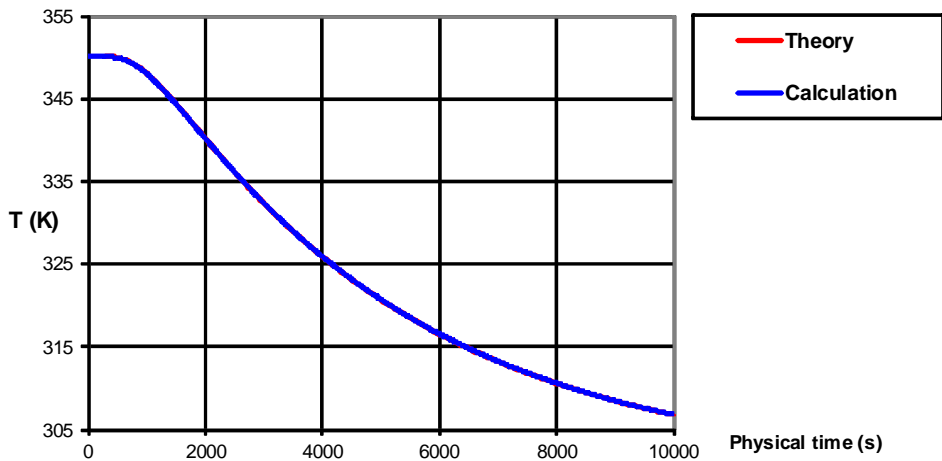


Fig. 14.3 Evolution of the maximum rod temperature, predicted with Flow Simulation and compared to theory.

The temperature profiles along the rod at different time moments, predicted by Flow Simulation, are compared to theory and presented in Fig. 14.4.

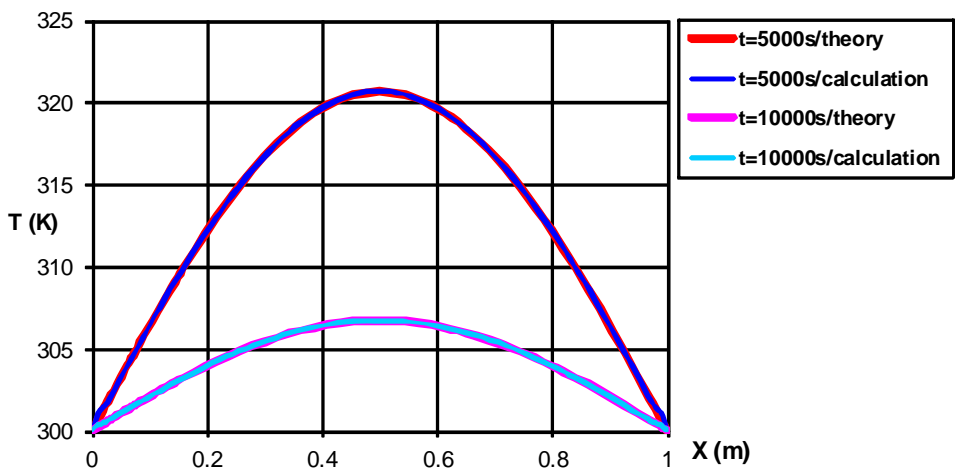


Fig. 14.4 Evolution of the temperature distribution along the rod, predicted with Flow Simulation and compared to theory.

Tube with Hot Laminar Flow and Outer Heat Transfer

Let us now consider an incompressible laminar flow of hot fluid through an externally cooled circular tube (Fig. 15.1). The fluid flow has fully developed velocity and temperature profiles at the tube inlet, whereas the heat transfer conditions specified at the tube outer surface surrounded by a cooling medium sustain the self-consistent fluid temperature profile throughout the tube.

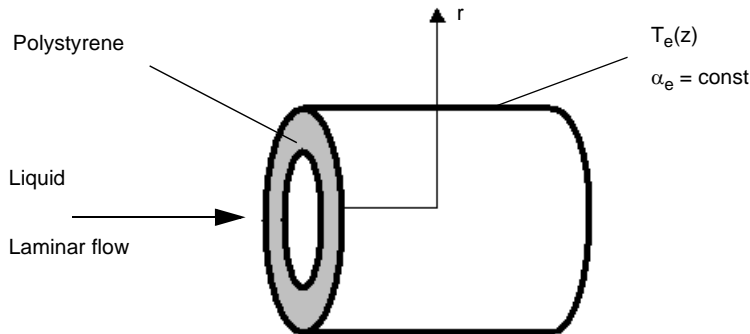


Fig. 15.1 Laminar flow in a tube cooled externally.

In accordance with Ref. 6, a laminar tube flow with a fully developed velocity profile has a self-consistent fully developed temperature profile if the following two conditions are satisfied: the fluid's properties are temperature-independent and the heat flux from the tube inner surface to the fluid (or vice versa) is constant along the tube. These conditions provide the following fully developed tube flow temperature profile:

$$T(r, z) = T(r=0, z=z_{inlet}) - \frac{q_w R_i}{k} \left[\left(\frac{r}{R_i} \right)^2 - \frac{1}{4} \left(\frac{r}{R_i} \right)^4 \right] + \frac{4q_w \cdot (z - z_{inlet})}{\rho C_p u_{max} R_i},$$

where

T is the fluid temperature,

r is a radial coordinate ($r = 0$ corresponds to the tube axis, $r = R_i$ corresponds to the tube inner surface, i.e., R_i is the tube inner radius),

z is an axial coordinate ($z = z_{inlet}$ corresponds to the tube inlet),

q_w is a constant heat flux from the fluid to the tube inner surface,

k is the fluid thermal conductivity,

ρ is the fluid density,

C_p is the fluid specific heat under constant pressure,

u_{max} is the maximum fluid velocity of the fully developed velocity profile

$$u(r) = u_{max} \left(1 - \left(\frac{r}{R_i} \right)^2 \right).$$

Since the tube under consideration has no heat sinks and is cooled by surrounding fluid medium, let us assume that the fluid medium surrounding the tube has certain fixed temperature T_e , and the heat transfer between this medium and the tube outer surface is determined by a specified constant heat transfer coefficient α_e .

By assuming a constant thermal conductivity of the tube material, k_s , specifying an arbitrary α_e , and omitting intermediate expressions, we can obtain the following expression for T_e :

$$T_e(z) = T(r = 0, z = z_{inlet}) - q_w R_i \left(\frac{3}{4k} + \frac{1}{\alpha_e R_o} - \frac{1}{k_s} \ln \frac{R_i}{R_o} \right) + \frac{4q_w \cdot (z - z_{inlet})}{\rho C_p u_{max} R_i},$$

where R_o is the tube outer radius.

In the validation example under consideration (Fig. 15.2) the following tube and fluid characteristics have been specified: $R_i = 0.05$ m, $R_o = 0.07$ m, $z - z_{inlet} = 0.1$ m, the tube material is polystyrene with thermal conductivity $k_s = 0.082$ W/(m·K), $u_{max} = 0.002$ m/s, $T(r=0, z=z_i) = 363$ K, $q_w = 147.56$ W/m², $k = 0.3$ W/(m·K), $C_p = 1000$ J/(kg·K), fluid dynamic viscosity $\mu = 0.001$ Pa·s, $\rho = 1000$ kg/m³ (these fluid properties provide a laminar flow condition since the tube flow Reynolds number based on the tube diameter is equal to $Re_d = 100$). The $T(r, z_{inlet})$ and $u(r)$ profiles at the tube inlet, the $T_e(z)$ distribution along the tube, $\alpha_e = 5$ W/(m²·K), and tube outlet static pressure $P_{out} = 1$ atm have been specified as the boundary conditions.

The inlet flow velocity and temperature profiles have been specified as the initial conditions along the tube.

To reduce the computational domain, the calculations have been performed with the $Y = 0$ and $X = 0$ flow symmetry planes. The calculations have been performed at result resolution level 7.

The fluid and solid temperature profiles predicted at $z = 0$ are shown in Fig. 15.3 together with the theoretical curve. It is seen that the prediction practically coincides with the theoretical curve (the prediction error does not exceed 0.4%).

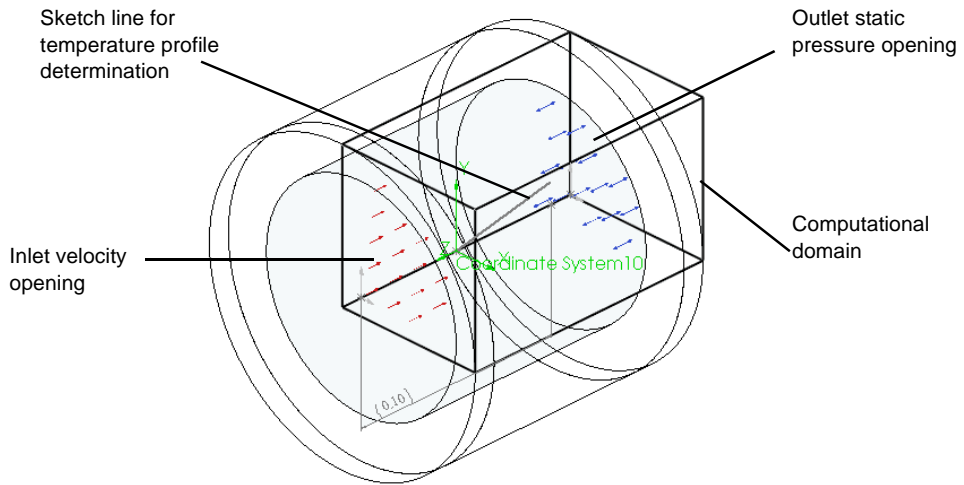


Fig. 15.2 The model used for calculating the 3D flow and the conjugate heat transfer in the tube with Flow Simulation.

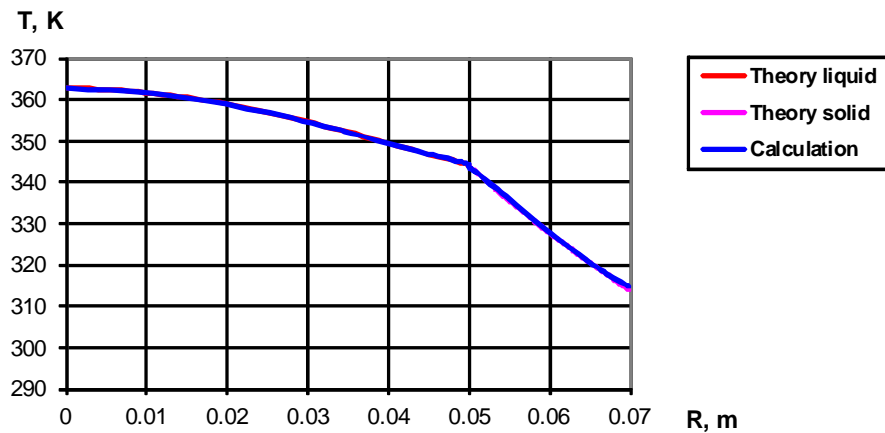


Fig. 15.3 Fluid and solid temperature profiles across the tube, predicted with Flow Simulation and compared with the theoretical curve.

Flow over a Heated Cylinder

Let us now return to the earlier validation example of incompressible flow over a cylinder and modify it by specifying a heat generation source inside the cylinder (see Fig. 16.1). The cylinder is placed in an incoming air stream and will acquire certain temperature depending on the heat source power and the air stream velocity and temperature.

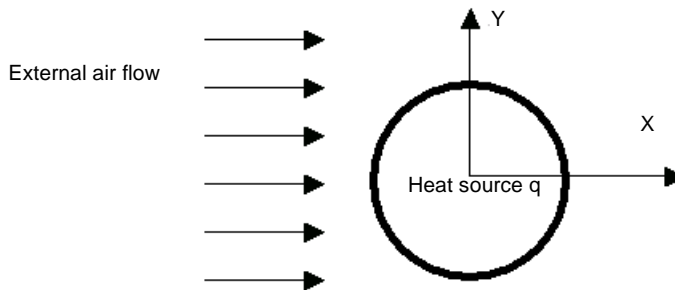


Fig. 16.1 2D flow over a

Based on experimental data for the average coefficient of heat transfer from a heated circular cylinder to air flowing over it (see Ref. 6), the corresponding Nusselt number can be determined from the following formula:

$$Nu_D = C \cdot (Re_D)^n \cdot Pr^{1/3} ,$$

where constants C and n are taken from the following table:

Re_D	C	n
0.4 - 4	0.989	0.330
4 - 40	0.911	0.385
40 - 4000	0.683	0.466
4000 - 40000	0.193	0.618
40000 - 400000	0.0266	0.805

Here, the Nusselt number, $Nu_D = (h \cdot D)/k$ (where h is the heat transfer coefficient averaged over the cylinder, and k is fluid thermal conductivity), the Reynolds number, $Re_D = (U \cdot D)/\mu$ (where U is the incoming stream velocity, and μ is fluid dynamic viscosity), and the Prandtl number, $Pr = \mu \cdot C_p/k$ (where μ is fluid dynamic viscosity, C_p is fluid specific heat at constant pressure, and k is fluid thermal conductivity) are based on the cylinder diameter D and on the fluid properties taken at the near-wall flow layer. According to Ref. 6, $Pr = 0.72$ for the entire range of Re_D .

To validate the Flow Simulation predictions, the air properties have been specified to provide $Pr = 0.72$: $k = 0.0251375 \text{ W/(m}\cdot\text{K)}$, $\mu = 1.8 \cdot 10^{-5} \text{ Pa}\cdot\text{s}$, specific heat at constant pressure $C_p = 1005.5 \text{ J/(kg}\cdot\text{K)}$. Then, the incoming stream velocity, U , has been specified to obtain $Re_D = 1, 10, 100, 10^3, 10^4, 5 \cdot 10^4, 10^5, 2 \cdot 10^5$, and $3 \cdot 10^5$ for a cylinder diameter of $D = 0.1 \text{ m}$ (see Fig. 16.1).

This validation approach consists of specifying the heat generation source inside the cylinder with a power determined from the desired steady-state cylinder temperature and the average heat transfer coefficient, $h = (Nu_D \cdot k)/D$. Nu_D is determined from the specified Re_D using the empirical formula presented above. The final cylinder surface temperature, that is also required for specifying the heat source power Q (see Table 16.1) is assumed to be 10°C higher than the incoming air temperature. The initial cylinder temperature and the incoming air temperature are equal to 293.15 K . The cylinder material is aluminum. Here, the heat conduction in the solid is calculated simultaneously with the flow calculation, i.e., the conjugate heat transfer problem is solved.

As a result of the calculation, the cylinder surface has acquired a steady-state temperature differing from the theoretical one corresponding to the heat generation source specified inside the cylinder. Multiplying the theoretical value of the Nusselt number by the ratio of the obtained temperature difference (between the incoming air temperature and the cylinder surface temperature) to the specified temperature difference, we have determined the predicted Nusselt number versus the specified Reynolds number. The values obtained by solving the steady-state and time dependent problems at result resolution level 5 are presented in Fig. 16.2 together with the experimental data taken from Ref. 6.

Table 16.1 The Flow Simulation specifications of U and Q for the problem under consideration.

Re_D	U, m/s	Q, W
1	1.5×10^{-4}	0.007
10	1.5×10^{-3}	0.016
10^2	0.015	0.041
10^3	0.15	0.121
10^4	1.5	0.405
10^5	15	1.994

From Fig. 16.2, it is seen that the predictions made with Flow Simulation, both in the time-dependent approach and in the steady-state one, are excellent within the whole Re_D range under consideration.

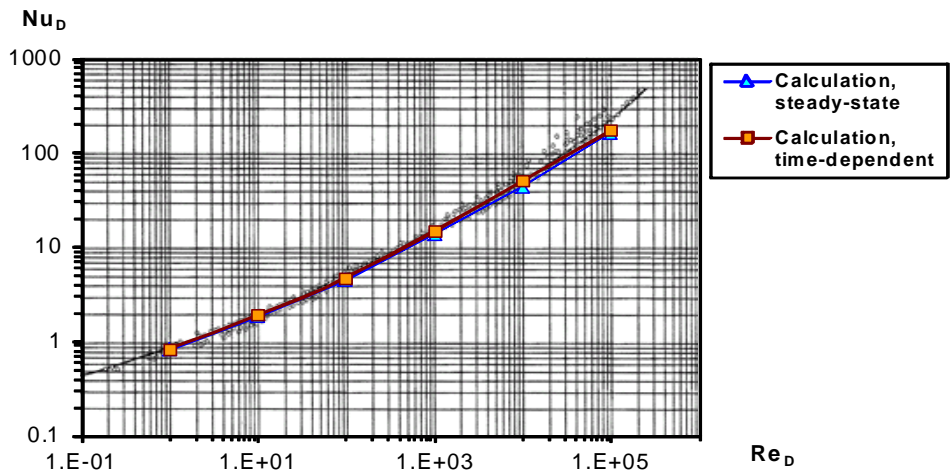


Fig. 16.2 Nusselt number for air flow over a heated cylinder: Flow Simulation predictions and the experimental data taken from Ref. 6.

Natural Convection in a Square Cavity

Here we will consider a 2D square cavity with a steady-state natural convection, for which a highly-accurate numerical solution has been proposed in Ref. 9 and used as a benchmark for about 40 computer codes in Ref. 10, besides it well agrees with the semi-empirical formula proposed in Ref. 11 for rectangular cavities. This cavity's configuration and imposed boundary conditions, as well as the used coordinate system, are presented in Fig. 17.1. Here, the left and right vertical walls are held at the constant temperatures of $T_1 = 305$ K and $T_2 = 295$ K, accordingly, whereas the upper and bottom walls are adiabatic. The cavity is filled with air.

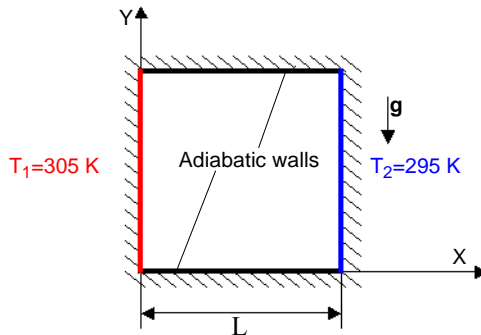


Fig. 17.1 An enclosed 2D square cavity with natural convection.

The square cavity's side dimension, L , is varied within the range of $0.0111 \dots 0.111$ m in order to vary the cavity's Rayleigh number within the range of $10^3 \dots 10^6$. Rayleigh number describes the characteristics of the natural convection inside the cavity and is defined as follows:

$$Ra = \frac{\beta g \rho^2 C_p L^3 \Delta T}{k \mu} ,$$

where $\beta = \frac{1}{T}$ is the volume expansion coefficient of air,

g is the gravitational acceleration,

C_p is the air's specific heat at constant pressure,

$\Delta T = T_1 - T_2 = 10 \text{ K}$ is the temperature difference between the walls,

k is the thermal conductivity of air,

μ is the dynamic viscosity of air.

The cavity's model is shown in Fig. 17.2.

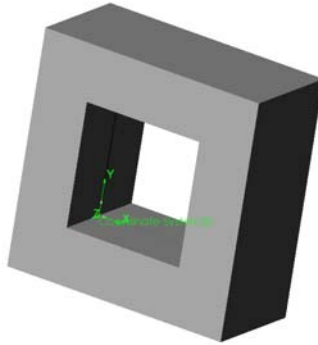


Fig. 17.2 The model created for calculating the 2D natural convection flow in the 2D square cavity using Flow Simulation.

Due to gravity and different temperatures of the cavity's vertical walls, a steady-state natural convection flow (vortex) with a vertical temperature stratification forms inside the cavity. The $Ra = 10^5$ flow's prediction performed with Flow Simulation is shown in Fig. 17.3.

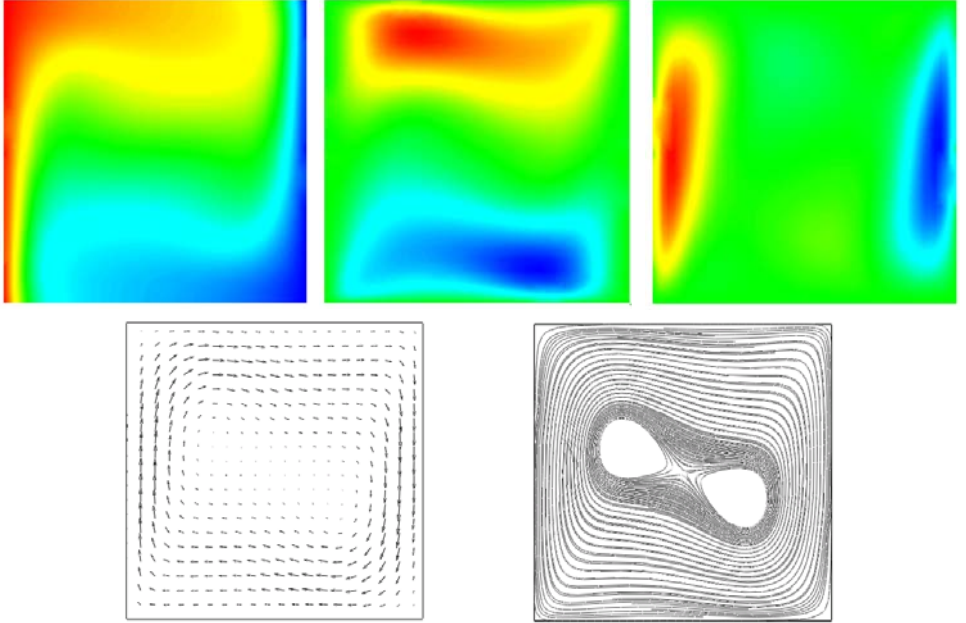


Fig. 17.3 The temperature, X-velocity, Y-velocity, the velocity vectors, and the streamlines, predicted by Flow Simulation in the square cavity at $Ra = 10^5$.

A quantitative comparison of the Flow Simulation predictions performed at result resolution level 8 with Ref. 9, Ref. 10 (computational benchmark) and Ref. 11 (semi-empirical formula) for different Ra values is presented in Figs. 17.4 - 17.6. The Nusselt number averaged over the cavity's hot vertical wall (evidently, the same value must be obtained over the cavity's cold vertical wall) $Nu_{av} = q_{wav} \cdot L / (\Delta T \cdot k)$, where q_{wav} is the heat flux from the wall to the fluid, averaged over the wall, is considered in Fig. 17.4.

Here, the dash line presents the Ref. 11 semi-empirical formula

$$Nu_{av} = 0.28 \cdot Ra^{1/4} (L/D)^{-1/4},$$

where D is the distance between the vertical walls and L is the cavity height ($D = L$ in the case under consideration). One can see that the Flow Simulation predictions practically coincide with the benchmark at $Ra \leq 10^5$ and are close to the semi-empirical data.

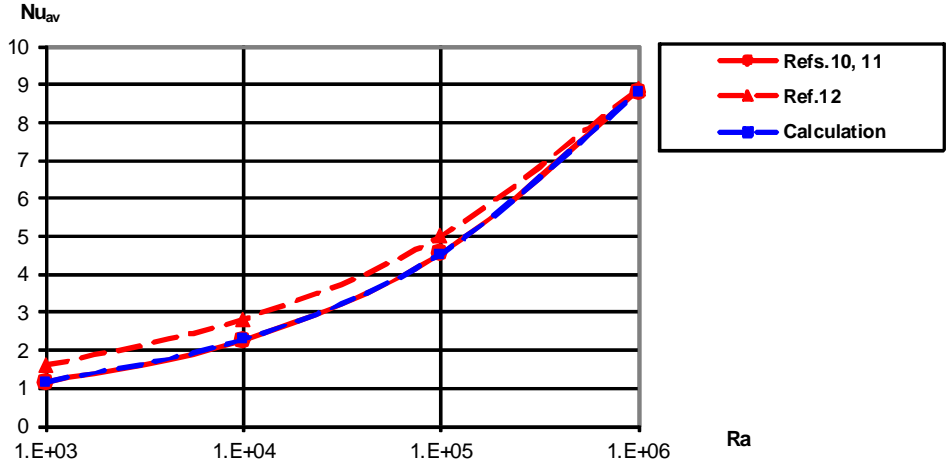


Fig. 17.4 The average sidewall Nusselt number vs. the Rayleigh number.

The dimensionless velocities of the natural convection flow in the X and Y directions,

$$\bar{U} = \frac{U \cdot L \cdot C_p \cdot \rho}{k} \quad \text{and} \quad \bar{V} = \frac{V \cdot L \cdot C_p \cdot \rho}{k} \quad (\text{which are maximum along the cavity's}$$

mid-planes, i.e., \bar{U}_{\max} along the vertical mid-plane and \bar{V}_{\max} along the horizontal

mid-plane) are considered in Fig. 17.5. The dimensionless coordinates, $\bar{x} = \frac{x}{L}$ and

$$\bar{y} = \frac{y}{L}, \quad \text{of these maximums' locations (i.e., } \bar{y} \text{ for } \bar{U}_{\max} \text{ and } \bar{x} \text{ for } \bar{V}_{\max} \text{) are}$$

presented in Fig. 17.6. One can see that the Flow Simulation predictions of the natural convection flow's local parameters are fairly close to the benchmark data at $Ra \leq 10^5$.

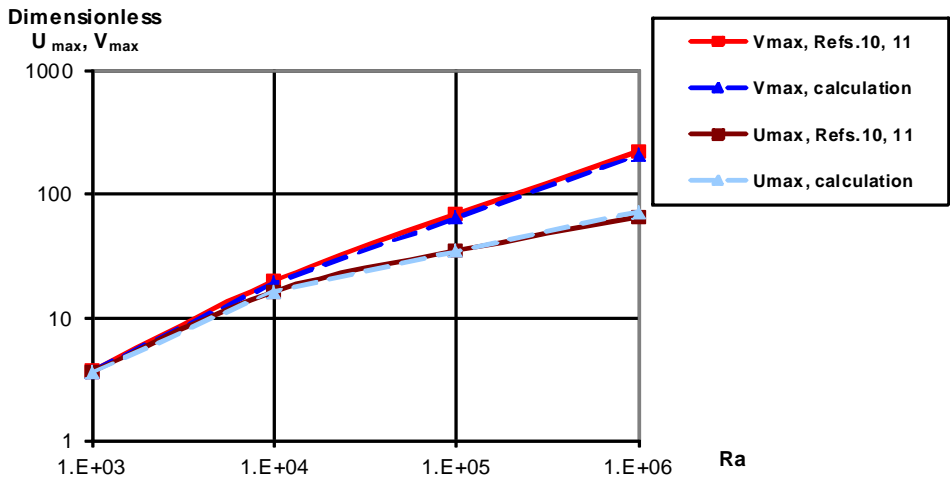


Fig. 17.5 Dimensionless maximum velocities vs. Rayleigh number.

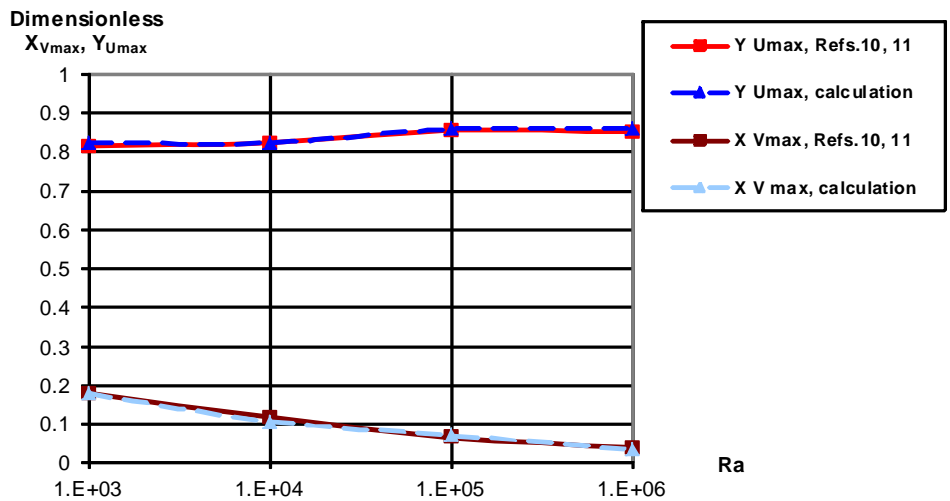


Fig. 17.6 Dimensionless coordinates of the maximum velocities' locations.

Particles Trajectories in Uniform Flows

Let us now consider the Flow Simulation capability to predict particles trajectories in a gas flow (i.e. two-phase flow of fluid + liquid droplets or solid particles).

In accordance with the particles motion model accepted in Flow Simulation, particle trajectories are calculated after completing a fluid flow calculation (which can be either steady or time-dependent). That is, the particles mass and volume flow rates are assumed substantially lower than those of the fluid stream, so that the influence of particles' motions and temperatures on the fluid flow parameters is negligible, and motion of the particles obeys the following equation:

$$m \frac{dV_p}{dt} = - \frac{\rho_f (V_f - V_p) \cdot |V_f - V_p|}{2} C_d A + F_g \quad ,$$

where m is the particle mass, t is time, V_p and V_f are the particle and fluid velocities (vectors), accordingly, ρ_f is the fluid density, C_d is the particle drag coefficient, A is the particle frontal surface area, and F_g is the gravitational force.

Particles are treated as non-rotating spheres of constant mass and specified (solid or liquid) material, whose drag coefficient is determined from Henderson's semi-empirical formula (Ref. 18). At very low velocity of particles with respect to carrier fluid (i.e., at the relative velocity's Mach number $M \rightarrow 0$) this formula becomes

$$C_d = \frac{24}{Re} + \frac{4.12}{1 + 0.03 \cdot Re + 0.48 \sqrt{Re}} + 0.38$$

where Reynolds number is defined as

$$Re = \frac{\rho_f |V_f - V_p| d}{\mu} \quad ,$$

d is the diameter of particles, and μ is the fluid dynamic viscosity.

To validate Flow Simulation, let us consider three cases of injecting a particle perpendicularly into an incoming uniform flow, Fig. 18.1. Since both the fluid flow and the particle motion in these cases are 2D (planar), we will solve a 2D (i.e. in the XY-plane) flow problem.

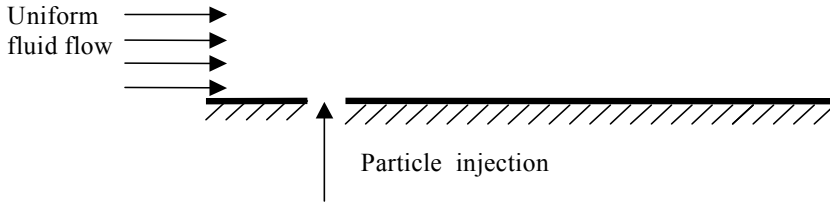


Fig. 18.1 Injection of a particle into a uniform fluid flow.

Due to the same reason as in the previous validation examples with flow over flat plates, we will solve this validation as an internal problem. The corresponding SOLIDWORKS model is shown in Fig. 18.2. Both of the walls are ideal, the channel has length of 0.233 m and height of 0.12 m, all the walls have thickness of 0.01 m. We specify the uniform fluid velocity V_{inlet} , the fluid temperature of 293.2 K, and the default values of turbulent flow parameters with the laminar boundary layer at the channel inlet, and the static pressure of 1 atm at the channel outlet. All the fluid flow calculations are performed at a result resolution level of 5.

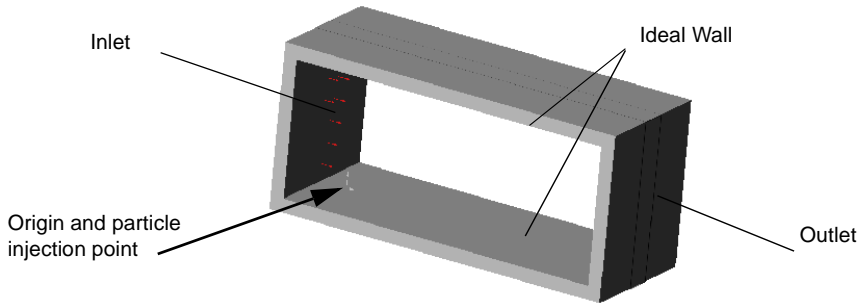


Fig. 18.2 The model geometry.

To validate calculations of particles trajectories by comparing them with available analytical solutions of the particle motion equation, we consider the following three cases:

- a) the low maximum Reynolds number of $Re_{max} = 0.1$ (air flow with $V_{inlet} = 0.002$ m/s, gold particles of $d = 0.5$ mm, injected at the velocity of 0.002 m/s perpendicularly to the wall),
- b) the high maximum Reynolds number of $Re_{max} = 105$ (water flow with $V_{inlet} = 10$ m/s, iron particles of $d = 1$ cm, injected at the velocities of 1, 2, 3 m/s perpendicularly to the wall),
- c) a particle trajectory in the Y-directed gravitational field (gravitational acceleration $g_y = -9.8$ m/s², air flow with $V_{inlet} = 0.6$ m/s, an iron particle

of $d = 1 \text{ cm}$, injected at the 1.34 m/s velocity at the angle of 63.44° with the wall).

In the first case, due to small Re values, the particle drag coefficient is close to $C_d = 24/Re$ (i.e., obeys the Stokes law). Then, neglecting gravity, we obtain the following analytical solution for the particle trajectory:

$$X(t) = X|_{t=0} + V_{fx} \cdot t + \frac{d^2 \rho_p}{18\mu} (V_{px}|_{t=0} - V_{fx}) \cdot \exp\left(-\frac{18\mu}{d^2 \rho_p} t\right) ,$$

$$Y(t) = Y|_{t=0} + V_{fy} \cdot t + \frac{d^2 \rho_p}{18\mu} (V_{py}|_{t=0} - V_{fy}) \cdot \exp\left(-\frac{18\mu}{d^2 \rho_p} t\right) ,$$

where V_{fx} , V_{px} , V_{fy} , V_{py} are the X- and Y-components of the fluid and particle velocities, accordingly, ρ_p is the particle material density. The Flow Simulation calculation and the analytical solution are shown in Fig. 18.3. It is seen that they are very close to one another. Special calculations have shown that the difference is due to the C_D assumptions only.

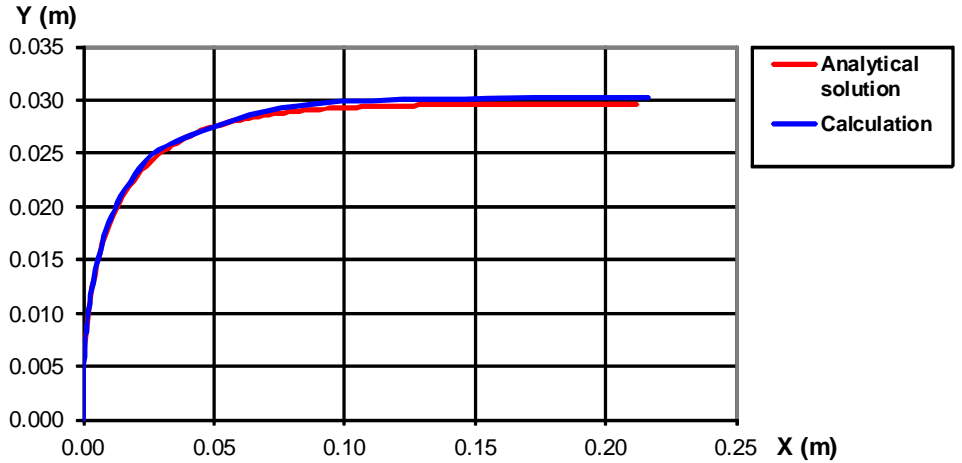


Fig. 18.3 Particle trajectories in a uniform fluid flow at $Re_{\max} = 0.1$, predicted by Flow Simulation and obtained from the analytical solution.

In the second case, due to high Re values, the particle drag coefficient is close to $C_d = 0.38$. Then, neglecting the gravity, we obtain the following analytical solution for the particle trajectory:

$$Y(t) = Y|_{t=0} + V_{fy} \cdot t + \frac{\rho_p d}{0.285 \rho} (V_{py}|_{t=0} - V_{fy}) \cdot \ln\left(1 + \frac{0.285 \rho}{\rho_p d} t\right) ,$$

$$X(t) = X|_{t=0} + V_{fx} \cdot t + \frac{\rho_p d}{0.285 \rho} (V_{px}|_{t=0} - V_{fx}) \cdot \ln\left(1 + \frac{0.285 \rho}{\rho_p d} t\right) .$$

The Flow Simulation calculations and the analytical solutions for three particle injection velocities, $V_{py}(t=0) = 1, 2, 3 \text{ m/s}$, are shown in Fig. 18.4. It is seen that the Flow Simulation calculations coincide with the analytical solutions. Special calculations have shown that the difference is due to the C_D assumptions only.

In the third case, the particle trajectory is governed by the action of the gravitational force only, the particle drag coefficient is very close to zero, so the analytical solution is:

$$Y = Y|_{t=0} + V_{py}|_{t=0} t + g_y \cdot \frac{1}{2} \left(\frac{X - X|_{t=0}}{V_{px}} \right)^2 .$$

The Flow Simulation calculation and the analytical solution for this case are presented in Fig. 18.5. It is seen that the Flow Simulation calculation coincides with the analytical solution.

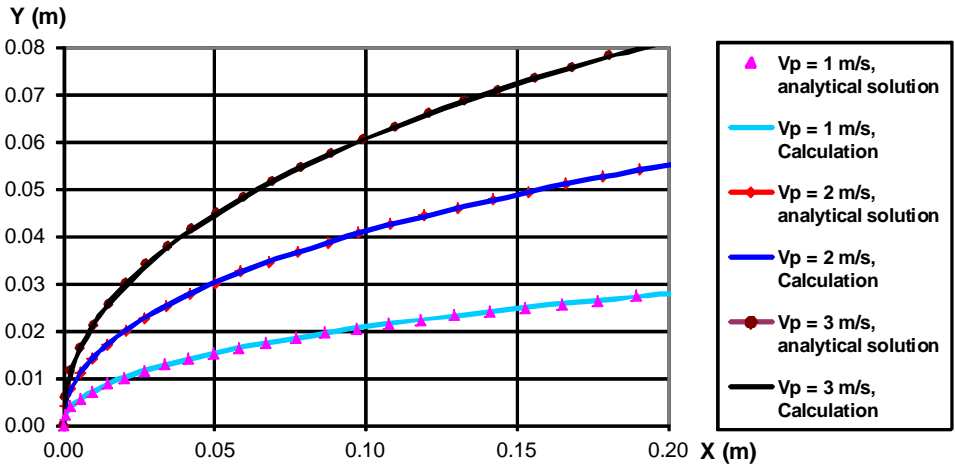


Fig. 18.4 Particle trajectories in a uniform fluid flow at $Re_{\max} = 10^5$, predicted by Flow Simulation and obtained from the analytical solution.

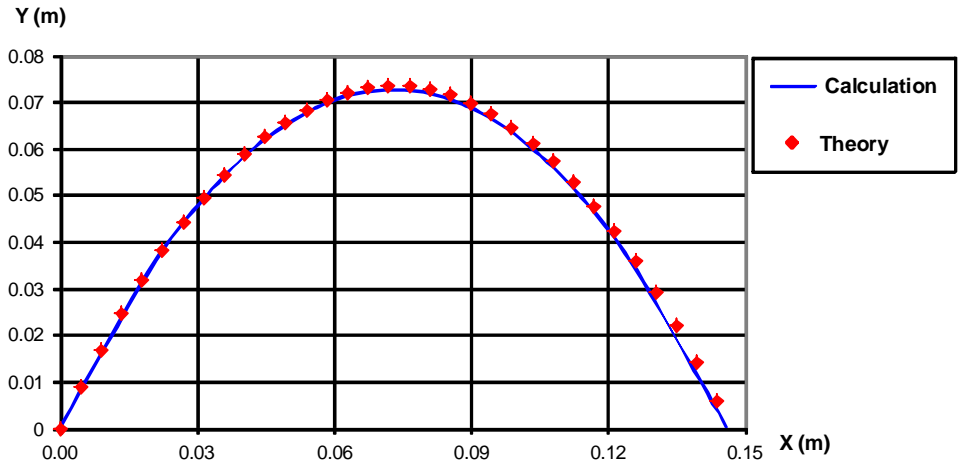


Fig. 18.5 Particle trajectories in the Y-directed gravity, predicted by Flow Simulation and obtained from the analytical solution.

Porous Screen in a Non-uniform Stream

Let us now validate the Flow Simulation capability to calculate fluid flows through porous media.

Here, following Ref. 2, we consider a plane cold air flow between two parallel plates, through a porous screen installed between them, see Fig. 19.1. At the channel inlet the air stream velocity profile is step-shaped (specified). The porous screen (gauze) levels this profile to a more uniform profile. This effect depends on the screen drag, see Ref. 2.

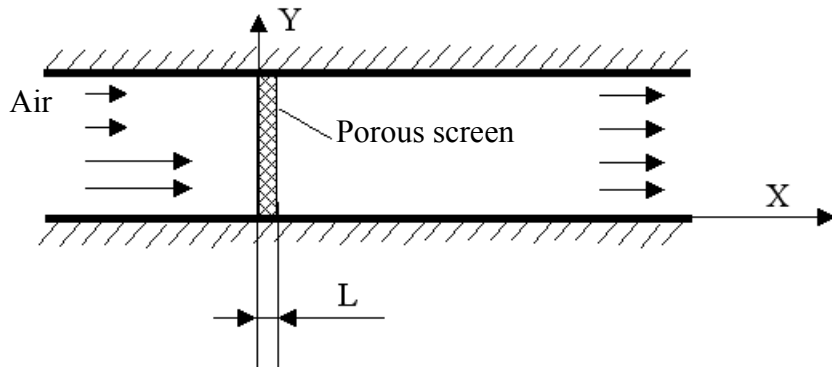


Fig. 19.1 Leveling effect of a porous screen (gauze) on a non-uniform stream.

The SOLIDWORKS model used for calculating the 2D (in XY-plane) flow is shown in Fig. 19.2. The channel has height of 0.15 m, the inlet (upstream of the porous screen) part of the 0.3 m length, the porous screen of the 0.01 m thickness, and the outlet (downstream of the porous screen) part of the 0.35 m length. All the walls have thickness of 0.01 m.

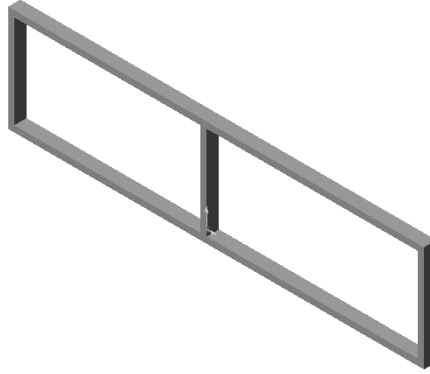


Fig. 19.2 The SOLIDWORKS model used for calculating the 2D flow between two parallel plates and through the porous screen with Flow Simulation.

Following Ref. 2, we consider porous screens (gauzes) of different drag, ζ :

$\zeta = 0.95, 1.2, 2.8$, and 4.1 , defined as:

$$\zeta = \frac{2\Delta P}{\rho V^2} ,$$

where ΔP is the pressure difference between the screen sides, $\rho V^2/2$ is the dynamic pressure (head) of the incoming stream.

Since in Flow Simulation a porous medium's resistance to flow is characterized by parameter $k = -gradP/\rho V$, then for the porous screens $k = V \cdot \zeta / (2L)$, where V is the fluid velocity, L is the porous screen thickness. In Flow Simulation, this form of a porous medium's resistance to flow is specified as $k = (A \cdot V + B) / \rho$, so $A = \rho \zeta / (2L)$, $B = 0$ for the porous screens under consideration. Therefore, taking $L = 0.01$ m and $\rho = 1.2$ kg/m³ into account, we specify $A = 57, 72, 168$, and 246 kg/m⁻⁴ for the porous screens under consideration. In accordance with the screens' nature, their permeability is specified as isotropic.

According to the experiments presented in Ref. 2, the step-shaped velocity profiles $V(Y)$ presented in Fig. 19.3 have been specified at the model inlet. The static pressure of 1 atm has been specified at the model outlet.

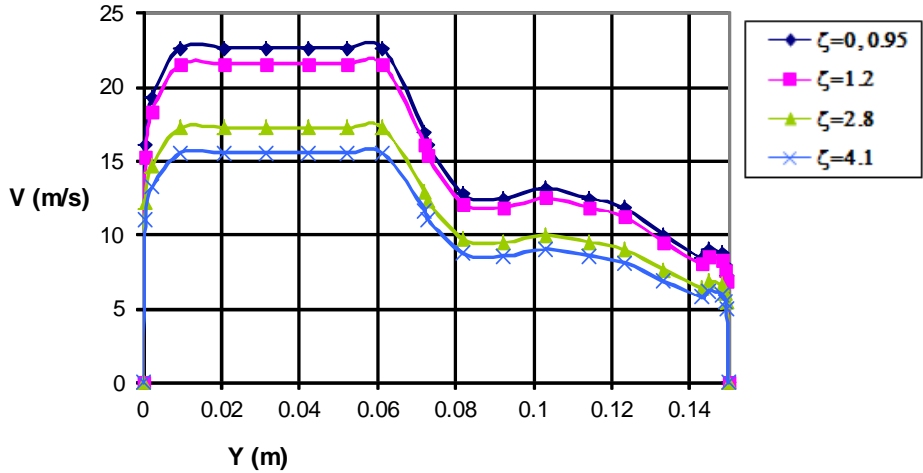


Fig. 19.3 Inlet velocity profiles.

The air flow dynamic pressure profiles at the 0.3 m distance downstream from the porous screens, both predicted by Flow Simulation at result resolution level 5 and measured in the Ref. 2 experiments, are presented in Fig. 19.4 for the $\zeta = 0$ case (i.e., without screen) and Figs. 19.5-19.8 for the porous screens of different ζ .

It is seen that the Flow Simulation predictions agree well, both qualitatively and quantitatively, with the experimental data both in absence of a screen and for all the porous screens (gauzes) under consideration, demonstrating the leveling effect of the gauze screens on the step-shaped incoming streams. The prediction error in the dynamic pressure maximum does not exceed 30%.

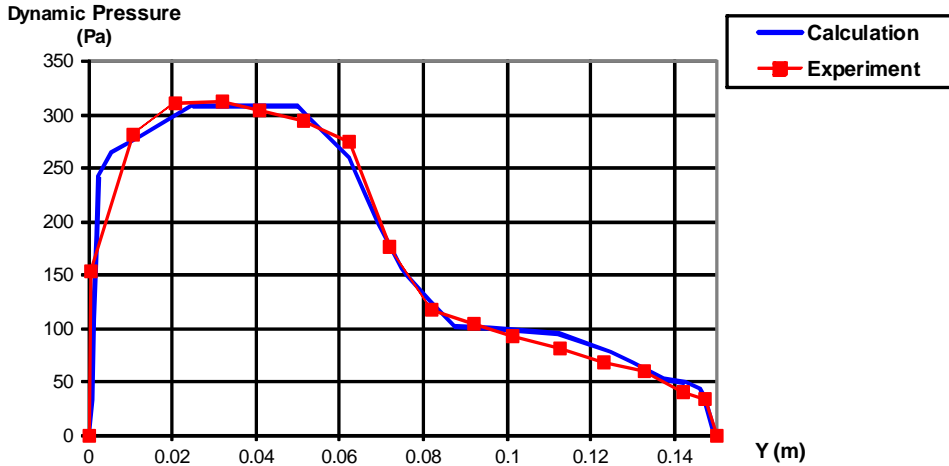


Fig. 19.4 The dynamic pressure profiles at $\zeta = 0$, predicted by Flow Simulation and compared to the Ref. 2 experiments.

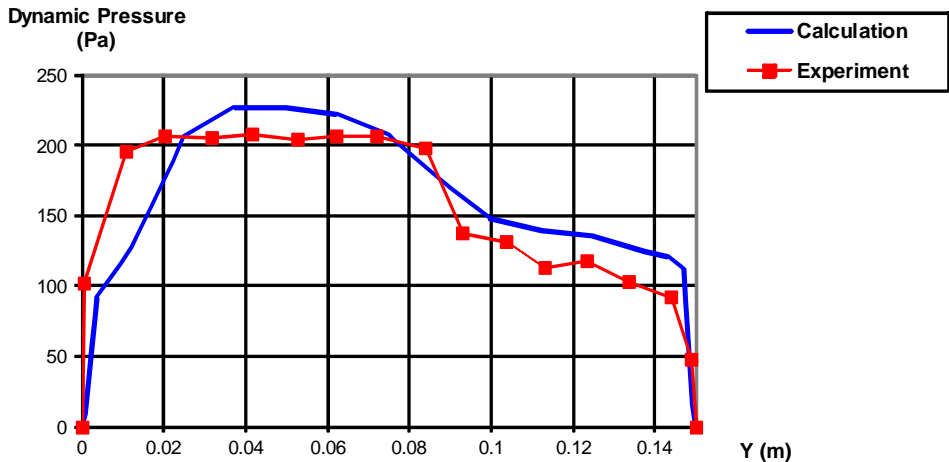


Fig. 19.5 The dynamic pressure profiles at $\zeta = 0.95$, predicted by Flow Simulation and compared to the Ref. 2 experiments.

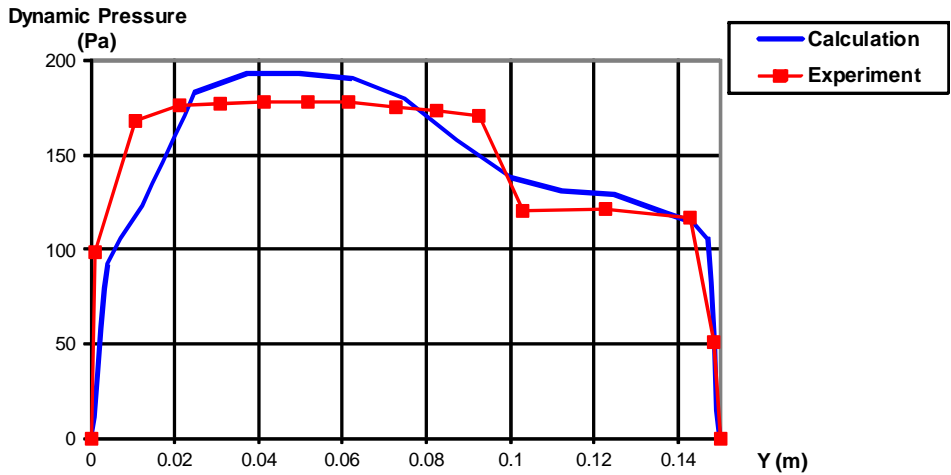


Fig. 19.6 The dynamic pressure profiles at $\zeta = 1.2$, predicted by Flow Simulation and compared to the Ref. 2 experiments.

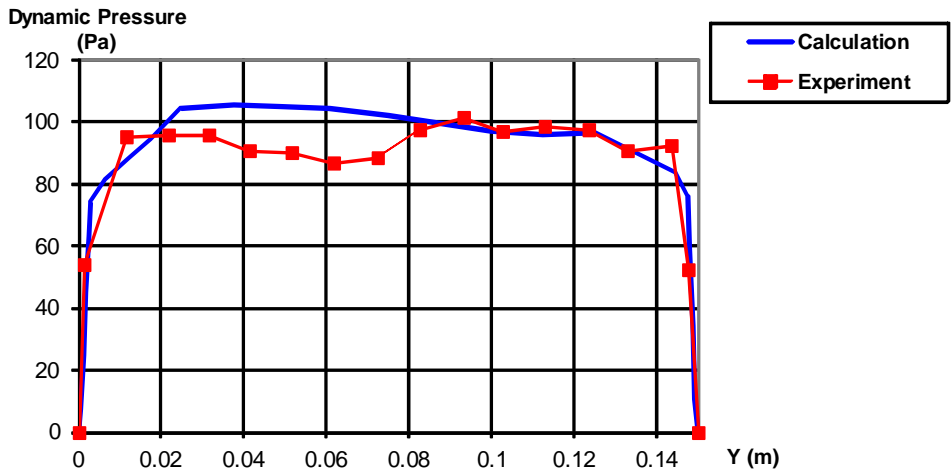


Fig. 19.7 The dynamic pressure profiles at $\zeta = 2.8$, predicted by Flow Simulation and compared to the Ref. 2 experiments.

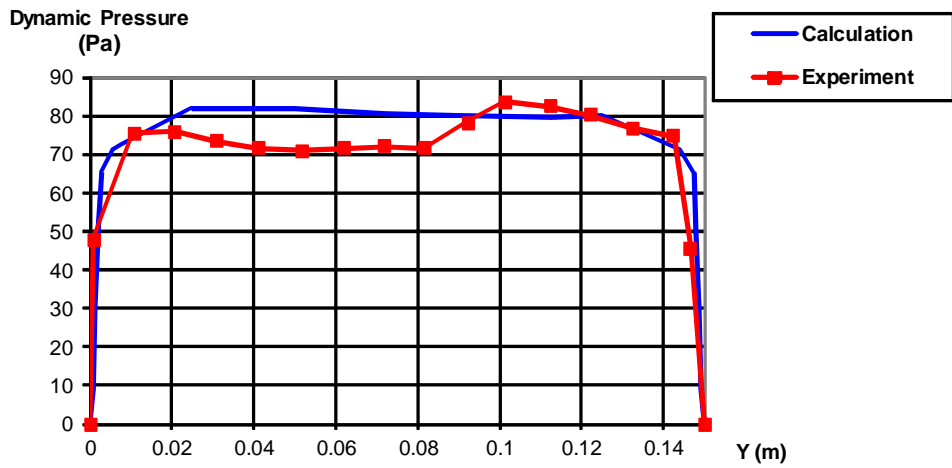


Fig. 19.8 The dynamic pressure profiles at $\zeta = 4.1$, predicted by Flow Simulation and compared to the Ref. 2 experiments.

Lid-driven Flows in Triangular and Trapezoidal Cavities

Let us now see how Flow Simulation predicts lid-driven (i.e., shear-driven) 2D recirculating flows in closed 2D triangular and trapezoidal cavities with one or two moving walls (lids) in comparison with the calculations performed in Ref. 19 and Ref. 20.

These two cavities are shown in Fig. 20.1. The triangular cavity has a moving top wall, the trapezoidal cavity has a moving top wall also, whereas its bottom wall is considered in two versions: as motionless and as moving at the top wall velocity. The no-slip conditions are specified on all the walls.

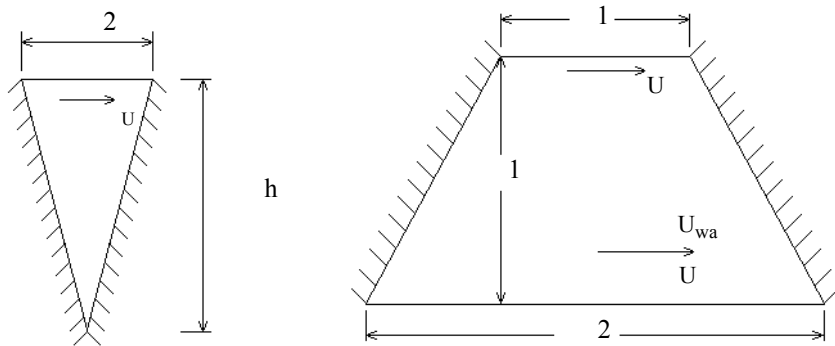


Fig. 20.1 The 2D triangular (left) and trapezoidal (right) cavities with the moving walls (the motionless walls are shown with dashes).

As shown in Ref. 19 and Ref. 20, the shear-driven recirculating flows in these cavities are fully governed by their Reynolds numbers $Re = \rho \cdot U_{wall} \cdot h / \mu$, where ρ is the fluid density, μ is the fluid dynamic viscosity, U_{wall} is the moving wall velocity, h is the cavity height. So, we can specify the height of the triangular cavity $h = 4$ m, the height of the trapezoidal cavity $h = 1$ m, $U_{wall} = 1$ m/s for all cases under consideration, the fluid density $\rho = 1$ kg/m³, the fluid dynamic viscosity $\mu = 0.005$ Pa·s in the triangular cavity produces a $Re = 800$, and $\mu = 0.01, 0.0025, 0.001$ Pa·s in the trapezoidal cavity produces a $Re = 100, 400, 1000$, respectively.

The cavities' models are shown in Fig. 20.2. The Flow Simulation calculation of flow in the triangular cavity has been performed on the 48x96 computational mesh. The results in comparison with those from Ref. 19 are presented in Fig. 20.3 (streamlines) and in Fig. 20.4 (the fluid velocity X-component along the central vertical bisector shown by a green line in Fig. 20.2). A good agreement of these calculations is clearly seen.

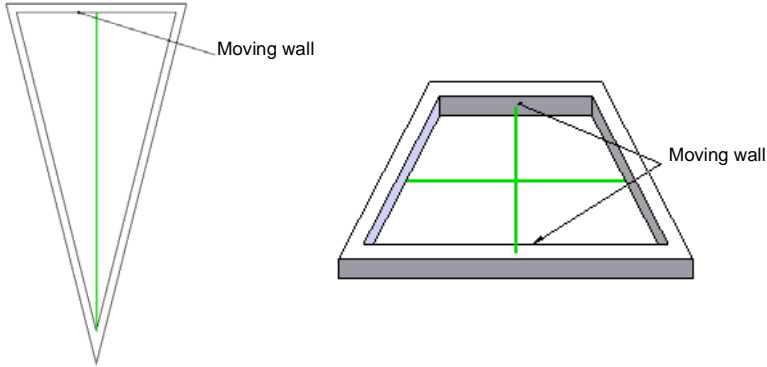


Fig. 20.2 The models for calculating the lid-driven 2D flows in the triangular (left) and trapezoidal (right) cavities with Flow Simulation.

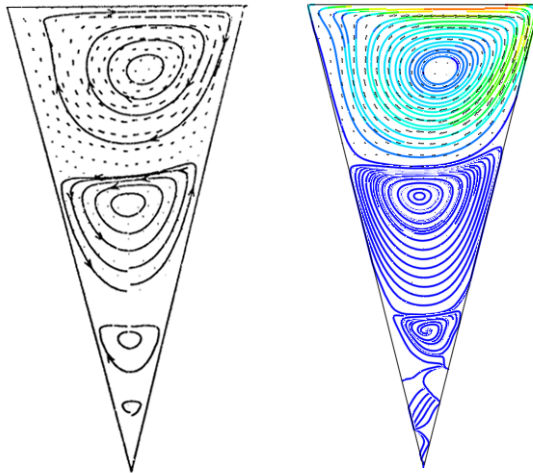


Fig. 20.3 The flow trajectories in the triangular cavity, calculated by Flow Simulation (right) and compared to the Ref. 19 calculation (left).

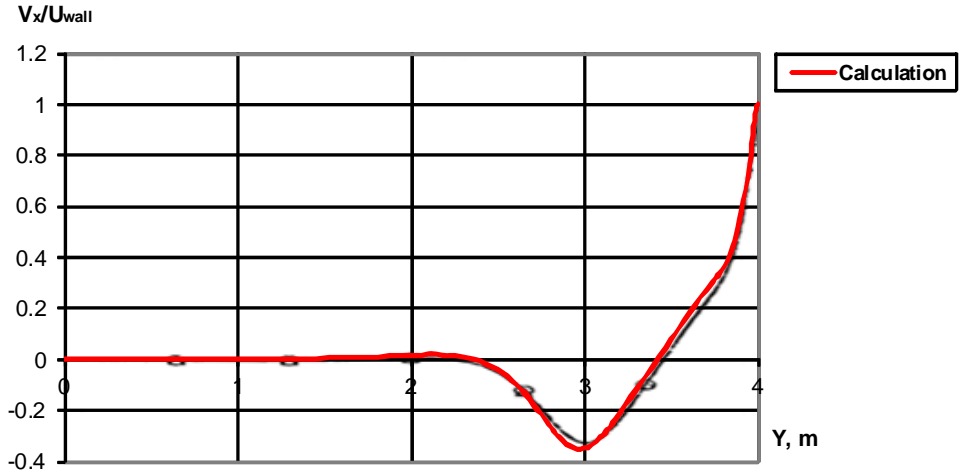


Fig. 20.4 The triangular cavity's flow velocity X-component along the central vertical bisector, calculated by Flow Simulation (red line) and compared to the Ref. 19 calculation (black line with circlets).

The Flow Simulation calculations of flows in the trapezoidal cavity with one and two moving walls at different Re values have been performed with the 100×50 computational mesh. Their results in comparison with those from Ref. 20 are presented in Figs. 20.5-20.10 (streamlines) and in Fig. 20.11 (the fluid velocity X-component along the central vertical bisector shown by a green line in Fig. 20.2). A good agreement of these calculations is seen.

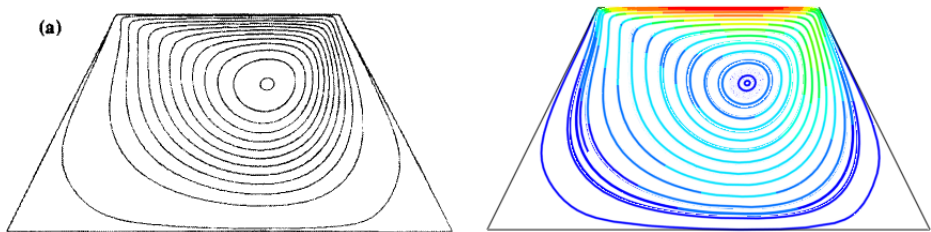


Fig. 20.5 The flow streamlines in the trapezoidal cavity with a top only moving wall at $Re = 100$, calculated by Flow Simulation (right) and compared to the Ref. 20 calculation (left).

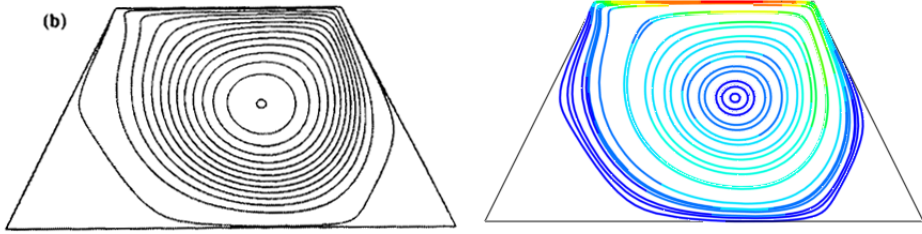


Fig. 20.6 The flow streamlines in the trapezoidal cavity with a top only moving wall at $Re = 400$, calculated by Flow Simulation (right) and compared to the Ref. 20 calculation (left).

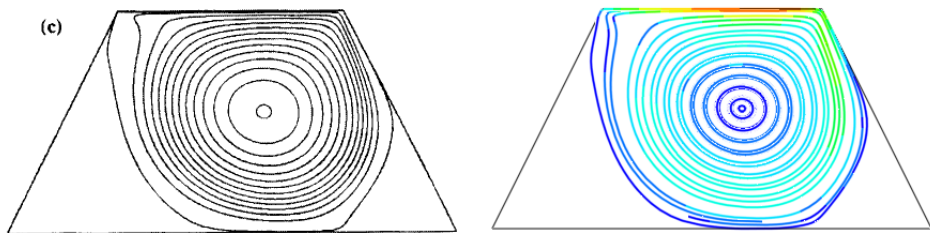


Fig. 20.7 The flow streamlines in the trapezoidal cavity with a top only moving wall at $Re = 1000$, calculated by Flow Simulation (right) and compared to the Ref. 20 calculation (left).

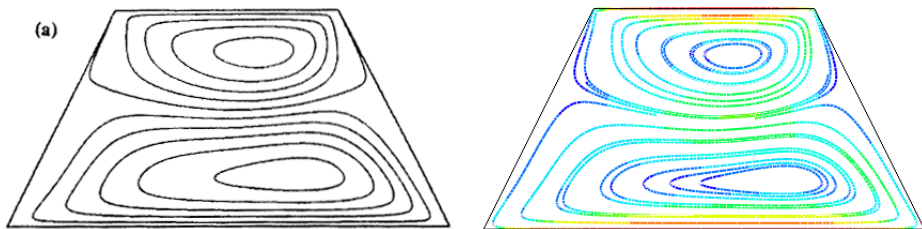


Fig. 20.8 The flow streamlines in the trapezoidal cavity with two moving walls at $Re = 100$, calculated by Flow Simulation (right) and compared to the Ref. 20 calculation (left).

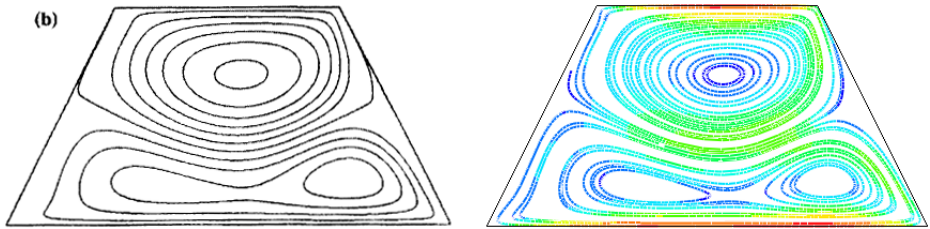


Fig. 20.9 The flow streamlines in the trapezoidal cavity with two moving walls at $Re = 400$, calculated by Flow Simulation (right) and compared to the Ref. 20 calculation (left).

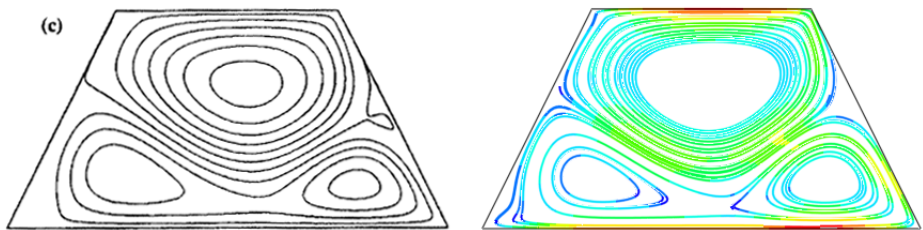


Fig. 20.10 The flow streamlines in the trapezoidal cavity with two moving walls at $Re = 1000$, calculated by Flow Simulation (right) and compared to the Ref. 20 calculation (left).

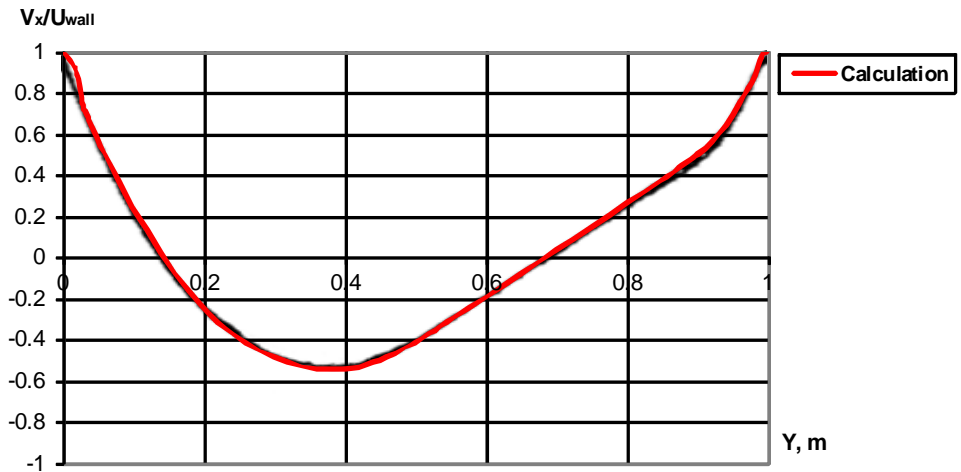


Fig. 20.11 The flow velocity X-component along the central vertical bisector in the trapezoidal cavity with two moving walls at $Re = 400$, calculated by Flow Simulation (red line) and compared to the Ref. 20 calculation (black line).

Flow in a Cylindrical Vessel with a Rotating Cover

Let us now see how Flow Simulation predicts a 3D recirculating flow in a cylindrical vessel closed by a rotating cover (see Fig. 21.1) in comparison with the experimental data presented in Ref. 21 (also in Ref. 22). This vessel of $R = h = 0.144$ m dimensions is filled with a glycerol/water mixture. The upper cover rotates at the angular velocity of Ω . The other walls of this cavity are motionless. The default no-slip boundary condition is specified for all walls.

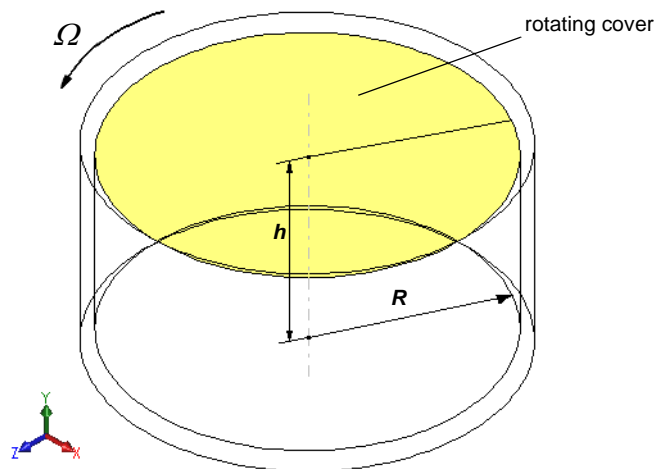


Fig. 21.1 The cylindrical vessel with the a rotating cover.

Due to the cover rotation, a shear-driven recirculating flow forms in this vessel. Such flows are governed by the Reynolds number $Re = \rho \cdot \Omega \cdot R^2 / \mu$, where ρ is the fluid density, μ is the fluid dynamic viscosity, Ω is the angular velocity of the rotating cover, R is the radius of the rotating cover. In the case under consideration the 70/30% glycerol/water mixture has $\rho = 1180 \text{ kg/m}^3$, $\mu = 0.02208 \text{ Pa}\cdot\text{s}$, the cover rotates at $\Omega = 15.51 \text{ rpm}$, so $Re = 1800$.

The Flow Simulation calculation has been performed on the 82x41x82 computational mesh. The formed flow pattern (toroidal vortex) obtained in this calculation is shown in Fig. 21.2 using the flow velocity vectors projected onto the XY-plane. The tangential and radial components of the calculated flow velocity along four vertical lines arranged in the XY-plane at different distances from the vessel axis in comparison with the Ref. 21 experimental data are presented in Figs. 21.3-21.6 in the dimensionless form (the Y-coordinate is divided by R , the velocity components are divided by $\Omega \cdot R$). There is good agreement with the calculation results and the experimental data shown.

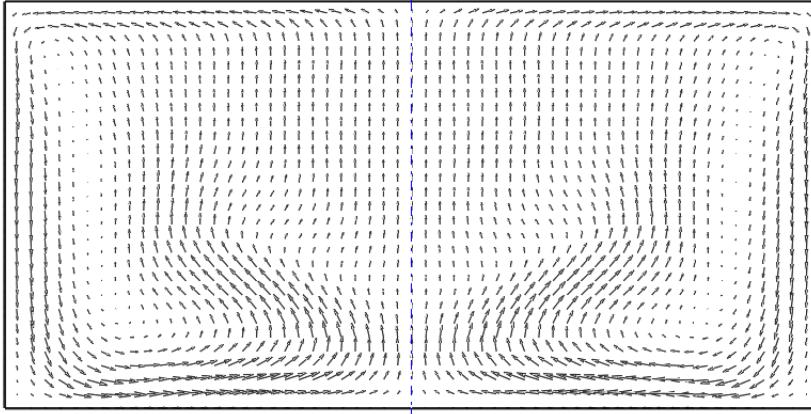


Fig. 21.2 The vessel's flow velocity vectors projected on the XY-plane.

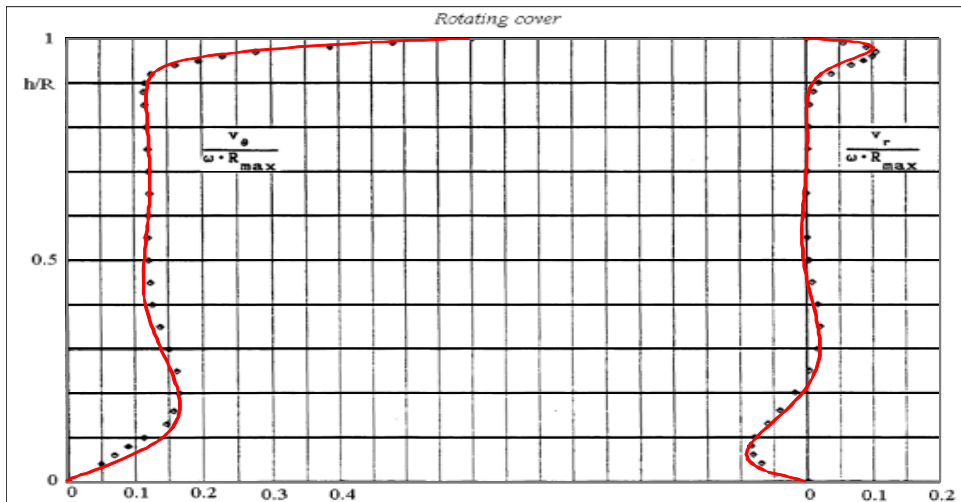


Fig. 21.3 The vessel's flow tangential and radial velocity components along the $X = 0.6$ vertical, calculated by Flow Simulation (red) and compared to the Ref. 21 experimental data.

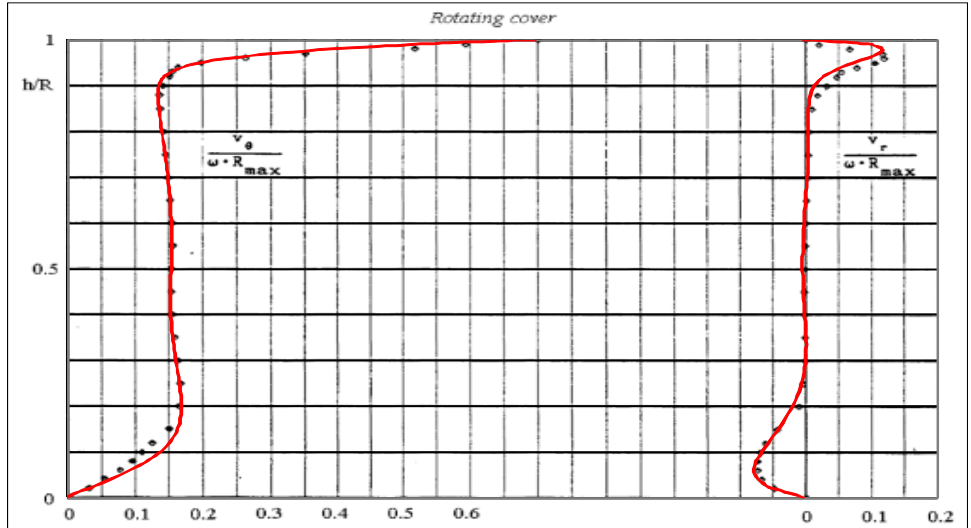


Fig. 21.4 The vessel's flow tangential and radial velocity components along the $X = 0.7$ vertical, calculated by Flow Simulation (red) and compared to the Ref. 21 experimental data.

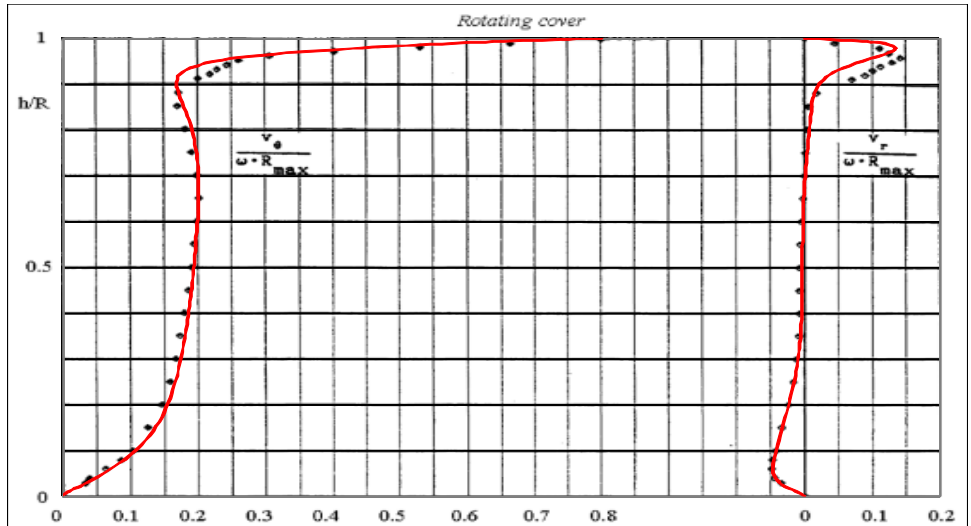


Fig. 21.5 The vessel's flow tangential and radial velocity components along the $X = 0.8$ vertical, calculated by Flow Simulation (red) and compared to the Ref. 21 experimental data.

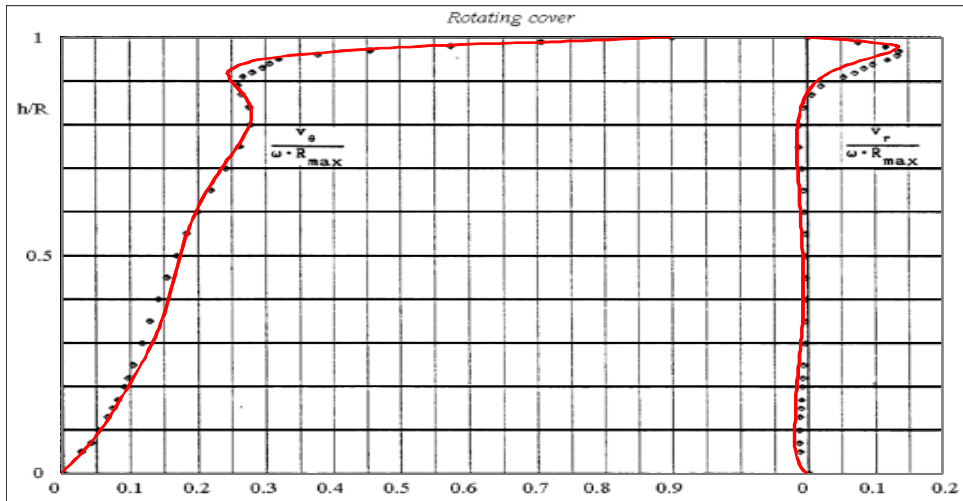


Fig. 21.6 The vessel's flow tangential and radial velocity components along the $X = 0.9$ vertical, calculated by Flow Simulation (red) and compared to the Ref. 21 experimental data.

Flow in an Impeller

Let us now validate the Flow Simulation ability to perform calculations in a rotating coordinate system related to a rotating solid. Following Ref. 23, we will consider the flow of water in a 9-bladed centrifugal impeller having blades tilted at a constant 60° angle with respect to the intersecting radii and extending out from the 320 mm inner diameter to the 800 mm outer diameter (see Fig. 22.1). The water in this impeller flows from its center to its periphery. To compare the calculation with the experimental data presented in Ref. 23, the impeller's angular velocity of 32 rpm and volume flow rate of $0.00926 \text{ m}^3/\text{s}$ are specified.

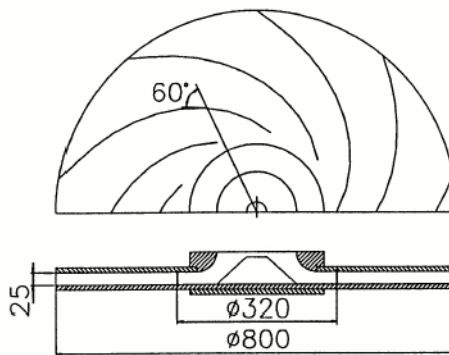


Fig. 22.1 The impeller's blades geometry.

Since the impeller's inlet geometry and disk extension serving as the impeller's vaneless diffuser have no exact descriptions in Ref. 23, to perform the validating calculation we arbitrarily specified the annular inlet as 80 mm in diameter with an uniform inlet velocity profile perpendicular to the surface in the stationary coordinate system. The impeller's disks external end was specified as 1.2 m diameter, as shown in Fig. 22.2.

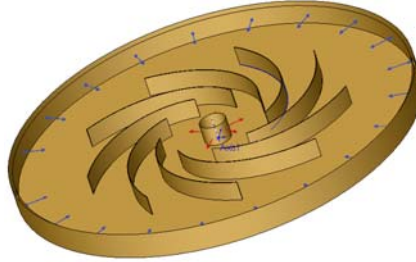


Fig. 22.2 The model used for calculating the 3D flow in the impeller.

The above-mentioned volume flow rate at the annular inlet and the potential pressure of 1 atm at the annular outlet are specified as the problem's flow boundary conditions.

The Flow Simulation 3D flow calculation is performed on the computational mesh using the result resolution level of 5 and the minimum wall thickness of 2 mm (since the blades have constant thickness). To further capture the curvature of the blades a local initial mesh was also used in the area from the annular inlet to the blades' periphery. As a result, the computational mesh has a total number of about 1,000,000 cells.

Following Ref. 23, let us compare the passage-wise flow velocities (w_s , see their definition in Fig. 22.3, $\beta = 60^\circ$) along several radial lines passing through the channels between the blades (lines g, j, m, p in Fig. 22.4) at the mid-height between the impeller's disks.

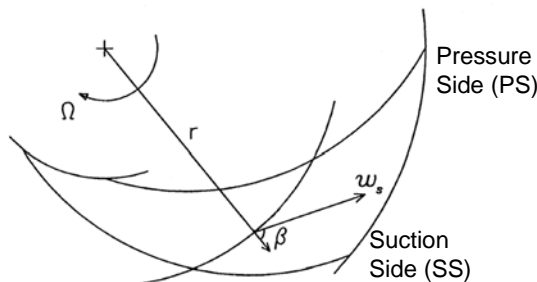


Fig. 22.3 Definition of the passage-wise flow velocity.

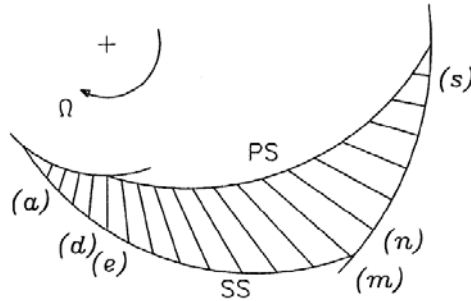


Fig. 22.4 Definition of the reference radial lines along which the passage-wise flow velocity was measured in Ref. 23 (from *a* to *s* in the alphabetical order).

The passage-wise flow velocities divided by Ωr_2 , where Ω is the impeller's angular velocity and $r_2 = 400$ mm is the impeller's outer radius, which were measured in Ref. 23 and obtained in the performed Flow Simulation calculations, are shown in Figs. 22.5-22.8. In these figures, the distance along the radial lines is divided by the line's length. The Flow Simulation results are presented in each of these figures by the curve obtained by averaging the corresponding nine curves in all the nine flow passages between the impeller blades. The calculated passage-wise flow velocity's cut plot covering the whole computational domain at the mid-height between the impeller's disks is shown in Fig. 22.9. Here, the *g*, *j*, *m*, *p* radial lines in each of the impeller's flow passages are shown. A good agreement of these calculation results with the experimental data is seen.

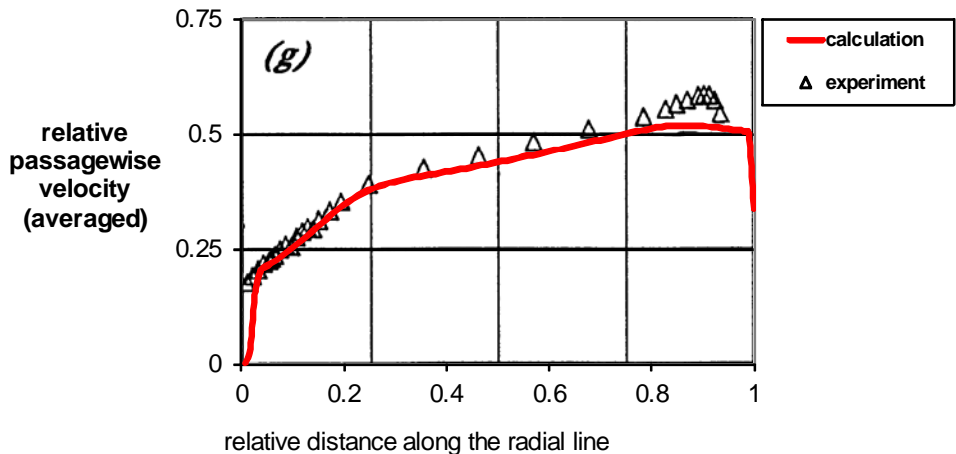


Fig. 22.5 The impeller's passage-wise flow velocity along the *g* (see Fig. 22.4) radial line, calculated by Flow Simulation and compared to the experimental data.

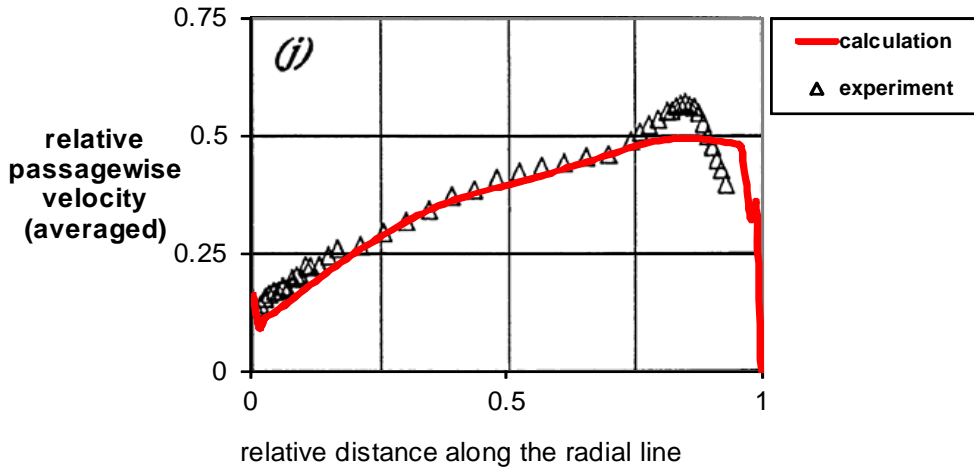


Fig. 22.6 The impeller's passage-wise flow velocity along the j (see Fig. 22.4) radial line, calculated by Flow Simulation and compared to the experimental data.

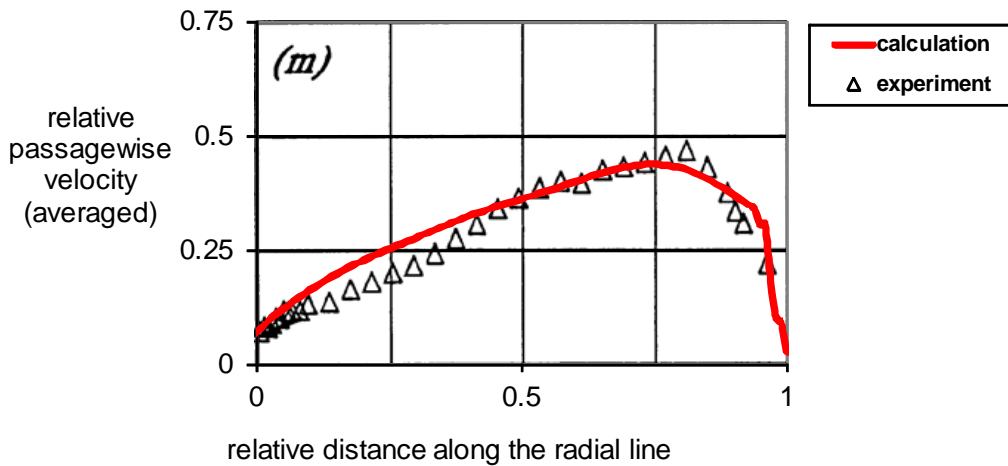


Fig. 22.7 The impeller's passage-wise flow velocity along the m (see Fig. 22.4) radial line, calculated by Flow Simulation and compared to the experimental data.

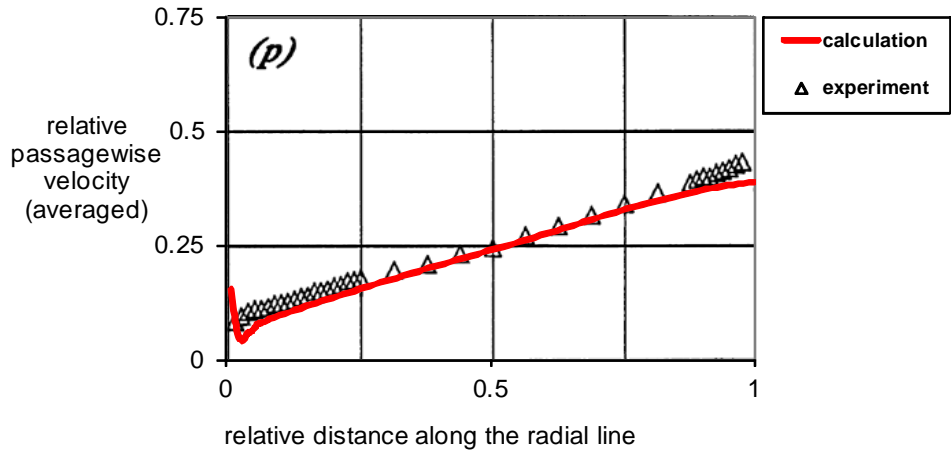


Fig. 22.8 The impeller's passage-wise flow velocity along the p (see Fig. 22.4) radial line, calculated by Flow Simulation and compared to the experimental data.

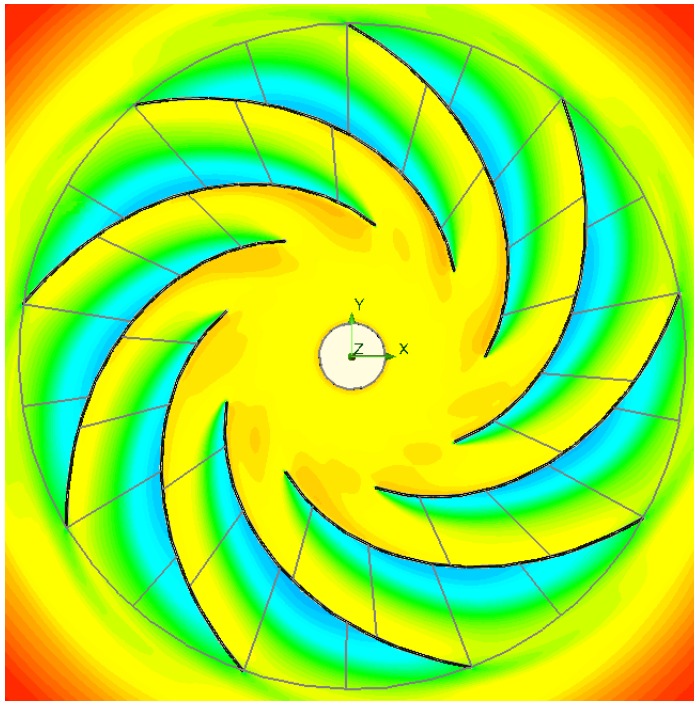


Fig. 22.9 A cut plot of the impeller's passage-wise flow velocity calculated by Flow Simulation.

Rotation of Greek Cross Cylinder

To validate the capability of Flow Simulation to simulate the rotation by using the **Local region(s) (Sliding)** option, let us consider a rotating cylinder of a Greek cross section with axes perpendicular to the direction of motion and determine the air force acting on the rotating cylinder. The model was tested at an airspeed of 10 m/s in infinite length-diameter ratio; cross-sectional dimensions are shown in Fig. 23.1. The results of its experimental study are given in Ref. 24.

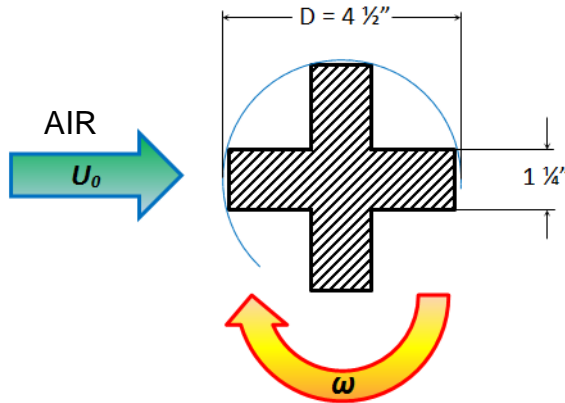


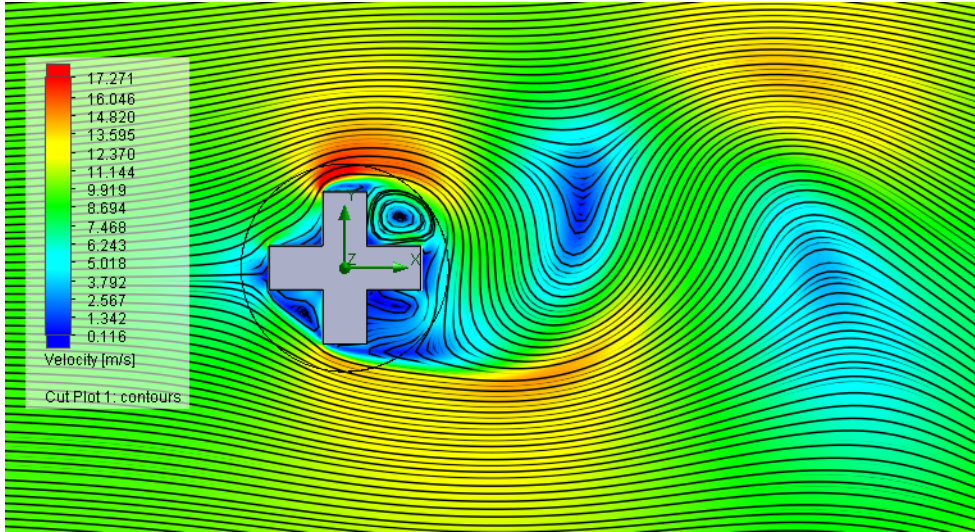
Fig. 23.1 Cylinder cross-section (according to Ref. 24).

The experimental data consist of drag and lift forces as functions of the ratio of peripheral to translation speed:

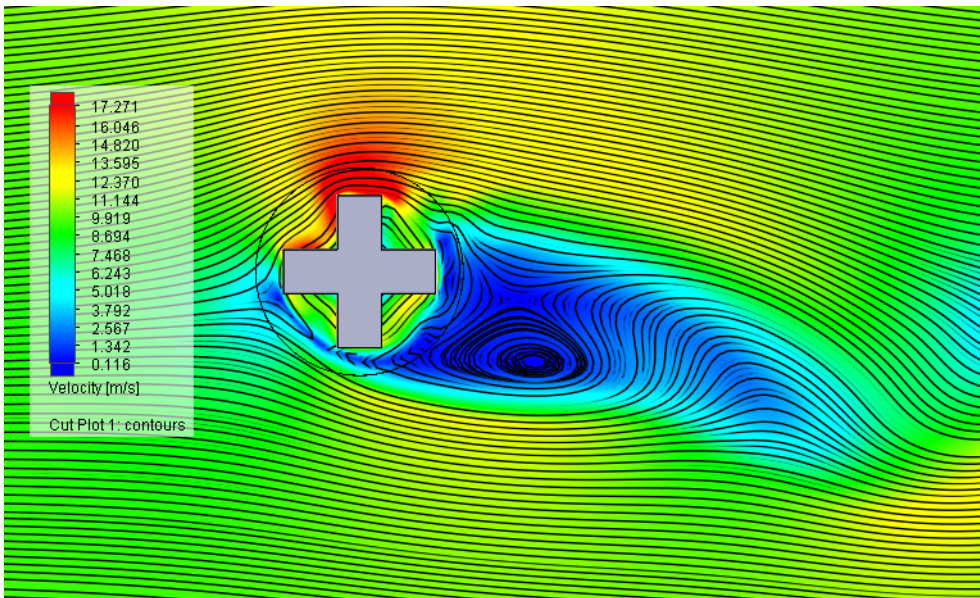
$$r = \frac{U'}{U_0} = \frac{D \cdot \pi \omega / 60}{U_0} \quad C_L = \frac{L}{qS} \quad C_D = \frac{D}{qS}$$

where U' is the peripheral speed, U_0 is the airspeed, ω is the rotation speed, L is the "lift" or the cross-wind force, D is the "drag" force, q is the dynamic pressure and S is the projected area of the cylinder.

For the calculation, a time-dependent analysis with the constant time step from 1/160 of the rotation period for $\omega \leq 1000$ rpm up to 1/80 of the rotation period for $\omega > 1000$ rpm has been performed on the 100x80x1 computational mesh. The flow fields at $\omega = 300$ rpm and $\omega = 2000$ rpm are shown in Fig. 23.2.



$\omega = 300$ rpm



$\omega = 2000$ rpm

Fig. 23.2 Flow fields at $\omega = 300$ rpm and $\omega = 2000$ rpm.

The aerodynamical coefficients, which were predicted by Flow Simulation and compared against the experimental data (see Ref. 24), are shown in Fig. 23.3.

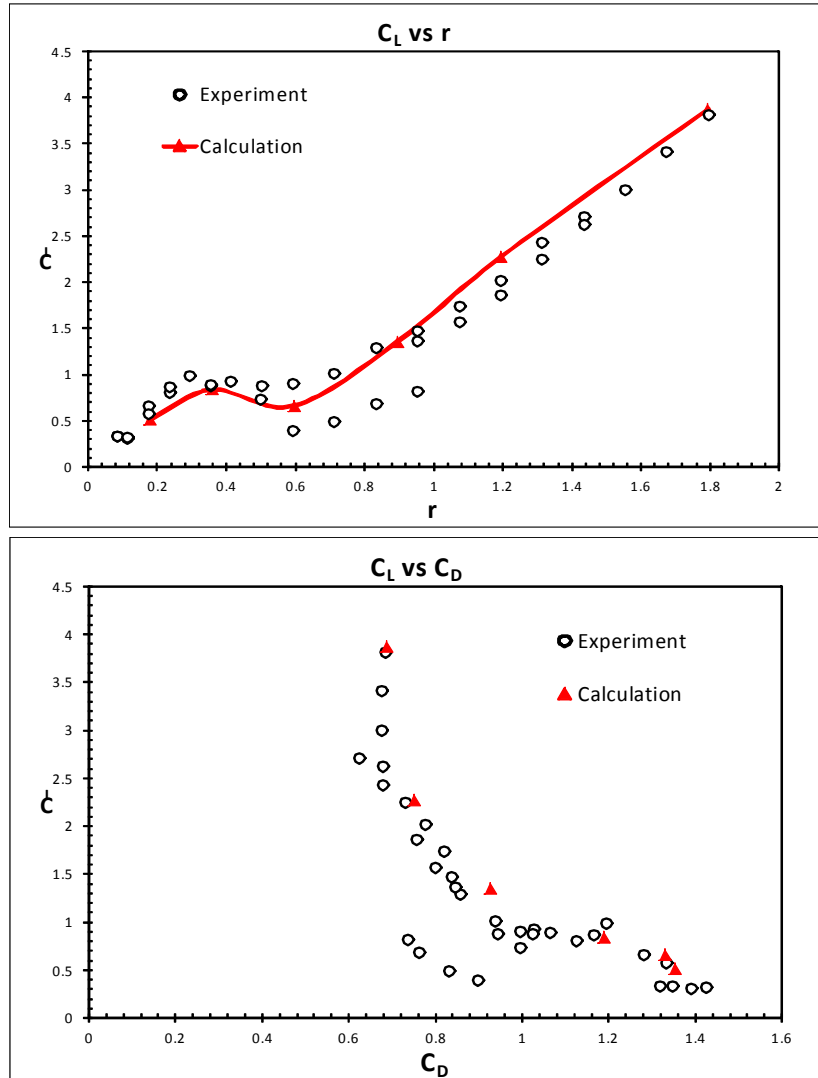


Fig. 23.3 The aerodynamical coefficients predicted by Flow Simulation and measured experiments

Comparison of the aerodynamical coefficients shows that Flow Simulation predicts the rotation effects with good accuracy.

Cavitation on a hydrofoil

When the local pressure at some point in the liquid drops below the liquid's vapour pressure at the local temperature, the liquid undergoes phase transition and form cavities filled with the liquid's vapor with an addition of gas that has been dissolved in the liquid. This phenomenon is called cavitation.

In this validation example we consider Flow Simulation abilities to model cavitation on the example of water flow around a symmetric hydrofoil in a water-filled tunnel. The calculated results were compared with the experimental data from Ref. 25.

The problem is solved in the 2D setting. A symmetric hydrofoil with the chord c of 0.305 m is placed in a water-filled tunnel with the angle of attack of 3.5° . The part of the tunnel being modelled has the following dimensions: length $l = 2$ m and height $h = 0.508$ m. The calculation is performed four times with different values of the cavitation number σ defined as follows:

$$\sigma = \frac{P_\infty - P_v}{\frac{1}{2} \rho U_\infty^2}$$

where P_∞ is the inlet pressure, P_v is the saturated water vapor pressure equal to 2340 Pa at given temperature (293.2 K), ρ is the water density at inlet, and U_∞ is the water velocity at inlet (see Fig. 24.1).

The inlet boundary condition is set up as Inlet Velocity of 8 m/s. On the tunnel outlet an Environment Pressure is specified so that by varying it one may tune the cavitation number to the needed value. The project fluid is water with the cavitation option switched on, and the mass fraction of non-condensable gas is set to $5 \cdot 10^{-5}$. A local initial mesh was created in order to resolve the cavitation area better. The resulting mesh contains about 30 000 cells.

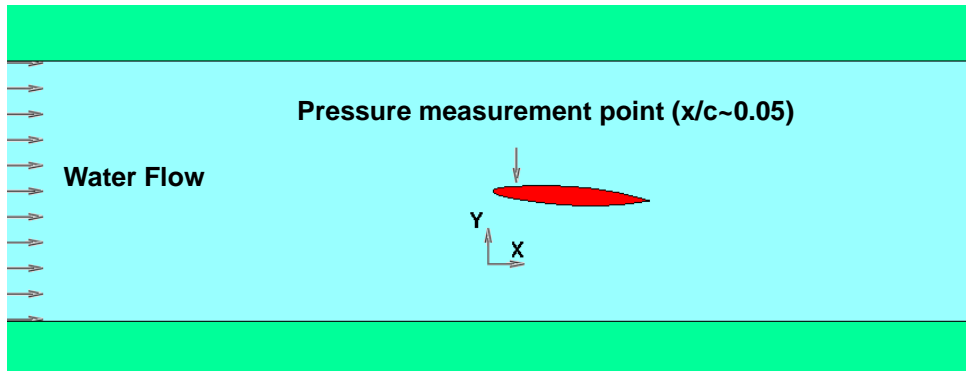


Fig. 24.1 The model geometry.

The qualitative comparison in a form of cut plots with Vapor Volume Fraction as the visualization parameter are shown on Fig. 24.2

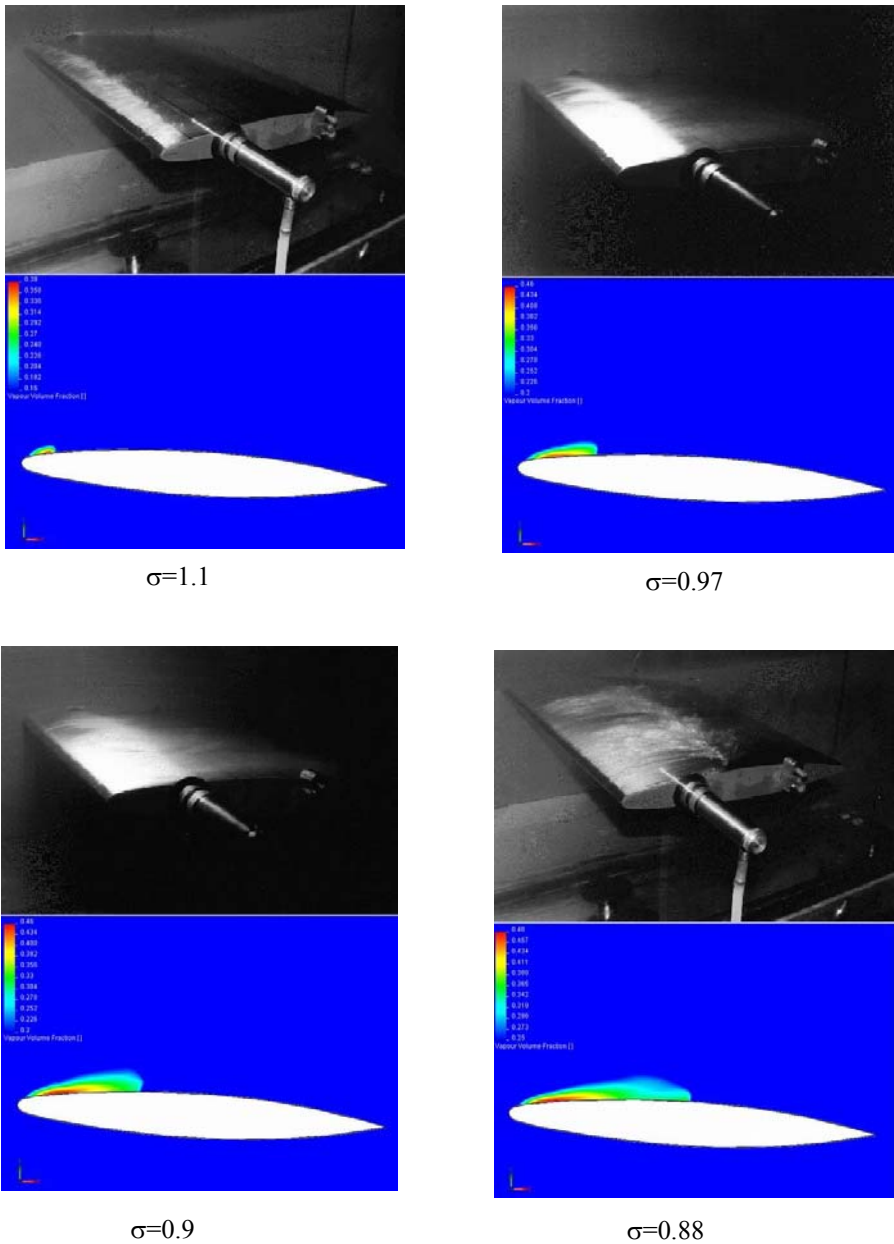


Fig. 24.2 A comparison of calculated and experimentally observed cavitation areas for different σ .

The calculated length of the cavitation area was derived from the distribution of the Vapor Volume Fraction parameter over the hydrofoil's surface as the distribution's width at half-height. The results are presented on Fig. 24.3

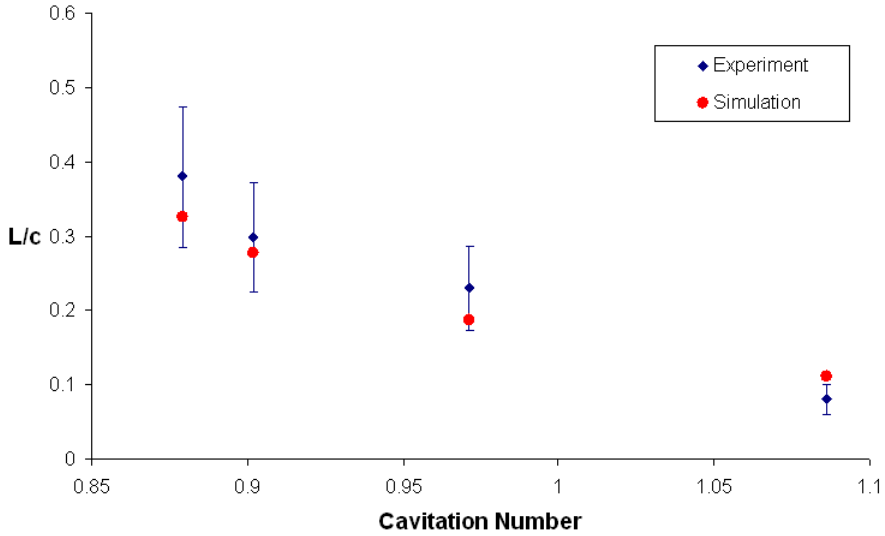


Fig. 24.3 A comparison of calculated and measured cavitation lengths.

According to Ref. 25, the "clear appearance" of the cavity becomes worse for larger cavity lengths. The experimental data also confirm that the amount of uncertainty increases with increasing cavity extent. Taking these factors into account together with the comparison performed above, we can see that the calculated length of the cavitation area agrees well with the experiment for a wide range of cavitation numbers.

Pressure measurements were performed on the hydrofoil surface at $x/c = 0.05$ in order to calculate the pressure coefficient defined as follows:

$$-C_p = \frac{P_\infty - P_{x/c=0.05}}{\frac{1}{2} \rho U_\infty^2}$$

A comparison of the calculated and experimental values of this parameter is presented on Fig. 24.4 and also shows a good agreement.

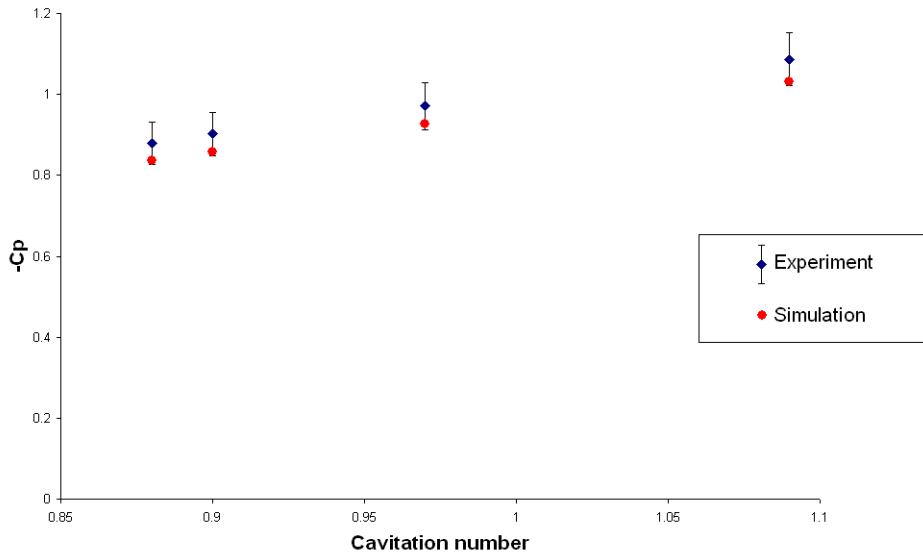


Fig. 24.4 A comparison of calculated and measured pressure coefficient

Isothermal Cavitation in a Throttle Nozzle

In this validation example we consider Flow Simulation capabilities to simulate cavitation in industrial liquid flows using the Isothermal cavitation model. The problem studied here validates this model by considering a 3D diesel fuel flow in a throttle channel that was studied experimentally in Ref. 26. According to this work, thermal effects in the considered flow are negligible. Therefore, it is reasonable to apply the Isothermal cavitation model.

Throttle channel geometry with its main dimensions is shown in Fig. 25.1

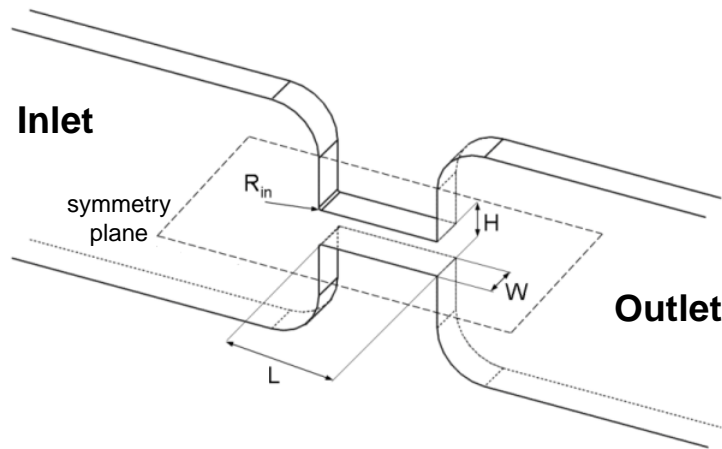


Fig. 25.1 The channel geometry: $L = 1$ mm, $H = 0.299$ mm, $W = 0.3$ mm, $R_{in} = 0.02$ mm.

Diesel fuel at 30°C is supplied to the inlet under the pressure (P_{in}) of 100 bar. The outlet pressure (P_{out}) varies from 10 to 70 bar. The properties of the analyzed fuel for the given temperature are presented in Table 25.1.

Table 25.1 Properties of the diesel fuel (2-D) at 30°C.

Density (kg/m^3)	836
Molar Mass (kg/mol)	0.198
Dynamic Viscosity ($\text{Pa}\cdot\text{s}$)	0.0025
Saturation Pressure (Pa)	2000

It is assumed that fuel contains dissolved air. The mass fraction of dissolved air is set to 0.001 to conform with the experimental data.

The objective of the calculations is to obtain channel characteristic under cavitation conditions and compare it with the experimental measurements. Because throttle channel has a symmetry plane, only a half of the model is used to generate the computational mesh. A finer local mesh is used to resolve the flow in the narrow channel and the adjacent regions providing about 15 mesh cells across the channel half-height. Additional refinement is performed in the region near the small fillet R_{in} . The resulting mesh are shown in Fig. 25.2.

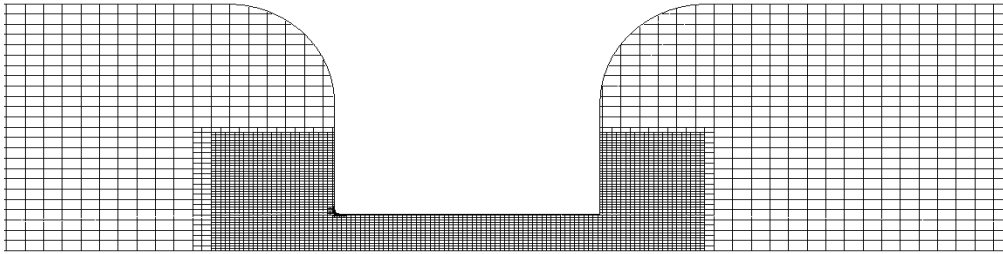


Fig. 25.2 The computational mesh (zoom-view).

Fig. 25.3 shows the distribution of the vapour volume fraction at different pressure drop. This figure provides a view of the initiation and development of the cavitation area.

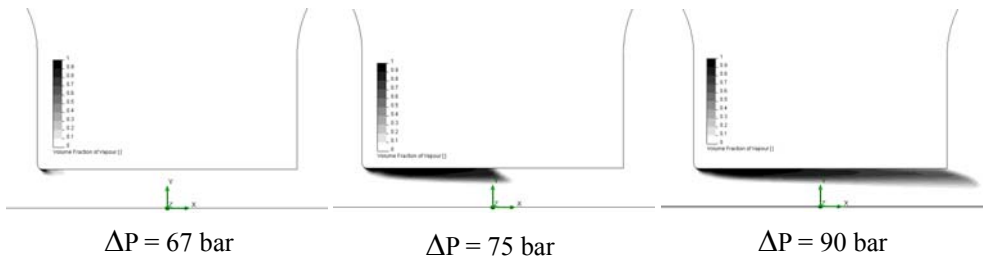


Fig. 25.3 Cavitation fields at symmetry plane.

The dependency of the pressure drop on the mass flow rate both predicted by Flow Simulation and determined experimentally are shown on Fig. 25.4. The difference between the calculations and the experimental measurements is less than 5%. Also, as it can be seen from the Fig. 25.3 and Fig. 25.4, the critical cavitation point corresponds to the pressure drop of about 70 bar. This point defines the transition from a pressure-dependent mass flow to choked mass flow that is induced by cavitation.

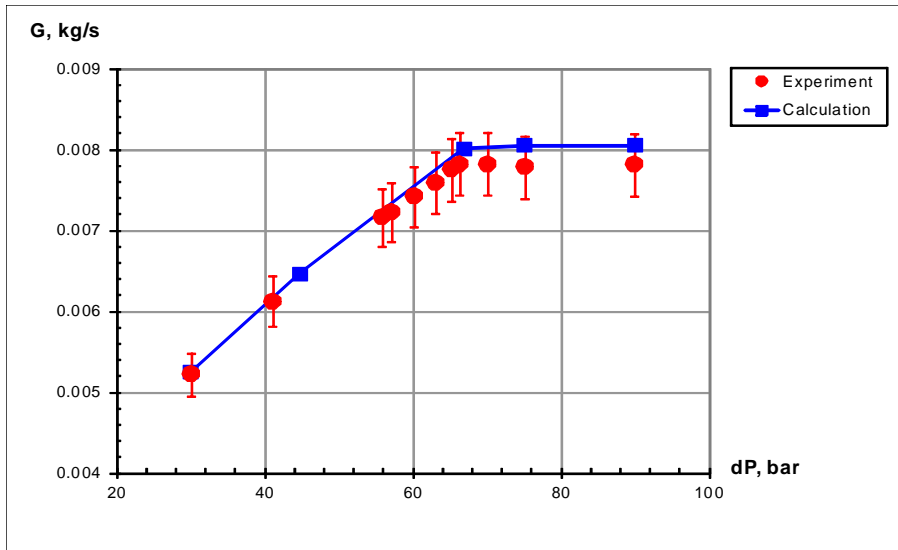


Fig. 25.4 Mass flow rate versus pressure drop at 100 bar inlet pressure in comparison with the experimental data (Ref. 26).

The comparison of the Flow Simulation calculations with the experimental data shows that the application of the Isothermal cavitation model that employs a limited set of fluid properties allows to predict cavitating flow characteristics with the sufficient accuracy.

Thermoelectric Cooling

Flow Simulation has the ability to model the work of a thermoelectric cooler (TEC), also known as Peltier element. The device used in this example has been developed for active cooling of an infrared focal plane array detector used during the Mars space mission (see Ref. 27).

According to the hardware requirements, the cooler (see Fig. 26.1) has the following dimensions: thickness of 4.8 mm, cold side of $8 \times 8 \text{ mm}^2$ and hot side of $12 \times 12 \text{ mm}^2$. It was built up of three layers of semiconductor pellets made of $(\text{Bi,Sb})_2(\text{Se,Te})_3$ -based material. The cooler was designed to work at temperatures of hot surface in the range of 120-180 K and to provide the temperature drop of more than 30 K between its surfaces.

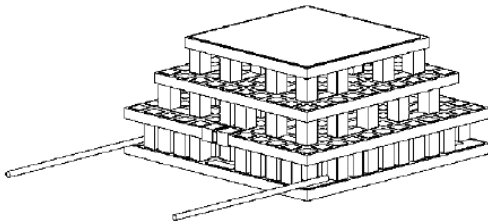


Fig. 26.1 Structure of the thermoelectric cooler.

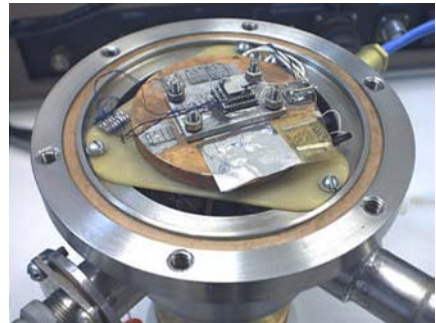


Fig. 26.2 The thermoelectric module test setup (image from Ref. 27).

To solve the engineering problem using Flow Simulation, the cooler has been modelled by a truncated pyramidal body with fixed temperature (Temperature boundary condition) on the hot surface and given heat flow (Heat flow boundary condition) on the cold surface (see Fig. 26.3).

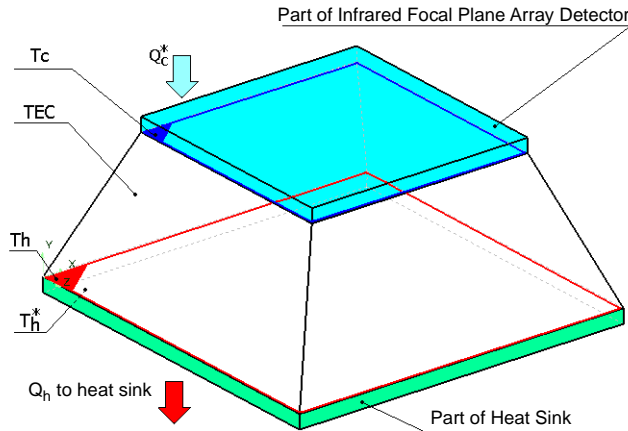


Fig. 26.3 The model geometry.

The TEC characteristics necessary for the modelling, i.e. temperature dependencies of the maximum pumped heat, maximum temperature drop, maximum current strength and maximum voltage, were represented in the Flow Simulation Engineering Database as a linear interpolation between the values taken from Ref. 27 (see Fig. 26.4).

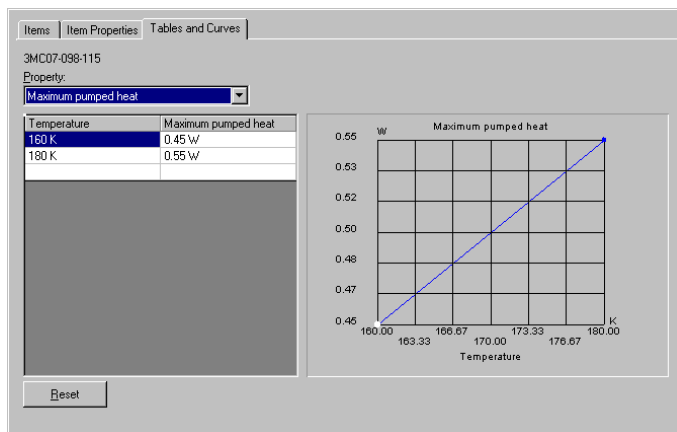


Fig. 26.4 The TEC's characteristics in the Engineering Database.

As it can be seen on Fig. 26.5, the temperature drop between the cooler's hot and cold surfaces in dependence of current agrees well with the experimental data.

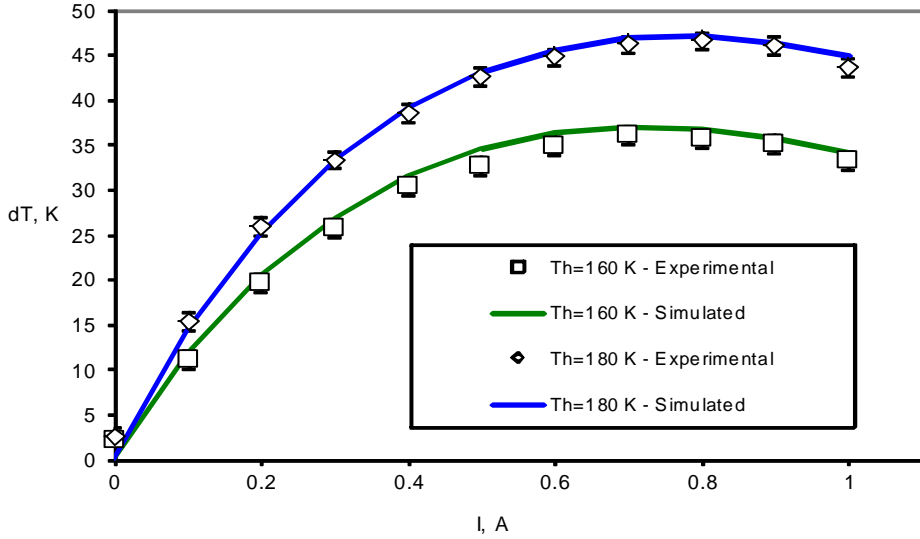


Fig. 26.5 ΔT as a function of current under various T_h .

The dependency of ΔT against heat flow under various T_h (see Fig. 26.6) is also in a good agreement with the performance data, as well as the coefficient of performance COP (see Fig. 26.7) defined as follows:

$$COP = \frac{Q_c}{P_{in}} = \frac{Q_c}{Q_h - Q_c}$$

where P_{in} is the cooler's power consumption, and Q_c and Q_h are the heat flows on the cold and hot faces, respectively.

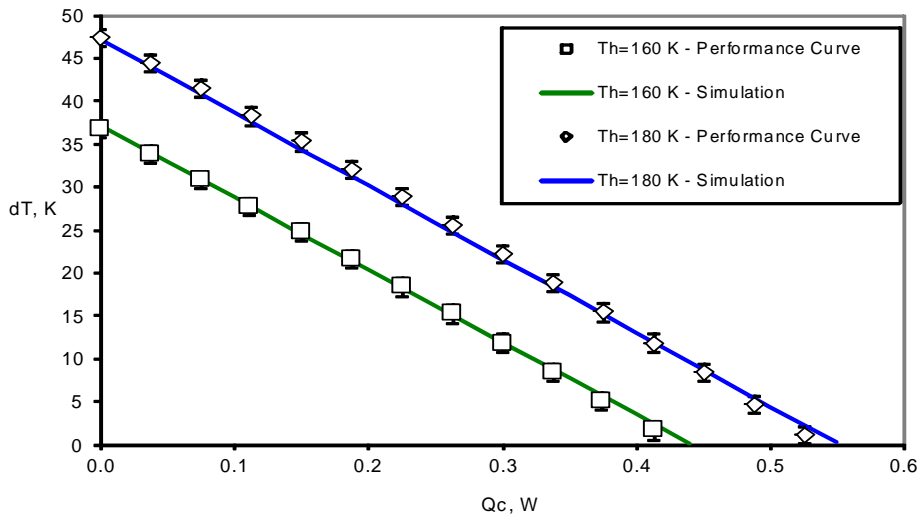


Fig. 26.6 ΔT as a function of heat flow under various T_h .

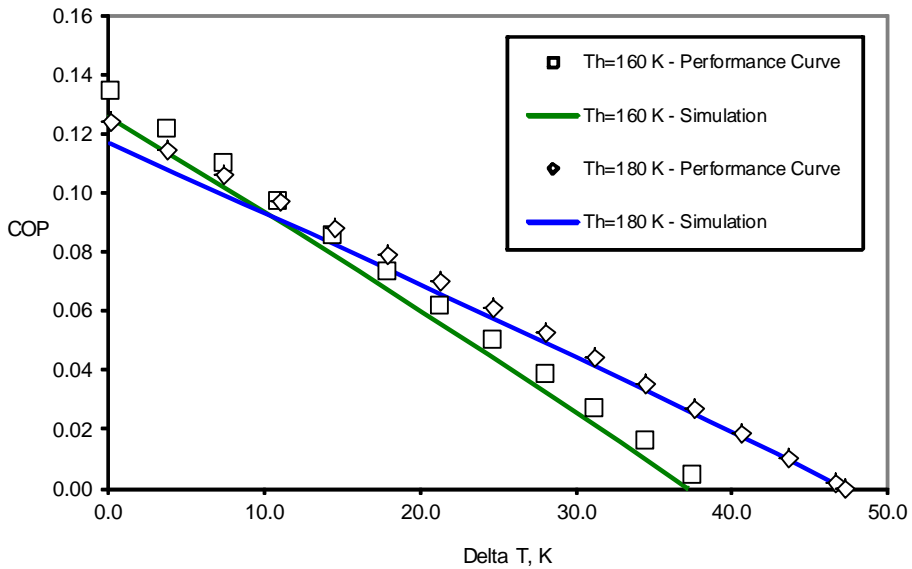


Fig. 26.7 COP as a function of ΔT under various T_h .

Finally, we may conclude that Flow Simulation reproduces thermal characteristics of the thermoelectric coolers at various currents and temperatures with good precision.

Buice-Eaton 2D Diffuser

To validate the performance of the Flow Simulation enhanced $k-\varepsilon$ turbulence model, let us consider a flow through the Buice-Eaton diffuser. This problem was a test-case for the 8th ERCOFTAC/IAHR/COST Workshop on Refined Turbulence modeling in Espoo, Finland, 17-18 June 1999. The flow includes a smooth-wall separation due to an adverse pressure gradient, reattachment and redevelopment of the downstream boundary layer. The results of its experimental study are given in Ref. 28. The data include mean and fluctuating velocities at various stations in the diffuser and skin friction data on both walls.

The Buice-Eaton diffuser, illustrated in Fig. 27.1, is an asymmetric 2D diffuser in which incompressible, fully developed turbulent flow undergoes smooth wall separation and reattachment. The lower wall of the diffuser slopes down at 10° and opens the diffuser up to 4.7 times the entrance height, $H = 0.59055$ in. The inlet channel flow is turbulent and fully-developed with a $Re = 20,000$ based on the centreline velocity and the channel height.

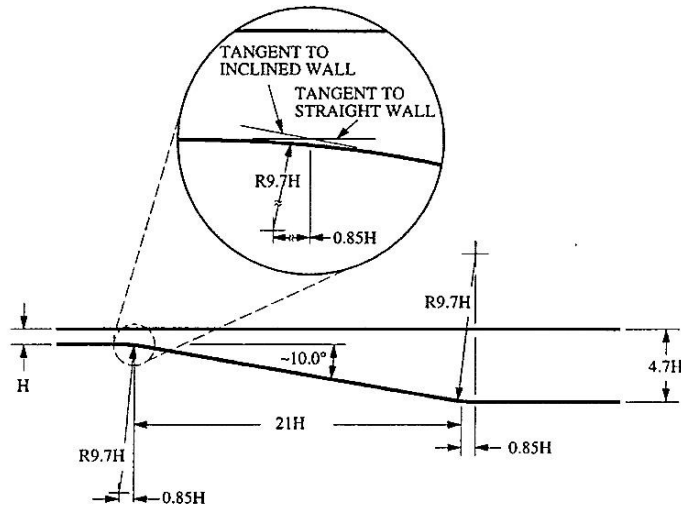


Fig. 27.1 Schematics of the diffuser (according to Ref. 28).

For the calculation, 2D computational domain was considered. As the **Fully developed flow** boundary condition was specified at the inlet, so a short entrance was used. A large outlet was used so that the flow had time to stabilise before reaching the outlet, to avoid causing any upstream effects. The basic initial mesh was 495x100x1 cells (in the X-Y plane).

The skin friction along lower and upper walls of Buice-Eaton diffuser is shown in Fig. 27.2.

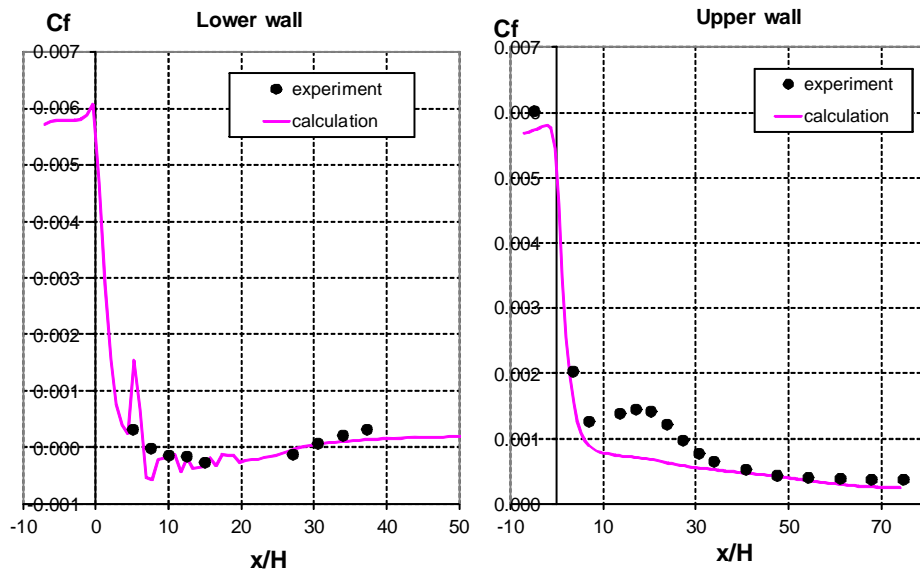


Fig. 27.2 Skin friction along lower and upper walls predicted by Flow Simulation and measured experimentally.

The mean velocity and turbulent kinetic energy profiles for the Flow Simulation simulation, along with experimental results can be seen in Fig. 27.3.

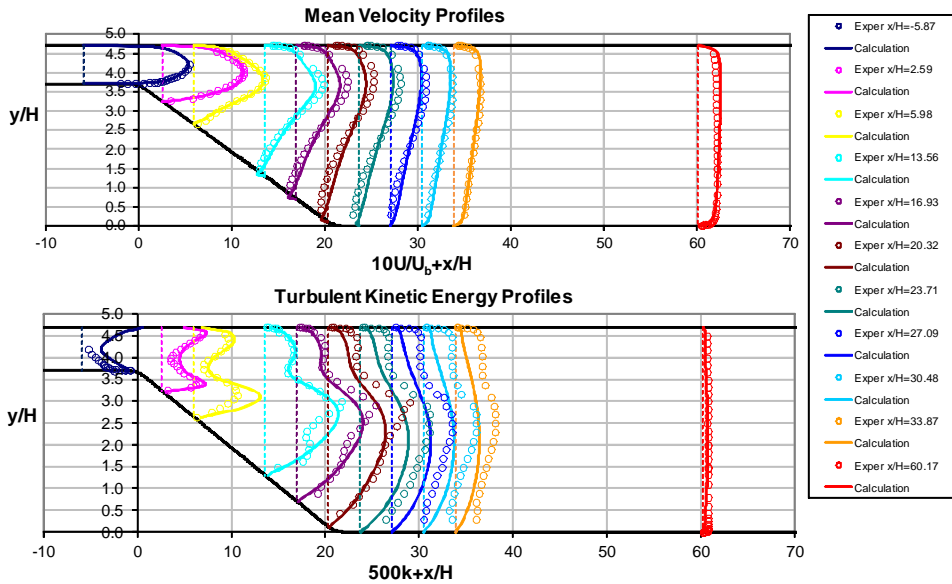


Fig. 27.3 Velocity and turbulent energy profiles predicted by Flow Simulation and measured experimentally.

Comparison of the experimental and calculated results shows that Flow Simulation predicts the separation point and the extent of the recirculation region with good accuracy.

Flow Over a Broad-crested Weir

In this validation example we consider Flow Simulation capabilities to simulate free-surface flows using the Volume of Fluid (VOF) technique. The problem studied here validates this model by considering a water flow over a broad-crested weir that was studied theoretically by using Bernoulli's theorem in Ref. 29.

The considered model of a broad-crested weir is shown in Fig. 28.1, where $H=0.06, 0.065, 0.07\text{ m}$ is the initial height of water, $a=0.05\text{ m}$ is the height of the weir at its highest point, d is the depth of the stream and h is the fall in water level below that some distance upstream where the water velocity V is negligibly small.

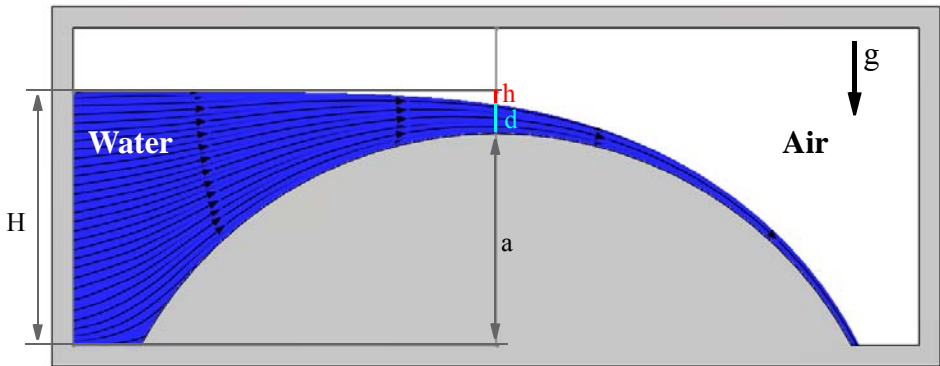


Fig. 28.1 Steady flow over a broad-crested weir.

The water density is $\rho=1000\text{ kg/m}^3$ and its viscosity is $\mu=0\text{ Pa}\cdot\text{s}$.

Lets observe the level of the surface of the dammed slowly-moving water upstream of the weir. At the place where $d+h$ is a minimum, i.e. above the highest point of the weir, the values of d and V are:

$$d_a = \frac{2}{3}(H - a) , \quad V_a = (gd_a)^{1/2}$$

For the calculation, 2D computational domain was considered and a time-dependent analysis was performed. To specify the initial water level and opening boundary conditions, the zero reference point for the pressure in hydrostatic equilibrium should be defined first. Let the zero reference point be at the height H . Thus the initial water distribution can be defined as **Initial Condition** by specifying the **Initial fluid** equals Water, the **Static Pressure** equals $P_{\text{atm}}=101325$ Pa and the **Pressure potential** is checked. The inlet boundary condition can be defined as the **Static Pressure** equals P_{atm} and the **Initial fluid** equals Water at the height below H and Air at the height above H , and the **Pressure potential** is checked. The outlet boundary condition can be defined as the **Static Pressure** specified as the dependency on height (y coordinate) $P_{\text{atm}}-\rho_{\text{air}}*g*(y-H)$, where $\rho_{\text{air}}=1.2 \text{ kg/m}^3$, $g=9.81 \text{ m/s}^2$, the **Initial fluid** equals Air, and the **Pressure potential** is unchecked.

Fig. 28.2 shows a comparison between the theoretical and calculated depth of the water stream d_a and the water velocity V_a at the weir highest point.

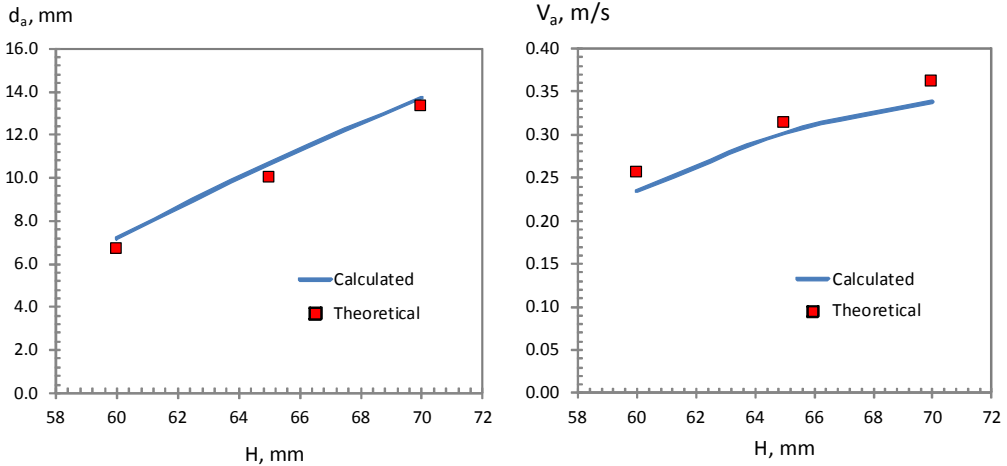


Fig. 28.2 The water stream depth and the velocity at the weir highest point predicted by theory and calculated by Flow Simulation.

Comparison of the water stream characteristics predicted by calculation and by theory shows that Flow Simulation simulates the free-surface flows with good accuracy.

References

- 1 Schlichting, H., *Boundary Layer Theory*. 7th ed., McGraw –Hill, New York, 1979.
- 2 Idelchik, I.E., *Handbook of Hydraulic Resistance*. 2nd ed., Hemisphere, New York, 1986. Version 6
- 3 Panton, R.L., *Incompressible Flow*. 2nd ed., John Wiley & Sons, Inc., 1996.
- 4 White, F.M., *Fluid Mechanics*. 3rd ed., McGraw-Hill, New York, 1994.
- 5 Artonkin, V.G., Petrov, K.P., *Investigations of aerodynamic characteristics of segmental conic bodies*. TsAGI Proceedings, No. 1361, Moscow, 1971 (in Russian).
- 6 Holman, J.P., *Heat Transfer*. 8th ed., McGraw-Hill, New York, 1997.
- 7 Humphrey, J.A.C., Taylor, A.M.K., and Whitelaw, J.H., *Laminar Flow in a Square Duct of Strong Curvature*. J. Fluid Mech., v.83, part 3, pp.509-527, 1977.
- 8 Van Dyke, Milton, *An Album of Fluid Motion*. The Parabolic press, Stanford, California, 1982.
- 9 Davis, G. De Vahl: *Natural Convection of Air in a Square Cavity: a Bench Mark Numerical Solution*. Int. J. for Num. Meth. in Fluids, v.3, pp. 249-264 (1983).
- 10 Davis, G. De Vahl, and Jones, I.P.: *Natural Convection in a Square Cavity: a Comparison Exercise*. Int. J. for Num. Meth. in Fluids, v.3, pp. 227-248 (1983).
- 11 Emery, A., and Chu, T.Y.: *Heat Transfer across Vertical Layers*. J. Heat Transfer, v. 87, p. 110 (1965).
- 12 Denham, M.K., and Patrick, M.A.: *Laminar Flow over a Downstream-Facing Step in a Two-Dimensional Flow Channel*. Trans. Instn. Chem. Engrs., v.52, pp. 361-367 (1974).
- 13 Yanshin, B.I.: *Hydrodynamic Characteristics of Pipeline Valves and Elements. Convergent Sections, Divergent Sections, and Valves*. “Mashinostroenie”, Moscow, 1965.

- 14 Enchao Yu, Yogendra Joshi: *Heat Transfer Enhancement from Enclosed Discrete Components Using Pin-Fin Heat Sinks*. Int. J. of Heat and Mass Transfer, v.45, p.p. 4957-4966 (2002).
- 15 Kuchling, H., *Physik*, VEB FachbuchVerlag, Leipzig, 1980.
- 16 Balakin, V., Churbanov, A., Gavrilouk, V., Makarov, M., and Pavlov, A.: *Verification and Validation of EFD.Lab Code for Predicting Heat and Fluid Flow*, In: CD-ROM Proc. Int. Symp. on Advances in Computational Heat Transfer "CHT-04", April 19-24, 2004, Norway, 21 p.
- 17 Jonsson, H., Palm B., *Thermal and Hydraulic Behavior of Plate Fin and Strip Fin Heat Sinks Under Varying Bypass Conditions*, Proc. 1998 Intersociety Conf. On Thermal and Thermomechanical Phenomena in Electronic Systems (ITherm '98), Seattle, May 1998, pp. 96-103.
- 18 Henderson, C.B. *Drag Coefficients of Spheres in Continuum and Rarefied Flows*. AIAA Journal, v.14, No.6, 1976.
- 19 Jyotsna, R., and Vanka, S.P.: *Multigrid Calculation of Steady, Viscous Flow in a Triangular Cavity*. J. Comput. Phys., v.122, No.1, pp. 107-117 (1995).
- 20 Darr, J.H., and Vanka, S.P.: *Separated Flow in a Driven Trapezoidal Cavity*. J. Phys. Fluids A, v.3, No.3, pp. 385-392 (1991).
- 21 Michelsen, J. A., *Modeling of Laminar Incompressible Rotating Fluid Flow*, AFM 86-05, Ph.D. Dissertation, Department of Fluid Mechanics, Technical University of Denmark, 1986.
- 22 Sorensen, J.N., and Ta Phuoc Loc: *Higher-Order Axisymmetric Navier-Stokes Code: Description and Evaluation of Boundary Conditions*. Int. J. Numerical Methods in Fluids, v.9, pp. 1517-1537 (1989).
- 23 Visser, F.C., Brouwers, J.J.H., Jonker, J.B.: *Fluid flow in a rotating low-specific-speed centrifugal impeller passage*. J. Fluid Dynamics Research, 24, pp. 275-292 (1999).
- 24 Elliott G. Reid *Tests of rotating cylinders*, NACA Technical Notes №209. December, 1924.
- 25 Wesley, H. B., and Spyros, A. K.: *Experimental and computational investigation of sheet cavitation on a hydrofoil*. Presented at the 2nd Joint ASME/JSME Fluid Engineering Conference & ASME/EALA 6th International Conference on Laser Anemometry. The Westin Resort, Hilton Head Island, SC, USA August 13 - 18, 1995.
- 26 Winklhofer, E., Kull, E., Kelz, E., Morozov, A. *Comprehensive Hydraulic and Flow Field Documentation in Model Throttle Experiments Under Cavitation Conditions*. Proceedings of the ILASS-Europe Conference, Zurich, pp. 574-579 (2001).
- 27 Yershova, L., Volodin, V., Gromov, T., Kondratiev, D., Gromov, G., Lamartinié, S., Bibring, J-P., and Soufflot, A.: *Thermoelectric Cooling for Low Temperature Space Environment*. Proceedings of 7th European Workshop on Thermoelectrics, Pamplona, Spain, 2002.
- 28 Buice, C. U. and Eaton, J. K., *Experimental Investigation of Flow Through an Asymmetric Plane Diffuser*, J. Fluids Engineering, Vol. 122, June 2000, pp. 433-435.

29 Batchelor, G.K. *An Introduction to Fluid Dynamics*. Cambridge University Press, 1967, 1973, 2000.

30

